ANALYSIS OF MICROTUBULE-PODOSOME CONTACTS AND THE IMPACT OF INF2, KANK1 AND DREBRIN

Dissertation zur Erlangung des Doktorgrades

an der Fakultät für Mathematik, Informatik und Naturwissenschaften

Fachbereich Biologie

der Universität Hamburg

vorgelegt von

Kathrin Weber

aus Itzehoe

Hamburg, 2022

Die vorliegende Arbeit wurde in der Zeit von Oktober 2017 bis Oktober 2022 unter der Leitung von Prof. Dr. Stefan Linder am Institut für Medizinische Mikrobiologie, Virologie und Hygiene des Universitätsklinikums Hamburg-Eppendorf angefertigt.

Dissertation zur Erlangung des Doktorgrades

an der Fakultät für Mathematik, Informatik und Naturwissenschaften

im Fachbereich Biologie der Universität Hamburg

vorgelegt von M. Sc. Kathrin Weber

aus Itzehoe

Erstgutachter:	Prof. Dr. Stefan Linder
Zweitgutachter:	PD Dr. Andreas Pommerening-Röser

Disputation: 17.01.2023

„Die Welt ist voller Sachen, und es ist wirklich nötig, dass sie jemand findet.“

– Astrid Lindgren

Table of contents

1 Zusammenfassung

Der Schwerpunkt dieser Arbeit lag in der schrittweisen Entwicklung des Software-basierten Programmes „ContactAnalyzer“ und dessen erfolgreicher Anwendung zur Untersuchung und Quantifizierung der intrazellulären Kontakte zwischen Podosomen und Mikrotubuli-Plus-Enden.

Podosomen sind Aktin-reiche, funktionell sehr vielfältige Adhäsionsstrukturen vieler Zellsysteme und werden in den hier untersuchten primären humanen Makrophagen spontan in großer Zahl gebildet. Sie haben eine dreigeteilte Struktur mit einem Aktinkern, einem adhäsiven Ring aus Plaque-Proteinen wie *Vinculin* und einer Kappe die sich z.B. durch Proteine wie α-*Actinin* auszeichnet. Um neben der Adhäsion auch ihre weiteren Funktionen, wie die Degradation von extrazellulärer Matrix durchführen zu können, benötigen Podosomen lytische Enzyme wie die membranständige Matrixmetalloprotease MT1-MMP. Der Transport dieser Enzyme in Vesikeln wird über Mikrotubuli, einer weiteren Zytoskelettkomponente, bewerkstelligt. Es konnte beobachtet werden, dass das Kontaktieren von Mikrotubuli-Plus-Enden an Podosomen Auswirkungen auf deren Dynamik hat. Bisher wurde jedoch keine genaue Analyse dieser Kontakte angefertigt, im Speziellen nicht der Einfluss verschiedener Podosomenkomponenten auf diese Interaktionen.

Zunächst wurden acht verschiedene Proteine als potentielle Kandidaten ausgewählt, die eine Rolle für die Kontakte oder deren Regulation spielen könnten. Hierzu zählen *inverted formin 2* (INF2), *lymphocyte-specific protein 1* (LSP1), *supervillin* (SV) als bekannte Kappenproteine sowie *drebrin* (DBN), welches im Rahmen dieser Arbeit als Kappenprotein identifiziert wurde. Die Podosomen-Kappe könnte durch ihre exponierte Position ein vielversprechendes Ziel für Mikrotubuli sein. Weiter wurde ein Protein des Ringes, *p21-activated kinase 4* (PAK4) sowie ein Podosomen-assoziertes Protein *IQ motif containing GTPase-activating protein 1* (IQGAP1) in die Analyse mit einbezogen. Für beide Proteine wurden Interaktionen mit Aktin bzw. Mikrotubuli gezeigt, daher sollte untersucht werden, ob sie auch einen Einfluss auf die Kontakte zwischen Podosomen und Mikrotubuli haben. Die zwei abschließenden Kandidaten *KN motif and ankyrin repeat domain-containing protein 1* (KANK1) und *protein rich in the amino acids E, L, K and S* (ELKS) sind Teil eines Komplexes, der Mikrotubuli Kortex-nah stabilisiert, dem sogenannten *cortical microtubule stabilization complex* (CMSC) und daher ebenfalls potentiell an der Regulation von Podosom-Mikrotubuli-Kontakten beteiligt.

Zunächst wurde ein Software-basiertes Auswertungsprogramm „ContactAnalyzer“ entwickelt und validiert, um Lebendzellaufnahmen zu analysieren. Dieses verwendet Koordinaten von Podosomen und Mikrotubuli, um festzustellen, ob ein Kontakt stattfindet und wie lange dieser

andauert. Außerdem können weitere Parameter wie Podosomen- und Mikrotubulianzahl und Podosomen-Lebenspanne ausgewertet werden.

In dieser Arbeit wurden vorbereitend 3 Mikrotubuli-Plus-Enden (+TIP)-Marker untersucht, wobei das EB3 (*end binding protein 3*) den geringsten Einfluss auf die Anzahl der Podosomen, Anzahl der Mikrotubuli-Plus-Enden sowie die Kontaktanzahl zwischen diesen beiden zeigte. Um den Einfluss der Podosomenkomponenten besser einschätzen zu können, wurde daher dieser Marker für alle folgenden Analysen gewählt. Nach der Auswahl der zu untersuchenden Podosomenkomponenten, wurde zunächst die Effizienz und der Einfluss ihrer siRNA basierten Depletion auf die allgemeine Zell- und Podosomencharakteristik untersucht. Es konnte gezeigt werden, dass für die meisten Depletionen der Kandidatenproteine keine signifikante Änderung in Zellgröße, Podosomenanzahl, -durchmesser oder -dichte zu beobachten sind. INF2-depletierte Zellen wiesen eine etwas geringere Größe und Anzahl von Podosomen auf, wodurch die Podosomendichte unverändert blieb. KANK1-depletierte Zellen zeigten eine verringerte Podosomendichte bei leicht erhöhtem Podosomendurchmesser.

Nach diesen vorbereitenden Analysen wurde die Auswirkung der Depletion einzelner Kandidatenproteine auf das Kontaktverhalten und Kontaktcharakteristika untersucht. Hier konnte im Vergleich zur Kontrolle gezeigt werden, dass trotz normaler Anzahl von Podosomen und detektierten Mikrotubuli-Plus-Enden die Anzahl der Kontakte bei einer *Drebrin*-Depletion massiv abnimmt, was nahelegte, dass *Drebrin* an der Initiierung der Kontakte beteiligt ist. Eine signifikante Zunahme der Kontaktanzahl konnte wiederum für INF2-depletierte Zellen gezeigt werden, was bedeutet, dass vorhandenes INF2 als negativer Regulator für Kontakte fungiert. Auch die Kontaktdauer zwischen Mikrotubuli-Plus-Enden und Podosomen wurde untersucht. Hier konnte für INF2-depletierte Zellen eine signifikante Verlängerung und für LSP1-depletierte Zellen eine Verringerung der Kontaktdauer festgestellt werden, was einen Hinweis darauf gibt, dass einerseits die Initiierung des Kontaktes und die Aufrechterhaltung der Podosomen-Mikrotubuli-Verbindung zwei verschiedene Prozesse sind. Anderseits zeigt es, dass Kappenproteine trotz ihrer gleichen Lokalisation im Podosom unterschiedliche Funktionen besitzen können.

Weiterhin wurde der Einfluss des Kontaktverhaltens und der Podosomenkomposition auf die Funktion des Podosomes untersucht. Sowohl für die INF2- als auch KANK1-Depletion konnte eine hoch signifikante Verringerung der Podosomen-Lebensspanne beobachtet werden. Dies zeigt, dass sowohl INF2 als auch KANK1 für die Stabilität von Podosomen von Bedeutung sind. Um mehr Informationen über die Struktur der Podosomen unter Depletion der Kandidaten zu erfahren, wurden mit einem bereits veröffentlichten Makro „Poji“ die Profile des typischen Ringproteins *Vinculin* sowie des Kappenproteins α-*Actinin* in Relation zu dem Aktinkern vermessen. Dabei wurde für INF2-depletierte Zellen eine Abnahme der Kappenintensität von

α–*Actinin* gemessen, für INF2- und KANK1-depletierte Zellen insbesondere eine Abnahme der Intensität des Ringproteins *Vinculin*. Möglicherweise liegt hierin auch eine Erklärung für die verminderte Lebenspanne der Podosomen, wenn bei INF2- bzw. KANK1-Depletion die Integrität des Podosomenrings nicht mehr vollständig gewahrt wird.

Da, wie bereits erwähnt, die Degradation von extrazellulärer Matrix eine wichtige Funktion der Podosomen darstellt, wurde diese mit Gelatine-Abbau-Versuchen getestet. Bei der Untersuchung der Degradationsfähigkeit konnte gezeigt werden, dass der Verlust von EB3 und/oder *Drebrin* zu einer Verstärkung des Matrixabbaus führt, der Verlust von INF2 oder KANK1 jedoch eine Unfähigkeit von Matrixabbau zur Folge hat. Da im letzteren Fall möglicherweise wiederum die Integrität des Ringes eine Rolle spielt, wurde insbesondere für den verstärkten Abbaueffekt bei EB3 und/oder *Drebrin*-Depletion eine Erklärung gesucht.

Da das lytische Enzym MT1-MMP für die Degradationsfähigkeit von Bedeutung ist, wurde die Menge an MT1-MMP auf der Zelloberfläche gemessen. Diese Analyse zeigte, dass Zellen mit einer EB3 und/oder *Drebrin*-Depletion signifikant mehr MT1-MMP an der Zelloberfläche aufweisen. Dieses Ergebnis steht im Einklang mit dem vermehrten Abbau, der in diesen Konditionen beobachtet wurde.

Zusammengenommen konnte innerhalb dieser Arbeit ein neues Werkzeug entwickelt werden, welches eine deutlich verbesserte und detailliertere Analyse von Mikrotubuli-Podosomen-Kontakten ermöglicht. Neben der Charakterisierung von *Drebrin* als neuem Kappenprotein, konnte so insbesondere der Einfluss von den Kappenproteinen *Drebrin*, LSP1 und INF2 für diese Kontakte identifiziert werden. Außerdem wurde eine verkürzte Podosomen-Lebensspanne für INF2- und KANK1-Depletionen verzeichnet, welche mit verringerter Degradation von extrazellulärer Matrix einherging. Eine Steigerung dieser wurde wiederum für Zellen mit *Drebrin* und/oder EB3 Depletion beobachtet, welche mit erhöhter MT1-MMP Konzentration auf der Zelloberfläche korrelierte.

2 Abstract

The focus of this work was the stepwise development of the software-based program "ContactAnalyzer" and its successful application to study and quantify intracellular contacts between podosomes and microtubule plus ends.

Podosomes are actin-rich, functionally diverse adhesion structures of many cell systems, and they are formed spontaneously in large numbers in the primary human macrophages studied here. They have a tripartite structure with an actin core, an adhesive ring of plaque proteins such as vinculin, and a cap characterized by proteins such as α-actinin. In addition to adhesion to carry out their other functions, for example, degradation of extracellular matrix, podosomes require lytic enzymes such as the membrane-bound matrix metalloprotease MT1-MMP. The transport of these enzymes in vesicles is accomplished via microtubules, another cytoskeletal component. It has been observed that the contact between microtubule plus ends and podosomes affects the dynamics of podosomes. However, no detailed analysis of these contacts has been made to date; specifically, the influence of different podosome components on these interactions has not been analyzed yet.

Initially, eight different proteins were selected as potential candidates that might play a role in the contacts or their regulation. These include *inverted formin 2* (INF2), *lymphocyte-specific protein 1* (LSP1), *supervillin* (SV) as known cap proteins, and *drebrin* (DBN), which was identified as a cap protein in this work. The podosome cap could be a promising microtubule target due to its exposed position. Additionally, a protein of the ring, *p21-activated kinase 4* (PAK4), as well as a podosome-associated protein *IQ motif containing GTPase-activating protein 1* (IQGAP1), were included in the analysis. Both proteins have been shown to interact with actin and microtubules, respectively, so it should be investigated whether they also affect podosome-microtubule contacts. The two final candidates, *KN motif and ankyrin repeat domain-containing protein 1* (KANK1) and *protein rich in the amino acids E, L, K and S* (ELKS), are part of a complex that stabilizes microtubules close to the cortex, the so-called *cortical microtubule stabilization complex* (CMSC), and are therefore also potentially involved in the regulation of podosome-microtubule contacts.

First, a software-based analysis program named "ContactAnalyzer" was developed and validated to analyze live cell recordings. It uses the coordinates of podosomes and microtubules to determine whether contact occurs and how long it lasts. In addition, other parameters, such as podosome and microtubule number, as well as podosome lifespan, can be evaluated.

In preparation of this work, three microtubule plus end (+TIP) markers were investigated, of which EB3 (*end binding protein 3*) showed the slightest influence on the number of podosomes

and microtubule plus ends and the number of contacts between them. Therefore, this marker was chosen for all subsequent analyses to better assess the influence of podosome components. After having selected the podosome components to be studied, the efficiency and influence of their siRNA-based depletion on the general cell and podosome characteristics were investigated. For most depletions of the candidate proteins, no significant change in cell size, podosome number, diameter, or density was observed. INF2-depleted cells exhibited a slightly smaller podosome size and number, leaving podosome density unchanged. KANK1-depleted cells showed a decreased podosome density with a slightly increased podosome diameter.

Following these preliminary analyses, the effect of the depletion of individual candidate proteins on contact behavior and contact characteristics was examined. Compared to the control condition, it was shown that despite regular numbers of podosomes and detected microtubule plus ends, the number of contacts massively decreases upon *drebrin* depletion; this suggests that *drebrin* is involved in the initiation of contacts. However, a significant increase in contact number was shown for INF2-depleted cells, implying that expressed INF2 acts as a negative regulator of contacts. The contact duration between microtubule plus ends and podosomes was investigated as well: Here, a significant increase in contact duration was found for INF2-depleted cells and a decrease for LSP1-depleted cells, indicating that, on the one hand, initiation of contact and maintenance of the podosome-microtubule junction are two different processes. And on the other hand, cap proteins can have different functions despite their same localization in the podosome structure.

Further, this work aimed to determine whether the altered contact behavior and podosome composition impact the podosome function. A massive reduction in podosome lifespan was observed for both INF2 and KANK1 depletion. This indicates that both INF2 and KANK1 are important for podosome stability. To learn more about the structure of podosomes under depletion of the candidates, a previously published macro, "Poji", was used to measure the profiles of the typical ring protein vinculin and the cap protein α-actinin in relation to the actin core. A decrease in the cap intensity of α-actinin was measured for INF2-depleted cells, and a decrease in the intensity of the ring protein vinculin was measured for INF2- and KANK1-depleted cells in particular. This may also explain the podosome's decreased lifespan when the integrity of the podosome ring is no longer fully maintained upon INF2 or KANK1 depletion.

Since, as mentioned above, degradation of the extracellular matrix is an essential function of podosomes, it was tested with gelatin degradation experiments. When the degradation capacity was examined, it was shown that the loss of EB3 and/or *drebrin* leads to an enhancement of matrix degradation, but the loss of INF2 or KANK1 results in an inability of matrix degradation. Whereas in the latter case, the ring's integrity may again play a role, an

explanation was sought for the enhanced degradation effect upon EB3 and/or drebrin depletion.

Since the lytic enzyme MT1MMP is essential for the degradation capacity, the amount of MT1-MMP on the cell surface was measured. This analysis showed that cells with EB3 and/or drebrin depletion had significantly more MT1-MMP on the cell surface. This result is consistent with the increased degradation observed in these conditions.

Collectively, a new tool was developed within this work that allows a significantly improved and more detailed analysis of microtubule-podosome contacts. Besides the characterization of *drebrin* as a new cap protein, the influence of the cap proteins *drebrin*, LSP1, and INF2 for these contacts could be identified. In addition, a shortened podosome lifespan was recorded for INF2 and KANK1 deletions, which was associated with reduced extracellular matrix degradation. On the other hand, an increase in this was observed for cells with *drebrin* and/or EB3 depletion, correlating with an increase in cell surface located MT1-MMP, suggesting a role of these proteins in endocytosis.

3 Introduction

3.1 Macrophages

3.1.1 Origin

Macrophages were first described in the 19th century as phagocytic cells of the immune system and belong to the group of leucocytes, also known as white blood cells[1-4]. Macrophages differentiate from bone marrow-derived monocytes. Those precursors are recruited from the blood circulation to sites of inflammation, infection, or damage and differentiate in the tissue[2], among others, upon cytokine stimulation to macrophages. However, whereas monocytes are still dividing, differentiated macrophages no longer proliferate to any meaningful extent.

Further, specialized tissue-resident macrophages that are not recruited via the bloodstream but migrate into the particular tissue at embryonic stages of development differentiate locally and show self-replenishing behavior[5]. The most prominent examples of these cell types are microglia in the brain[6], Kupffer cells in the liver[7], Langerhans cells in the skin[8], osteoclasts in the bone[9], and alveolar[10] macrophages in the lung, among others.

Macrophages are widely distributed throughout the tissues and display a wide functional heterogeneity. Contingent on the given surrounding, cytokines, and microenvironment, macrophages may assume pro-inflammatory as well as anti-inflammatory functions. As such, macrophages are subcategorized into M1 and M2 phenotypes according to their position in the inflammatory process. M1 macrophages seem to play a crucial role in the initial stages of inflammation; M2, on the other hand, is associated with the resolution of inflammation. The M1 and M2 activation states constitute the furthest points of the inflammatory spectrum, with research suggesting there may well be a seamless transition between these pronounced phenotypes. This polarization of macrophages into M1 or M2 was shown to be very plastic and reversible[11-13].

3.1.2 Function

The primary function of macrophages is to distinguish between benign and harmful microorganisms through pathogen-associated molecular patterns[14], making them critical players in the maintenance of homeostatic and healthy tissue as well as the regulation and mitigation of inflammatory processes[15]. Macrophages constitute a part of the innate immune system and are the first cellular defense against pathogens through phagocytosis[16]. Further, they are involved in tissue clearance by phagocytosing apoptotic cells, cell debris, and parts

of the extracellular matrix (ECM)[10]. Particularly M1-macrophages are characterized by strong microbicidal and tumoricidal activity, among others, mediated by the secretion of specific cytokines or reactive oxygen species (ROS)[17]. M2 macrophages, on the other hand, show an anti-inflammatory response characterized by high phagocytic activity, containment of parasites, wound healing, and tissue repair alongside angiogenesis. The latter function has also been described in pathological conditions, as it positively influences tumor progression[13, 18]. Therefore, the regulation of the M1 and M2 polarization and the successive occurrence of both states is required for the appropriate termination of inflammatory responses and adequate tissue repair after injury. Defects in the ability to shift between macrophage polarization states result in chronic inflammatory pathologies, autoimmune diseases, and even metabolic disorders[11, 12, 19].

An area of considerable interest is the association of highly heterogenic macrophages infiltrating tumorous tissue, i.e., tumor-associated macrophages (TAMs). Tumors are frequently characterized by their dense tissue, as well as by inflammation of the affected tissue, leading to the recruitment of monocyte-derived macrophages, generally an M1 phenotype, in the early stages of cancer development[20, 21]. The potentially 'aggressive' pro-inflammatory and tumoricidal activity of M1 macrophages may enable or even promote metastasis of specific tumor types. The interplay of all present cells adds up to complicated interactions and cross-talk, contributing to a unique environment, and was correlated with a poor prognosis in, for example, Hodgkin's disease, glioma, ovarian, and breast carcinoma[13]. However, not only is the regulation and crosstalk intercellularly highly interesting, but the regulation processes within macrophages contributing to this interplay are not fully understood.

To fulfill all these functions, macrophages need to migrate through the tissue. To date, two migration modes are known, the amoeboid and the mesenchymal process[22-24]. With its relatively high velocity of around 0.7 µm/min, only a few adhesion structures and low ECM remodeling[22] characterize the former migration mode. In the latter migration mode, cells appear less spherical, migrate significantly slower (0.2 µm/min), and display more adhesive structures as well as ECM degradation and remodelling[22]. Macrophages can switch between these two migration types depending on the density of the extracellular matrix and tissue stiffness[23]. Since tumors are often characterized by dense tissue, this leads to an elevated research interest in macrophages and their interaction with tumors. The adhesive and degrading properties of macrophages are mainly, but not exclusively, mediated by a structure named podosome[25].

3.2 Podosomes

First described in 1980, actin-rich structures with an altered vinculin localization were found in fibroblasts that were transformed with the Rous sarcoma virus[26]. Later they were named podosomes[27] since they were located at the ventral sites of the cells and found to mediate adhesion to the extracellular matrix reminding the researchers of cellular feet (from *podos*: feet and *soma*: body). When stimulated by cytokines[28] (e.g., TGF-β[29]), these actin-rich structures were found in several cell types such as smooth muscle cells[30, 31], endothelial cells[28, 32], megakaryocytes[33], and eosinophils[34]. Physiologically and in a constitutively vast amount, podosomes are displayed by cells of the monocytic lineage like macrophages[27, 35], dendritic cells[36], and osteoclasts[37, 38]. On the other hand, cancer cells form similar structures termed invadopodia[39, 40]. These are summarized with podosomes under the umbrella term invadosomes[36, 41]. In contrast to invadopodia, podosomes occur in greater numbers, are more dynamic, and smaller in size[41, 42].

3.2.1 Structure

Podosomes are characterized by a tri-partite structure with an actin-rich core, a ring of plaque proteins, and a cap. The core is roughly 0.5-1 µm in diameter with a height of 0.6 µm, comprised of mainly branched F-actin[35]. In addition, proteins involved in (de-)polymerization, regulation, or crosslinking/bundling of actin are frequently found to be core components. This includes, for instance, Arp2/3[36, 43] complex and formins (actin assembly), WASP[35 31, 38], CDC42[35] and cortactin[44, 45] (regulation), gelsolin and cofilin (disassembly) or α-actinin, caldesmon, fimbrin, and fascin (interconnection of actin filaments)[27, 37, 46, 47].

The ring consists of different plaque proteins that bind to integrins, mediating a firm adhesion of the whole structure to the substrate. Super-resolution microscopy revealed that typical ring proteins like vinculin, talin, zyxin, or paxillin are organized in clusters or polygonal configurations rather than continuous rings[48, 49]. Podosomes show two sets of myosin IIA containing cables, where F-actin is organized into tightly packed bundles. While the lateral cables connect the ring and core of one podosome, the dorsally located cables connect single podosomes into super-structures like clusters, rosettes, rings, and belts[38, 50-55].

The most recently found substructure of the podosome is the cap that contains proteins like INF2, supervillin, and LSP1[56-59]. While neither all cap proteins nor their functions have been fully characterized, regulatory effects on actin dynamics and myosin contractility have been reported for most of them[57-59].

Typically around ~300 evenly spaced podosomes can be found in a resting macrophage[60]. However, podosomes are located primarily at the leading edge of migrating macrophages[61, 62].

Further, in macrophages are at least two podosome subpopulations described based on their size, dynamics, and localization: precursors (located at the cell periphery, larger, less static, show fission and fusion) and successors (located in the central cell part, smaller and more static)[42, 47].

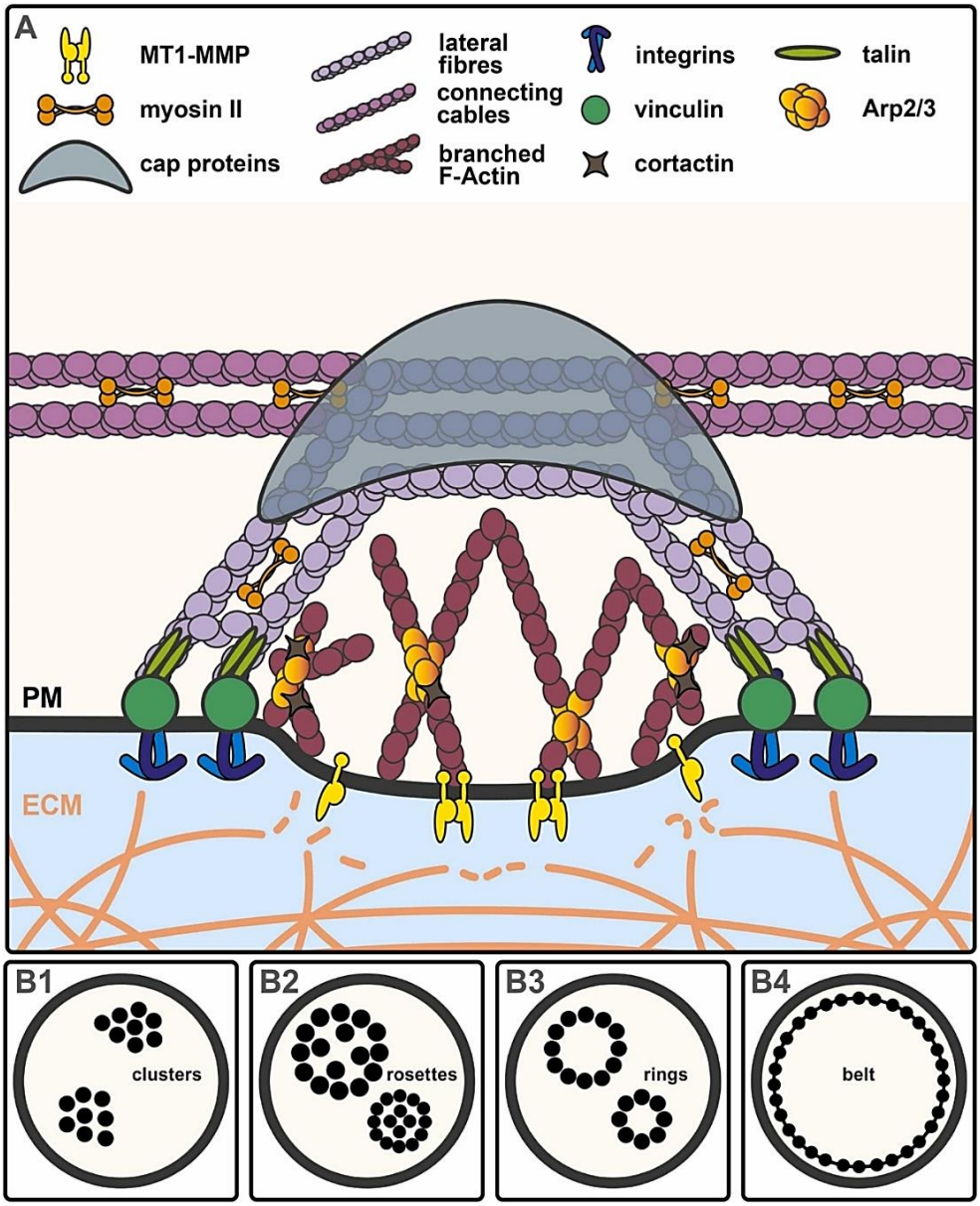

Figure 1: Podosome architecture.

A) Podosomes display a tripartite structure with i) an F-actin rich core based on Arp2/3 complex dependent nucleation, containing different regulatory proteins, e.g. cortactin. At its ventral side the matrix metalloprotease MT1-MMP is located. ii) a ring structure that is formed of patches with plaque proteins like vinculin and talin, mediating via integrins a firm adhesion to the substrate. iii) a cap structure consisting of, for example, actomyosin regulating proteins like LSP1 and supervillin. Further, there are two sets of unbranched actin cables containing myosin IIA: the lateral cables, linking the core with the ring and contractile connecting cables that interconnect podosomes to superstructures. B1-B4) Different observed superstructures of podosomes. PM: plasma membrane, ECM: extracellular matrix (light blue), ECM filaments in orange. From Weber et al., 2022.

3.2.2 Function

Podosomes are multipurpose structures that display a variety of functions and abilities. Among the earliest recorded functions of podosomes was their relevance in cell adhesion. In human macrophages, podosomes were shown to mediate the adhesion and migration of the cell. To regulate migration modes, podosomes have to integrate information about the extracellular matrix's rigidity[51] and sense the topography of their environment. Furthermore, podosomes translate ECM properties like substrate stiffness into traction forces, using actin polymerization and myosin contractility[51, 53, 63, 64]. These forces can induce conformational changes in mechanosensitive ring proteins[63, 65, 66], which initiates signaling cascades leading to matrix degradation[67]. Matrix degradation at podosomes depends partially on microtubule-based vesicle transport of different metalloproteases like soluble MMPs or membrane-bound MT1-MMP[68, 69].

3.2.3 Regulation

Some cells require stimulation with growth factors or transformation to form podosomes, whereas macrophages display podosomes constitutively. Therefore, the regulation of formation, dynamics like fusion and fission, as well as the arrangement of super-structures, is likely to be very cell-type specific. If not stated otherwise, the following findings are for cells of the monocytic lineage, i.e., cells that form podosomes constitutively, with a focus on primary human macrophages.

The essential requirement for podosome formation is the adhesion of the cell to a substrate via integrins and CD44 at sites of low contractility[60, 70-73]. This induces major reorganization of the actin cytoskeleton[46], including the activation of Src-kinases and RhoGTPases[74]. CDC42 supports the podosome core's formation by activating the WASP-Arp2/3 cascade, which in turn promotes the formation of branched F-actin[35, 43]. With the further assembly of the cap and actomyosin cables, the podosome gains its protrusive function[75, 76]. Proteins of the cap like caldesmon[77], fascin[78], or INF2[57] have been reported to regulate the podosome size, as well as proteins located in the ring like PAK4[79], possibly forming a “restricting corsage” around the core. Fully assembled podosomes can be targeted for the microtubule-dependent transport of proteins that enable the degradative function of podosomes, like MMPs[80] or DNaseX[81]. For human macrophages, it was shown that MT1-MMP is transported in vesicles moved by kinesin-1 and -2 motor proteins[82] toward podosomes. MT1-MMP is subsequently embedded underneath the F-actin core[83].

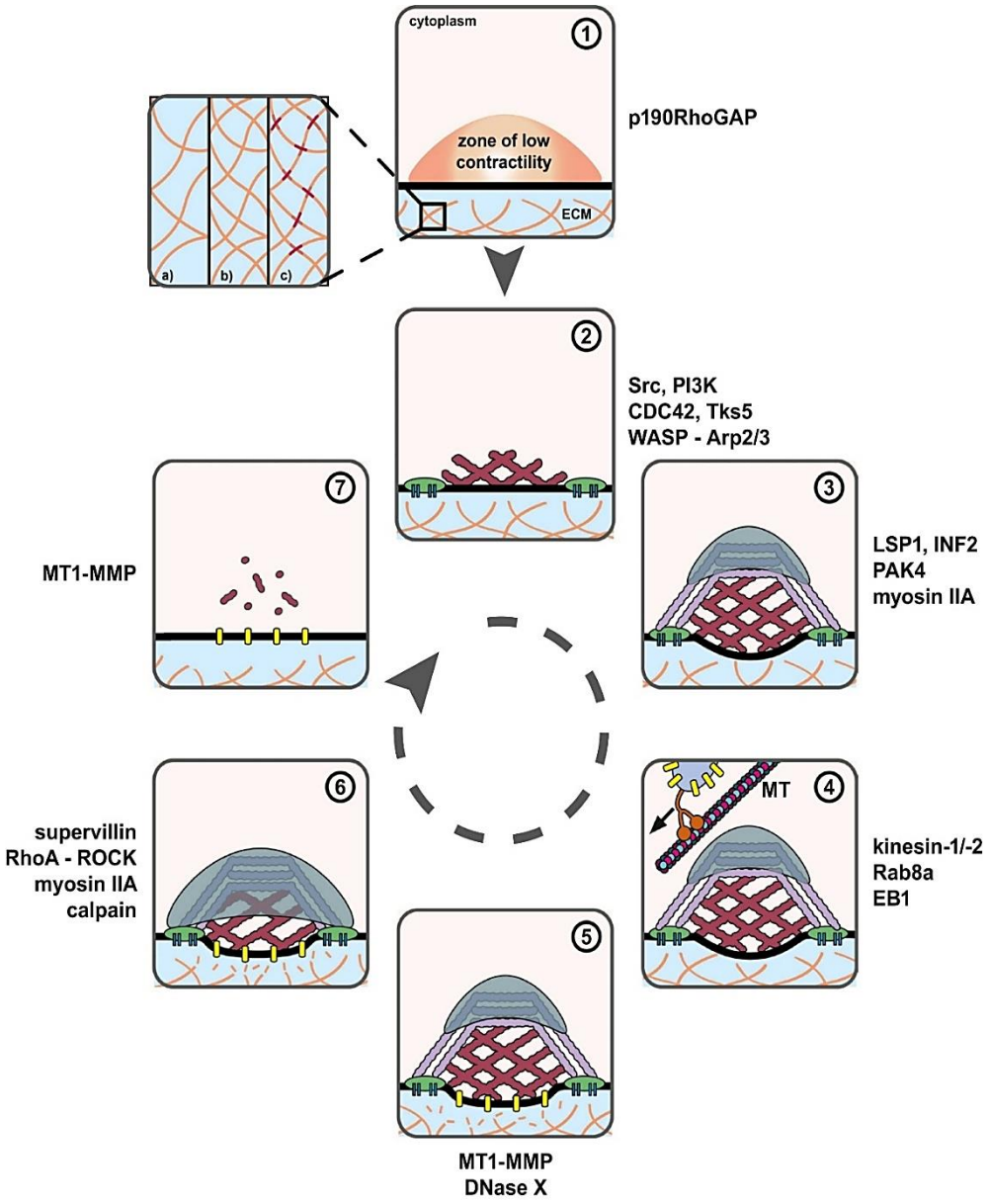

Figure 2: The podosome life cycle.

1) Assembly of podosomes takes place in zones of low contractility facilitated by RhoA inactivators like p190RhoGAP. Enlarged are fibers of extracellular matrix shown with increasing density (a-c) and additionally crosslinking in red (c). 2) Most important factors for the growing podosome core are named, and the recruitment of the ring is shown. 3) With the assembly of the podosome cap and its lateral cables connecting it to the ring, the podosome is fully formed. Its protrusive force is regulated by myosin IIA, LSP1 and INF2. PAK4 together with INF2 impact podosome size. 4) Via microtubule-dependent, kinesin-1 and -2 driven vesicle transport, MT1-MMP is brought towards the podosome. 5) The subsequent embedding of lytic enzymes like MT1-MMP and DNaseX as islets underneath the podosome core mediate substrate degradation. 6) The Rho-ROCK pathway as well as the recruitment of supervillin lead to a hyper-activation of myosin IIA, which in turn induces the dissolution of podosomes. Further, the cleavage of actin nucleators like WASP by calpain facilitates the podosome dissolution. 7) The MT1-MMP islets remain embedded in the plasma membrane after podosome dissolution and may act as seeds for actin nucleation and a podosome reassembly. From Weber et al., 2022.

In contrast to the assembly of podosomes, the disassembly takes place in a locally hyper-contractile environment[84]. Following the cap's role in size regulation and influence on podosome stability, many proteins of the podosome cap seem to be involved in the dissolution. Accumulation of supervillin, for example, recruits and activates myosin IIA[58], as well as a RhoA-dependent Rho-ROCK cascade[85]. Myosin IIA mediated hyper-contractility confines the core growth; further, a degradation of essential nucleators like WASP by calpain[86] supports the dissolution of the actin core, leaving long-lasting MT1-MMP islets at sites of previous podosome formation[83, 87]. Podosomes can reassemble at distinct sites, and the re-emergence is based on the previous deposition of MT1-MMP by podosomes, concluding the podosome life cycle. Since this life cycle is affected significantly by actin polymerization and microtubule contact, the cytoskeleton's regulation and dynamics are essential for the podosome's function and architecture.

3.3 Cytoskeleton

The cytoskeleton is an essential part of eukaryotic cells, including macrophages. Unlike a rigid structure, as the term may suggest, the cytoskeleton is a very dynamic structure characterized by a constant change and re-build, also referred to as a dynamic steady state[88]. It is, among others, involved in cell shape, locomotion, intracellular organization and signaling, cell division, and molecule trafficking[89-93].

The main structures contributing to the cytoskeleton are actin (F-actin)[94], tubulin (microtubules)[95], intermediate filaments[96], and septins[97]. While F-actin and microtubules are both structurally polarized into a plus end and a minus end, they perform different tasks to control and regulate cytoskeletal functions.

3.3.1 Actin

Actin is one of the most abundant proteins of eukaryotic cells and is present in cells as either G-actin (globular actin) or F-actin (filamentous actin). G-actin assembles to F-actin under ATP consumption and with the help of nucleating proteins like the Arp-2/3 complex. These actin microfilaments display as a non-rigid double-stranded polymer with a diameter of about 7 nm. The asymmetrical G-actin monomers can add up to filaments of several micrometers in length, characterized by ends with different kinetic constants, with a fast-growing plus end (“barbed end”) and a slowly growing minus end (“pointed end”)[98]. This leads to the so-called *treadmilling*, where simultaneous polymerization and depolymerization within one filament can be observed at the barbed and pointed end, respectively[88]. Although this is an ATP-intense process, it

provides a highly adaptable and fine-tuned system through tightly controlled polymerization and depolymerization.

Regulation of the actin cytoskeleton occurs, among others, via actin-associated proteins like nucleators (e.g., Arp2/3, formins), proteins for filament severing (e.g., gelsolin, cofilin)[99], as well as barbed-end capping and stabilization (e.g., tropomyosin). In addition, dynamic actin filaments are often cross-linked into bundles or networks to perform their functions in cells[100], such as motility, phagocytosis, and intracellular transport[101]. The effectors, as mentioned earlier, regulate actin dynamics. Furthermore, an alteration of actin dynamics upon microtubule contact was observed[62].

3.3.2 Microtubules

Microtubules (MTs), which are hollow, tube-like polymers of α/β-tubulin with a diameter of about 23 nm[102], are another vital component of the cytoskeleton involved in cell division, differentiation, cell morphogenesis, cell motility, and intracellular organelle transport[103-106]. A misregulation of microtubules and the subsequent defective cellular transport is linked to several diseases like ciliopathies, hereditary diseases associated with defects in cilia, and several neurodegenerative disorders, such as Parkinson's syndrome[107, 108]. Moreover, many efficient anti-cancer drugs target microtubules, as tumor growth is highly dependent on mitosis[109].

Like actin filaments, microtubules are polarized structures with a fast-growing plus end and a slowly growing minus end[102, 110, 111]. The latter is usually anchored at the microtubule organizing center (MTOC), which is also involved in the initial nucleation of a microtubule[105, 111, 112]. Although the *treadmilling* dynamics comparable to actin filaments were described for microtubules as well, *dynamic instability* is the most frequently observed mechanism. *Dynamic instability* describes the alteration between slow growth phases followed by a fast shrinkage (so-called catastrophe). At the growing plus end, freshly polymerized microtubules contain GTP-loaded β-tubulin in a so-called GTP cap with plus end stabilizing function. Because of GTP hydrolyzation in the MT lattice, predominantly GDP-bound subunits are present there[113]. The dynamics of microtubules are further affected by posttranslational modifications (PTMs) like acetylation, polyglutamylation, or tyrosination of the tubulin dimers after their polymerization[114, 115]. Different subsets of microtubules are created through this biochemical diversity of tubulin isoforms and PTMs and are referred to as tubulin code[116]. Additionally, those microtubule subsets were shown to co-exist in one cellular compartment[117]. This heterogeneity[118] is further extended by various microtubule-associated proteins (MAPs). These proteins are categorized into five different groups according to their function and/or

localization; namely (i) motile MAPs, motor proteins that generate forces and movement; (ii) enzymes that break or depolymerize microtubules; (iii) microtubule nucleators; (iv) the so-called structural MAPs; and (v) end-binding proteins that specifically associate with plus or minus ends of microtubules[119].

Autonomous microtubule plus end-tracking proteins (+TIPs), such as the end-binding proteins (EBs), can influence microtubule polymerization rates[120] and presumably alter the structure of microtubule ends as well[121]. These EBs can recognize and track growing microtubule ends[122,123] independently of other factors by their calponin homology domain (CH domain)[124] and their linker region[120, 125, 126]. Up to several hundreds of EB molecules can bind a growing plus end, forming a comet-like structure of 0.5–2.0 µm in length when visualized by fluorescence microscopy[127, 128]. In mammalian cells, three EB members are expressed, namely EB1, EB2, and EB3, with different binding characteristics[120, 129-133]. For example, EB1 and EB3 show a higher affinity for MT-stabilizing proteins than EB2[129, 134]. Further, EB1 and EB3 have a positive role in neurite outgrowth, while EB2 has a negative effect[135].

Besides directly affecting microtubules, EB proteins act as scaffolds for other +TIPs that do not autonomously bind microtubule plus ends. To this EB-dependent +TIPs belongs, for example, the cytoplasmic linker protein of 170 kDa (CLIP170). Initially, CLIP170 was characterized in mammals as “a link between endocytic vesicles and microtubules” by Pierre et al., 1992[136]. Later, CLIP170 was found to play a positive role in MT rescue and polymerization[137] and additionally serves as a hub for the minus end-directed motor dynein and its associated cargos at microtubule plus ends[138].

In combination with molecular motors, e.g., kinesins and dyneins, microtubules allow the vesicular transport of essential cargos to specific destinations[139] or play a role in recycling[138], respectively. For site-directed cargo trafficking, a tethering of microtubules +TIPs to specific structures of the actin cytoskeleton, such as podosomes, has to be ensured and regulated[69, 82, 83, 140].

3.4 Interaction between actin and microtubules

Historically the actin and the microtubule cytoskeleton were seen and researched as distinct networks with a specific structure, localization, and function. Although there are also shared regulatory proteins, most regulators have been analyzed in the context of individual F-actin or microtubule networks and dynamics[119, 141-144]. However, already in 1988[145], the close localization of F-actin and microtubules in neuronal growth cones suggested an interaction between these cytoskeletal components[146]. A growing body of evidence shows that these two networks are intertwined at multiple levels, affecting and regulating each other. Microtubule

ends probe the actin-rich cellular cortex influencing the F-actin structures[147, 148], and on the other hand, the microtubule catastrophe rate, for example, is influenced by the branched F-actin network density[149, 150].

Interestingly, test tube experiments could show that F-actin and microtubules do not interact directly. Therefore, additional proteins or complexes are needed with binding sites for either of these cytoskeletal components[151-154]. There are six basic mechanisms for the interaction of actin and microtubules[155], although there are more than a dozen, often context and cell-specific

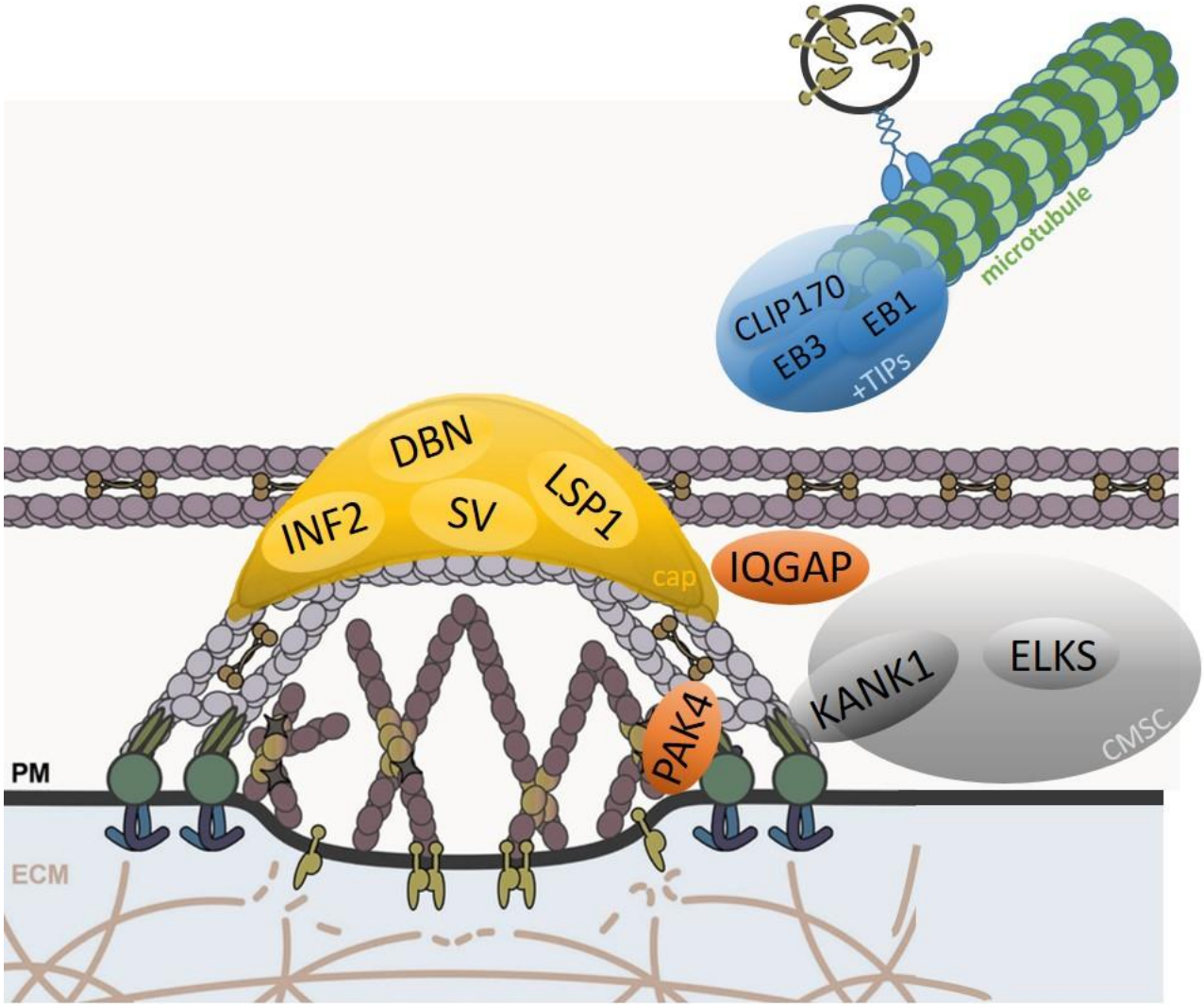

Figure 3: Podosome with proteins of interest.

Podosome structure with the known or assumed localization of different proteins of interest. INF2, SV, LSP1 and drebrin (yellow) were shown to localize to the podosome cap. PAK4 (orange) localizes to the inner podosome ring close to the actin core, KANK1 was published to bind talin and to be with ELKS part of the cortical microtubule stabilization complex (CMSC, gray), IQGAP (orange) is proposed to link microtubules to the CMSC. In the upper right corner a microtubule with +TIP proteins (blue) like EB1, EB3 and CLIP170 is depicted. An MT1-MMP containing vesicle gets transported by a kinesin towards the microtubule plus end. From Weber et al., 2022, modified.

proteins known that are involved in contact mediation. Podosomes are known to be contacted by microtubules, thereby altering the podosome dynamics[62]. Further, the site-directed tethering of microtubules to podosomes is needed to deliver cargo like MT1-MMP or soluble MMPs[69, 82, 83, 140]. However, a concerted effort to identify the proteins that mediate contacts between podosomes and microtubules has not been performed yet. Nevertheless, several proteins could be good candidates to play a role in podosome-microtubule interaction because of either their known actin and/or microtubule-binding or their exposed localization in the podosome structure, like the cap or the rim of the ring.

3.4.1 General regulator, general hub

PAK4

The p21-activated kinase 4 (PAK4) was found to localize in the podosome ring specifically; however, closer to the actin core than other ring proteins. It is known to drive the macrophage podosome turnover by affecting the Akt pathway in the ring-core transition zone[156]. A loss of PAK4 (or its kinase activity) led to a reduced number of podosomes, less degradation as well as changes in the podosome size[79]. PAK4 is not only affecting podosomes and actin but was reported as a critical effector in mitotic progression by regulating the spindle positioning for cell division[157, 158], microtubule dynamics and stability, as well as the regular centrosome assembly[159].

Further, PAK4 was proposed to play a role in the crosstalk between microtubules and the actin cytoskeleton via GEF-H1, a Rho-family guanine nucleotide exchange factor (GEF). PAK4 phosphorylation of MT-bound GEF-H1 releases it into the cytoplasm, where it promotes the dissolution of actin stress fibers[160], being therefore upstream of GEF-H1 mediated RhoA activation in response to extracellular matrix stiffness as well[161].

IQGAP1

IQ motif containing GTPase-activating protein 1 (IQGAP1) is known to be involved in anchoring microtubules at the cell cortex[147, 162]. Acting downstream of Rac1 and Cdc42, IQGAP recruits cortical partners like small kinetochore-associated protein (SKAP)[163], EB, and CLIP170[164] and is proposed to play a role in microtubule capture as well. Further, IQGAP1 is known to localize at invadopodia and interact with the so-called exocyst complex, which is suggested to support the targeting of MT1-MMP-containing vesicles to the degradative sites of invadopodia[165] and thus support the exocytosis and surface exposure of the matrix metalloprotease.

3.4.2 Cap localized candidates

The podosome cap is easily accessible by microtubules, being on the outer surface of the structure. For that reason, cap components are potential candidates for the site-directed interaction with microtubule +TIPs.

INF2

Inverted formin 2 (INF2) is expressed in humans in two isoforms – INF2-1 (localized at the ER) and the cytosolic INF2-2[166-168]. However, only the latter, also called the non-CAAX variant, is expressed in macrophages[57]. Therefore, in this study, INF2 refers exclusively to the INF2-2 isoform.

Additionally to its implication in podosome formation[57], INF2 was one of the first detected cap proteins of the podosome. It was found to regulate the podosome size, as siRNA-mediated depletion led to an increased podosome actin core (i.e., height and diameter). Moreover, INF2 was observed to regulate actin intensity oscillation of podosome cores[57].

Further, INF2 catalyzes the formation of actin filaments, but in contrast to most other formins, it can also sever and facilitate the depolymerization of F-actin[169, 170]. Structurally, INF2 is characterized by two domains, a DID (diaphanous inhibitory domain) and a DAD (diaphanous autoregulatory domain). The folding (i.e., the intermolecular binding of the two domains) regulates INF2 activity. G-actin competes with this binding; hence, INF2 is proposed to function as a G-actin sensor[171, 172]. Furthermore, INF2 was found to bind to, bundle, and stabilize microtubules[173-175]. It also regulates the specific acquisition of distinct posttranslational modifications of microtubules[171, 174].

Supervillin and LSP1

Supervillin (SV) and lymphocyte-specific protein 1 (LSP1) are proteins of the podosome cap as well. Both proteins bind to F-actin and myosin IIA, therefore competing for binding-sites. However, whereas LSP1 is enriched at precursor podosomes, especially at the leading edge, supervillin localizes preferentially to successor podosomes and becomes enriched at precursors immediately before their dissolution[58, 59].

Drebrin

Drebrin (developmentally regulated brain protein) was initially found in the embryonal chicken brain in 1985[176]. Therefore, it was analyzed mainly in a neuronal context and identified as an essential factor for neurite and dendrite elongation[177-182]. Nevertheless, in non-neuronal cells,

drebrin was detected and localized predominantly to actin-rich areas like lamellopodia or filopodia[183,184], and later also recognized as a regulator for actin rearrangement[185-189]. More recently in comparison to the actin interaction, the importance of drebrin for the capture of microtubule plus ends was discovered[190]. In neuronal cells, it was shown that the interaction of drebrin and the MT+TIP marker EB3 upregulates the number of MT entries into spines[191], as well as facilitates neurogenesis by microtubule insertion into filopodia[192, 193]. Additionally, an invasiveness promoting effect was shown for the drebrin/EB3 pathway[194]. Drebrin was found to localize to myotube (developmental stage of a muscle fiber) podosomes and interacts with EB3[195], but no substructure was determined. Importantly, drebrin was identified as a podosome cap protein in this work.

3.4.3 Cortical microtubule stabilization complex (CMSC) members

The cortical microtubule stabilization complex is a multi-protein complex that is proposed to connect microtubules to the actin cytoskeleton and integrin-containing adhesion structures like focal adhesions (FA)[196-200]. The CMSCs are strongly enriched at the leading cell edges, where they localize in close proximity to FAs but do not overlap with them[201-204].

KANK1

Kidney or KN motif and ankyrin repeat domain-containing proteins (KANKs) have been identified as components of integrin-adhesion complexes[200, 205]. Most analyses of KANK proteins were performed in focal adhesions (FA) and were found to localize in the peripheral FA zone termed the FA belt[197, 198]. Initially, KANK1 was described as a tumor suppressor in renal cell carcinoma[206]. Later, talin 1 and 2 were identified as interaction partners of KANK[196,198], assembling into a mechanically robust complex[207] that might act as an initiator for the cortical microtubule stabilization complex[196] and support crosstalk between actin and microtubules[207].

ELKS

The protein rich in the amino acids E, L, K and S (ELKS) forms a complex with CLASP (CLIP-associating protein) and LL5β around the rim of FAs where microtubules are anchored[202]. Complexes with ELKS are best known for their role in organizing presynaptic secretory sites[202, 208, 209]. It was shown that although ELKS does not bind microtubules directly, it is important for the recruitment of the cortical stabilization complex and, thus, for the microtubule stabilization[202].

3.5 Aim of the study

Despite the central importance of microtubule-based transport of components and regulators to and from podosomes, little is known about the dynamics and regulation of microtubule-podosome contacts. The main objective of this study was to shed some light on this topic with new approaches.

Development of a tool for statistical analysis of large amounts of podosome-MT+TIP contacts

Most studies concerning the analysis of contacts between MT+TIPs and other structures use video capture with subsequent manual counting and interpretation of single events. Consequently, the risk of biased analysis is fairly substantial and may result in an incorrect assessment given the limited number of analyzed events. Therefore, a new tool for a less biased and statistically more reliable contact analysis was needed. Hence, developing a software-based analysis that enables the analysis of huge data sets was the primary aim of this work.

Establishment of a pipeline for live cell contact analysis

An experimental pipeline for the newly developed contact analysis tool is equally required to be established. To be able to use the software tool extensively, a reliable set up of suitable marker proteins for the visualization of the target structures is required. This work aimed to find a functioning experimental protocol for the contacts between MT+TIPs and podosomes.

Analysis of targets for impact on podosome-MT+TIP contact

A further goal of this work was to use the newly developed tool and analyze the impact of different podosome-associated proteins and their effects on the podosome structure, particularly their potential impact on the MT+TIP-podosome contact behavior.

Analysis of functional consequences of altered contact behavior

Hence, the functional consequences of potential alterations in contact between microtubules and podosomes are of especial interest. These analyses included, among others, measurements of podosome lifetime and degradation capability as the concluding aim of this work.

4 Material

4.1 Devices

Properly maintained and qualified devices were used in this work and are listed in Table 1

Table 1: Devices

Device	Type, Provider
µMACS TM Separator	Milteny Biotech, Bergisch Gladbach (G)
Autoclave	Varioklav, Thermo Scientific, Rockford (USA)
Balance	440-47N, Kern, Balingen-Frommern (G)
Benches	Hera Safe, Thermo Scientific, Rockford (USA)
Cell counter	Neubauer chamber, Hartenstein, Würzburg (G)
Cell culture pump	Integra Vacusafe, Integra-Bioscience, Zizers (CH)
Centrifuges	5417R and 5810R, Eppendorf, Hamburg (G)
Film-cassette	Hartenstein, Würzburg (G)
Gel chamber horizontal (protein)	PeqLab, Erlangen (G); Bio-Rad, Hercules (USA)
Gel chamber vertical (DNA)	PeqLab, Erlangen (G)
Gel Electrophoresis Chamber	PeqLab, Erlangen (G)
Heatplate/ magnetic stirrer	IKAMAG RET, Janke&Kunkel GmbH&Co. KG, Staufen (G)
Hood pump	N811KN.18, KNF Laborport, Freiburg im Breisgau (G)
iBlot	Life Technologies, Carlsbad (USA)
Ice machine	AF-10, Scotsman, Vernon Hills (USA)
Incubator	Modell CB-S 170, Binder, Tuttlingen (G)
Incubator (shaking)	Certomat BS-1, Sartorius, Göttingen (G)
Microplate reader	Infinite M200, TECAN, Männerdorf (CH)
NanoDrop® ND-1000	PeqLab, Erlangen (G)
NEON™ Transfection System	Life Technologies, Carlsbad (USA)
PCR-cycler	Primus 25 advanced, PeqLab, Erlangen (G)
pH-meter	Mettler-Toledo GmbH, Gießen (G)
Photometer	Ultrospec 3100 pro, Amersham/GE Healthcare Europe, Munich (G)
Pipettes	2, 10, 20, 100, 200, 1000 µL, Eppendorf, Hamburg (G)
Power supplies	PeqPower 250/300, PeqLab, Erlangen (G)
Scanner	CanoScan 4400F, Canon, Amsterdam (NL)
Shaker	Edmund Bühler GmbH, Tübingen (G)
Sonifier	Digital Sonifier 250-D, Branson, Danbury (USA)
Transilluminator	Vilber Lourmat, ETX, Eberhardzell (G)
UV-Transilluminator + detector	ChemiDoc XRS, BioRad, Munich (G)
Voltohmmeter	Millicell® ERS-2, Millipore, Billerica (USA)
Vortex	REAX top, Heidolph Instruments, Schwabach (G); Janke&Kunkel GmbH&Co. KG, Staufen (G)
Water bath	Grant Instruments, Cambridge (GB)

4.2 Software and databases

Table 2 lists all software used for the analysis of the herein-shown data

Table 2: Software

Software	Developer
ContactAnalyzer	in-house software, unpublished
Endnote 20	Clarivate, Philadelphia (USA)
GraphPad Prism 9.4.0 (673)	GraphPad Software, San Diego (USA)
ImageJ 1.53q	National Institute of Health, Bethesda (USA)
InDesign	Adobe Systems Software Ireland, Dublin (I)
LAS X	Leica Microsystems, Wetzlar (G)
MS Office (Word, PowerPoint, Excel)	Microsoft, Washington, (USA)
Poji	in-house macro, see ref. Herzog et al., 2020[210]
TrackMate	ImageJ macro, see ref. Tinevez et al. 2017 [211]
Volocity Demo 6.1.1	PerkinElmer, Waltham (USA)
Zen Software	Carl Zeiss Microscopy Deutschland GmbH, Oberkochen (G)

4.3 Microscopes

4.3.1 Leica SP8

The SP8 system was primarily used for fixed cell samples.

Table 3: Leica TCS SP8 X System

Microscope	Leica DMi8
Objective 60x	63x HC PL APO Oil CS2 NA: 1.40 WD (mm): 0.14
Detectors	3x HyD, 2x PMT, 1x Trans-PMT
Laser lines (nm)	White light laser, pulsed (WLL): 470-670
Pinhole size	variable
Spectral separation	AOBS® + spectral detectors
Software	Leica LAS X SP8
Filters for fluorescence	Filter system (em.-color, dye): excitation | beamsplitter | emission L5 ET (green; AF488, GFP): BP 480/40 | FP 505 | em. BP 527/30 A (blue; DAPI): BP 340-380 | FP | LP 425 I 3 (green; AF488, GFP): BP 450-490 | FP | LP 515 N 2.1 (red; AF568, mCherry): BP 515-560 | FP | LP 590
UV-lamp	EL 6000 120W (LQHXP 120 LEJ)
Halogen lamp	100W 12V
Piezo focus drive	SuperZ Galvo type H (travel range: 1500 µm; reproducibility: 40 nm)
Tandem-Scanner	Variable: 512x512 @ 7 fps; max. 8192x8192 px; max. 3600 lines/s; 1x-48x zoom
Actively damped optical table	Newport

4.3.2 Visitron SD TIRF (before SoRa upgrade)

The Visitron-TIRF system was primarily used for live cell imaging experiments.

Table 4: Visitron SD TIRF System before SoRa upgrade

Microscope	**Nikon Eclipse TiE**
Objective 60x	60x Apo TIRF (corr.) Oil NA: 1.49 WD (mm): 0.13 (CS: 0.10-0.22 @ 23 or 37 °C) Pixel size in image (µm): 0.133 (w/ 2x intermediate magnification)
Objective 100x	100x CFI Plan Apo Lambda NA: 1.45 WD (mm): 0.13 Pixel size in image (µm): 0.080 (w/ 2x intermediate magnification)
Cameras	2x evolve-EM 512 (back-illuminated EM-CCD, 16µm pixel-size) Gain: 7 e-/ADU
Laser lines (nm)	Solid-state: 405/488/561/640
Spinning disk unit	Yokogawa CSU W-1 in dual-camera configuration 1) Confocal disk (50µm pinholes)
Emission filters spinning disk (for laser-related fluorescence)	Camera 1: DAPI, ET460 (W50) CFP ET470 (W24) GFP, ET525 (W50) Camera 2: YFP ET535 (W30) mCherry, ET609 (W54) CY5 ET700 (W75)
Dichroic in spinning disk unit	405/488/561/640 (used with the respective channels)
Dichroic for dual camera mode	561LP; 514LP
Fluorescence filters in the microscope stand	Filter system (em.-color, dye): excitation | beamsplitter | emission DAPI (blue; DAPI): BP 325-375 | DM 400 | BP 435-485 GFP (green; AF488, GFP): BP 450-490 | DM 495 | BP 500-550 TxRed (red; AF568, mCherry): BP 540-580 | DM 585 | BP 593-668
Dichroic mirrors in the microscope stand for TIRF and FRAP	TIRF-FRAP1: 405/488/561/640 rpc BS (Chroma; 2mm) TIRF-FRAP2: 442/514 rpc BS (Chroma; 2mm)
UV-lamp	SOLA-SM Light Engines, white light LED, 380-680nm
Transmitted light lamp	precisExcite, High-Power 525nm LED
Software	VisiView
Incubation unit	okolab bold line
FRAP-TIRF unit	Roper iLAS2 for FRAP&TIRF with all laser lines
Piezo focus drive	Ludl NanoPrecision PiezoZ, 350µm travel range
Motorized XY stage	Ludl BioPrecision2
Auto-focus	Nikon PerfectFocus system
Actively damped optical table	Newport

4.3.3 Visitron SD TIRF (after SoRa upgrade)

The Visitron-TIRF system was primarily used for live cell imaging experiments. Later also for fixed degradation assay samples.

Table 5: Visitron SD TIRF System after SoRa upgrade

Microscope	**Nikon Eclipse TiE**
Objective 60x	60x Apo TIRF (corr.) Oil NA: 1.49 WD (mm): 0.13 (CS: 0.10-0.22 @ 23 or 37 °C) Pixel size in image (µm): SpinningDisk: 0.183; SORA disk: 0.065
Objective 100x	100x CFI Plan Apo Lambda NA: 1.45 WD (mm): 0.13 Pixel size in image (µm): SpinningDisk: 0.110; SORA disk: 0.039
Cameras	2x Photometrics Prime 95B (back-illuminated sCMOS, 11µm pixel-size, 1200x1200 pixels)
Laser lines (nm)	Solid-state: 405/445/488/515/561/640
Spinning disk unit	Yokogawa CSU W-1 SoRa in dual-camera configuration 1) Confocal disk (50µm pinholes) 2) SoRa disk for super-resolution
Emission filters spinning disk (for laser-related fluorescence)	Camera 1: DAPI, ET460 (W50) CFP ET470 (W24) GFP, ET525 (W50) Camera 2: YFP ET535 (W30) mCherry, ET609 (W54) CY5 ET700 (W75)
Dichroic in spinning disk unit	405/488/561/640 (used with the respective channels) 445/515/640
Dichroic for dual camera mode	561LP; 514LP
Fluorescence filters in the microscope stand	Filter system (em.-color, dye): excitation | beamsplitter | emission DAPI (blue; DAPI): BP 325-375 | DM 400 | BP 435-485 GFP (green; AF488, GFP): BP 450-490 | DM 495 | BP 500-550 TxRed (red; AF568, mCherry): BP 540-580 | DM 585 | BP 593-668
Dichroic mirrors in the microscope stand for TIRF and FRAP	TIRF-FRAP1: 405/488/561/640 rpc BS (Chroma; 2mm) TIRF-FRAP2: 442/514 rpc BS (Chroma; 2mm)
UV-lamp	SOLA-SM Light Engines, white light LED, 380-680nm
Transmitted light lamp	precisExcite, High-Power 525nm LED
Software	VisiView
Incubation unit	okolab bold line
FRAP-TIRF unit	Roper iLAS2 for FRAP&TIRF with all laser lines
Piezo focus drive	Ludl NanoPrecision PiezoZ, 350µm travel range
Motorized XY stage	Ludl BioPrecision2
Auto-focus	Nikon PerfectFocus system
Actively damped optical table	Newport

4.4 Disposables

Table 6: Disposables

Name	Type, provider
6/12- well plates	Sarstedt, Nümbrecht (G)
Cannulas	B. Braun Melsungen AG, Melsungen (G)
Coverslips (12 mm and 18 mm)	Glaswarenfabrik Karl Hecht GmbH & Co KG, Sondheim v. d. Rhön (G)
Disposable scalpel	B. Braun Melsungen AG, Melsungen (G)
Disposable syringe 2 ml, 5 ml, 20 ml	B. Braun Melsungen AG, Melsungen (G)
Disposable tips 10, 200, 1000 µl	Sarstedt, Nümbrecht (G)
Filtopur S, seril filtes 0.2 µm	Sarstedt, Nümbrecht (G)
Glass slides	Glaswarenfabrik Karl Hecht GmbH & Co KG, Sondheim v. d. Rhön (G)
Kodak X-Omat AR films	GE Healthcare, München (G)
Parafilm „M“	American Can Company, Jersey City (USA)
Pasteur pipettes, glass	Brand, Wertheim (G)
Petri dishes 12 mm + 22 mm, WillCo-dish® glass bottom	WillCo Wells B.V., Amsterdam (NL)
Reaction tubes (falcon) 15, 50 ml	Sarstedt, Nümbrecht (G)
Reaction tubes 0.5, 1.5, 2 ml	Sarstedt, Nümbrecht (G)
Serological pipettes 1, 5, 10, 25 ml	Sarstedt, Nümbrecht (G)
Slide-A-Lyzer Dialysis Cassettes	Life Technologies, Carlsbad (USA)
Sterucup Vaccum filters 0.2 µm with flask	Millipore, Billerica (USA)
Tweezers	Manufactures D’Outils Dumont SA, Montignez (CH)

4.5 Kits and agents

Table 7: Kits

Name	Provider
Neon transfection system	Life Technologies, Carlsbad (USA)
Pierce BCA Protein Assay Kit	Thermo Scientific, Karlsruhe (G)
Pierce Silver Stain for Mass Spectrometry	Thermo Scientific, Karlsruhe (G)
TGX FastCast Acrylamide Kit (10 % + 12 %)	BioRad, München (G)

4.6 Growth media, additives, antibiotics, enzymes

Table 8: Growth media, additives, antibiotics

Name	Type, provider
RPMI1640 basic media	Thermo Scientific, Karlsruhe (G)
L-Glutamine-Penicillin-Streptomycin-solution (100x)	Sigma-Aldrich, Seelze (G)
Accutase	eBioscience, San Diego (G) & Serana, Pessin (G)
Autologous human serum	Transfusionsmedizin, Uniklinik Hamburg-Eppendorf (G)

4.7 Chemicals

4.7.1 Chemicals

Table 9: Chemicals

Name	Type, provider
1,4-diazabicyclo[2.2.2]octane 25 mg/ml	Sigma-Aldrich, Saint Louis, MO, USA
2-Propanol	Merck, Daermstadt (G)
BlueBlock	Serva, Heidelberg (G)
BSA	Roth, Karlsruhe (G)
Calciumchloride	Roth, Karlsruhe (G)
Caliumdihydrogenphosphate	Roth, Karlsruhe (G)
CD14 beads	Miltenyi Biotec, Teterow (G)
Developersolution (WB)	AGFA, Mortsel (BE)
Dimethylsulfoxide >99.5%	Roth, Karlsruhe (G)
Dinatriumhydrogenphosphat	Roth, Karlsruhe (G)
DPBS	Thermo Scientific, Karlsruhe (G)
DQ-BSA	Life Technologies, Carlsbad (USA)
ECL substrate (Femto)	Thermo Scientific, Karlsruhe (G)
ECL substrate (Pico)	Thermo Scientific, Karlsruhe (G)
EDTA	Roth, Karlsruhe (G)
Ethanol 96 % denatured	Roth, Karlsruhe (G)
Fixations solution (WB)	AGFA, Mortsel (BE)
Formaldehyd 16 % methanol-free	Roth, Karlsruhe (G)
Formaldehyde solution 37 %	Sigma-Aldrich, Seelze (G)
Glutaraldehyde 20%	Roth, Karlsruhe (G)
Glycin >99 %	Sigma-Aldrich, Seelze (G)
Hoechst 33342	Life Technologies, Carlsbad (USA)
hydrochloric acid 2 N	Roth, Karlsruhe (G)
Incidin Plus Disinfection	ecolab, Saint Paul (USA)
Lymphocyte separations medium 1077	PAA Laboratories, Pasching (G)
Mowiol 4-88	Roth, Karlsruhe (G)

Name	Type, provider
NHS rhodamine	Thermo Fisher Scientific, Waltham, MA (USA)
Phosphatase inhibitors	Roche, Penzberg (G)
Protease inhibitors	Roche, Penzberg (G)
Saccharose	Roth, Karlsruhe (G)
SDS	Roth, Karlsruhe (G)
Sodium chloride	Roth, Karlsruhe (G)
Sodium chloride	Roth, Karlsruhe (G)
Sodiumium hydroxide 32 %	Roth, Karlsruhe (G)
Tris-HCl	Sigma-Aldrich, Seelze (G)
Triton X-100	Sigma-Aldrich, Seelze (G)
Tween 20	Sigma-Aldrich, Seelze (G)

4.7.2 Buffers

In the following, the compositions of all used self-made buffers are described.

Monocyte buffer	DPBS pH 7.4 2 mM EDTA 0.5 % (w/v) human serum albumin
Monocyte culture medium	RPMI 1640 20% autologous human serum [prepared in-house] 100 U/ml penicillin and 100 µg/ml streptomycin
Lämmli loading buffer 5x	bromphenol blue 100 mg glycerine 3.5 ml SDS 1.5g 1 M Tris-HCL 3.2 ml mercaptoethanol 2.5 ml

4.8 Plasmids and siRNA

4.8.1 Plasmids

Table 10: Used plasmids for overexpression

Target	Origin of construct	Obtained/generated
LifeAct-RFP	ibidi / J.Riedl	Aug 2011
EB1-GFP	Mimori-Kiyosue	Feb 2005
EB3-GFP	Marina Mikhaylova	Mar 2018
CLIP170-GFP	N.Galjart	Jun 2006
Drebrin-GFP	W.Peitsch	Feb 2002

4.8.2 SiRNA

Table 11: Used siRNA for the depletion of +TIP markers or podosome components

Target	Sequence
DBN	5'- GGAAACAGCAGACUUUAGA -3'
EB1	5'- UGACAAAGAUCGAACAGUU -3'
EB3	5'- CAGCAAACUUCGUGACAUC -3
ELKS	5'- GUGGGAAAACCCUUUCAAU -3'
INF2	5'- CCAUGAAGGCUUUCCGGGA -3'
IQGAP	5'- GAACGUGGCUUAUGAGUAC -3'
KANK1	5'- CAGAGAAGGACATGCGGAT -3'
LSP1	5′- UGGAGACAUGAGCAAGAAA -3'
Luciferase	5′- AGGUAGUGUAACCGCCUUGUU -3'
PAK4	5'- GGUGAACAUGUAUGAGUGUTT -3'
SV	5'- CAGCCAUAAGGAAUCUAAAUAUGCU -3'

4.9 Antibodies

4.9.1 Primary antibodies

Table 12: Used antibodies (and dilution) to detect podosome components or +TIP markers. Dilution in Western blots (1:1000) or endogenous stainings (1:100), AF: AlexaFluor fluorophores with excitation wavelength in nm.

Target	origin species	source
DBN	rabbit	Abcam & Invitrogen
EB3	rabbit	Abcam
ELKS	mouse	Sigma Life Science
INF2	rabbit	Sigma Atlas Antibodies
IQGAP	mouse	Santa Cruz
KANK1	rabbit	Sigma Atlas Antibodies
LSP1	rabbit	Sigma Atlas Antibodies
PAK4	rabbit	Cell Signalling
SV	rabbit	E. Luna lab,
primary AF488-conjugated MT1-MMP	mouse	biotechne R&D Systems
isotype control for anti-MT1MMP AF488	mouse	biotechne R&D Systems

4.9.2 Secondary antibodies

Used antibodies and staining solution with dilutions. WB: immunochemical staining after Western Blotting; IF: immunofluorescent staining; AF: AlexaFluor fluorophores with excitation wavelength in nm.

Table 13: Secondary antibodies and staining solutions

Name	species	type	dilution WB	dilution IF	Provider
Anti-mouse-HRP	sheep	polyclonal	1:5000		GE Healthcare (USA)
Anti-rabbit-HRP	donkey	polyclonal	1:5000		GE Healthcare (USA)
Anti-mouse-AF488/568/647	donkey goat	polyclonal		1:200	Thermo Scientific, Karlsruhe (G)
Anti-rabbit- AF488/568/647	donkey goat	polyclonal		1:200	Thermo Scientific, Karlsruhe (G)
Anti-goat- AF488/568/647	donkey	monoclonal		1:200	Thermo Scientific, Karlsruhe (G)
Phalloidin AF405/488/568/647				1:50	Thermo Scientific, Karlsruhe (G)

5 Methods

5.1 Cell biological methods

5.1.1 Isolation and cultivation of primary human macrophages

Primary human monocytes were isolated from leukocyte fraction of buffy coats (kindly provided by Frank Bentzien, UKE Transfusion Medicine, Hamburg, Germany). These buffy coats are a side product of whole blood donations and consist mostly of leukocytes and thrombocytes, which make up about 10 % of the whole blood donation. The isolation of monocytes was performed as described before[212] by sucrose density gradient. Following this protocol, 15 ml Ficoll (leucocyte separation medium, LSM) was layered with 20 ml blood and centrifuged for 30 min at 4 °C with 460 xg, using smooth acceleration and brake. Next, the whitish leukocyte fraction was transferred into a fresh 50 ml falcon tube and filled up with cold RPMI 1640 medium for washing twice for 10 min at 4 °C and 460 xg. This enriched leukocyte fraction was then resuspended in 1.5 ml sterile monocyte buffer (see 4.7.2) and 250 µl of CD14 antibody-coupled magnetic beads. After incubation for 15 min on ice, this mixture was loaded on an MS^+ Separation column after placing it in a magnetic holder and equilibrated with 1 ml cold monocyte buffer. Trapped $CD14^+$ monocytes were washed twice on the column with 1 ml monocyte buffer. After removing the column from the magnet holder, they were eluted with 3 ml monocyte buffer into 15 ml cold RPMI 1640. Thereafter, the cells were counted and seeded on 6-well plates at a density of 2×10^6 cells per well. After enough time for the monocytes to adhere, around 5 hrs, the RPMI was replaced by 1.5 ml monocyte culture medium (see 4.7.2). Monocytes were cultivated in an incubator at 37 °C, 5% CO_2, and 90 % humidity and differentiated into macrophages. After 6 days, the culture medium was replaced by a fresh monocyte culture medium.

5.1.2 Cell transfection and siRNA experiments

Different constructs were overexpressed in human macrophages to visualize podosomes and MT+TIPs in living cells or for visualization of other podosome components. All used constructs are listed in Table 10. The transfection of cells with DNA-plasmids was performed with cultured cells 6-10 days post-isolation. For the transient transfection with a DNA-plasmid or siRNA, adherent macrophages were washed twice with 1 ml sterile DPBS and then detached by 500 µl accutase treatment for 1 h at 37°C. Accutase treatment was then stopped by the addition of 500 µl monocyte culture medium. The cells were resuspended in the solution and transferred into a 15 ml tube. Hereafter, the cell suspension was centrifuged at 460 xg for 5 min at room temperature. The supernatant was removed, the cells were resuspended in DPBS and counted. The appropriate amount of cells were subsequently used for the transfection.

Per 1x10^5 macrophages, 0.5 µg plasmid was used, following the manufacturer's protocol for transfection with the Neon system using 2 pulses for 40 ms at 1000 V. The transfected cells were then immediately transferred into RPMI and seeded in an 8-well ibidi chamber or 12-18 mm coverslips.

For the depletion of target proteins, macrophages were transfected with respective siRNAs (listed in Table 11) with the Neon electroporation system. Cells were detached with accutase, washed with PBS, and counted as described above. Per 1 million macrophages, 5 µl of 20 µM siRNA was used, following the manufacturer's protocol for transfection using 2 pulses for 40 ms at 1000 V. The transfected cells were then immediately transferred into 1 ml RPMI per 1 million cells and seeded into a 6-well plate. Cells were used for subsequent experiments 72-76 hrs after siRNA transfection.

5.1.3 Immunofluorescence staining

For the endogenous visualization and localization data, immunofluorescence stainings were performed. For that, cells of different conditions or treatments were seeded in a density of 1 x 10^5 cells per 12 mm diameter coverslip. Cells were fixed at least 5 hrs post-seeding with 4 % methanol-free formaldehyde for 10 min at RT; in the case of PTM staining, an additional pre-fixation with 32 % ice-cold methanol was performed. Afterward, the cells were permeabilized by incubation with 0.1 % Triton X-100 in PBS for 10 min at RT and subsequently blocked with a blocking solution (3 % BSA, 2 % NGS in PBS) for 3 hrs at RT. Next, cells were incubated with primary antibodies with respective dilutions solution (see antibody Table 12) in blocking over night at 4 °C. The next day, cells were washed twice with PBS and treated with the respective fluorescence-coupled secondary antibody and phalloidin for 4 hrs at RT in the dark. Coverslips were after another two washing steps with PBS mounted with Mowiol containing mounting medium and stored at 4 °C until microscopy.

5.1.4 Degradation Assay

Rhodamine-gelatin was made following the protocol by Chen and Ko (1994)[213] by labeling gelatin with NHS rhodamine. Coverslips were coated with labeled rhodamine-gelatin, fixed in 0.5 % glutaraldehyde, and washed in RPMI 1640 and monocyte culture medium. Cells (12 days to 16 days post isolation) were seeded at a density of 5×10^4 cells on the coated coverslips, and the cells were incubated to attach for 1.5 hrs in a monocyte culture medium. Further, they were cultured for another 6-8 hrs (in culture medium or RPMI with DMSO/treatment). Subsequently, the coverslips were fixed with 4 % formaldehyde in PBS for 10 min and stained with Alexa Fluor 488-phalloidin. Coverslips were mounted using Mowiol

containing 1,4-diazabicyclo[2.2.2]octane (25 mg/ml) as an anti-fading reagent. Matrix degradation values were determined as the ratio of fluorescent intensity under each cell versus areas of identical size adjacent to cells using ImageJ. The laser strength was not changed between measurements for comparability of fluorescence intensity levels. Three independent donors were analyzed for each condition, with at least 15 fields of view (over 100 cells) per condition. Statistical analyses were performed using a two-tailed-sample t-test or ordinary one-way ANOVA.

5.1.5 Collection of cell lysates

The detached and counted cells were centrifuged and resuspended in 100 µL lysis buffer containing a protease and phosphatase inhibitor cocktail. The detergent Triton X-100 at a final concentration of 1 % was used to disrupt the cell membrane. After incubation on ice for 10 min, the cell debris was pelleted by centrifugation with 14000 g for 25 minutes at 4 °C. Next, 25 µL Lämmli loading buffer (5x) was added, and the lysates were heated for 10 min to 96 °C for denaturation.

5.1.6 FACS analysis

For the analysis of the amount of MT1-MMP at the surface of cells with different knockdowns, respective cells were detached using 10 mM EDTA in DPBS for 1 h. Cells were pelleted by 350 xg centrifugation for 5 minutes and resuspended in 100 µL FACS-staining buffer (BSA in DPBS, sterile). Per million cells, 5 µl primary Alexa-488 conjugated antibodies against MT1-MMP or 12.5 µl isotype control were added to the samples and incubated for 1 h at room temperature in the dark. Cells were washed with 1 mL DPBS, centrifuged, and resuspended in 100 µL FACS analysis buffer (containing EDTA). After this point, the cells were constantly kept on ice. FACS were performed at the CANTO II with the 488 nm laser. The gain of forward scatter, side scatter, and 488 detectors were kept the same throughout all measurements.

5.1.7 Microscopy

5.1.7.1 Confocal laser scanning microscopy – fixed cells

The SP8 was used for images that required better resolution. Hence, the following laser scanning microscopy settings were used for profile and localization analysis in fixed samples.

5.1.7.1.1 Profile analysis

The following parameters were set to acquire images used to analyze the podosome structure. The images were captured with a zoom of 3.0 and a resolution of 872 x 872 pixels, equivalent to 61.51 x 61.51 µm. For the profiles, a z-stack was acquired with a step size of 0.16 µm. These settings were maintained for all conditions to ensure comparability.

Table 14: Parameters for image acquisition for profile analysis

	Target protein	F-actin	F-actin	EB3M
Channel	488	405	568	568
Line average	2	1	2	2
Line accumulation	1	1	1	1
Frame average	2	1	2	2
Frame accumulation	1	1	1	1
Laser power	4	9	1	1
Pinhole	0.80	0.5	0.21	0.21
Smart gain	400	100	116	100

5.1.7.1.2 Localization analysis

The localization in human primary macrophages was already published for most here analyzed proteins. Thus, this work has taken a closer look at targets that have not been characterized yet, especially concerning podosomes.

5.1.7.2 Spinning disk TIRF microscopy – live cell & fixed cells

The spinning disk TIRF microscopy system was used for live cell and fixed cell acquisition. The following chapters will describe the parameters used.

5.1.7.2.1 MT-Podo-Analysis

Here 30-minute movies were acquired for the contact analysis. Therefore, cells were prepared in an 8-well ibidi multiwell. Wildtype or cells depleted of different target proteins were used for the assay. The cells were transfected to overexpress LifeAct-RFP together with EB3-GFP or, in the case of the initial test, CLIP170-GFP or EB1-GFP. After 4.5 hrs of incubation, the acquisition was started. The movies were taken with a frame rate of two to three channels per 2 seconds. In the beginning, also to establish the assay, TIRF in two channels (488 nm and

568 nm) and one confocal channel were acquired (488 nm). Later, for less damage to the samples, only two channels were acquired, TIRF in two wavelengths (in nm): 488 and 568.

5.1.7.2.2 Degradation Assay acquisition

For fast acquisition of degradation assay coverslips, the 60 x objective of the spinning disk system was used. These ensured a more extensive field of view while having a minimum of bleaching through the fast acquisition time. Further, stacks of 10 focal planes were taken, accounting for shifts in the z-plane and ensuring all layers of the rhodamine-gelatin were acquired.

5.2 Biochemical methods

5.2.1 SDS-Page

For size-dependent separation of the proteins, SDS-PAGEs with 12 % acrylamide gels were made following the manufacturer's protocol. Further, the lysates were loaded on the gels and separated across an electric field of 120 V for 120 minutes. The normalization of protein levels was conducted based on the number of cells that were lysed for the respective lysate. After the running time of the SDS-PAGE, the gel was freed of the BioRad-Gel system and continued to be used to blot on a PDMS-membrane.

5.2.2 Western Blot

Using the iBlot2 system, the proteins were transferred from the acrylamide gel on a nitrocellulose membrane. The membrane was blocked using BlueBlock 1x in TBS - T buffer for a minimum of 3 hrs at RT. In the case of targets that were prone to background bands, the blocking was performed over night at 4 °C. For the subsequent staining, the membrane was incubated with primary antibodies diluted in 1 x BlueBlock TBS - T at 4 °C overnight. Between primary and secondary antibodies incubation, the membrane was washed three times with TBS - T for 20 minutes each. The Pico or Femto chemiluminescence kit was used to develop the Western Blot. All used antibodies are listed in Table 12. For the development traditional developer, LiCor, or Cytvia, were used.

5.3 Podosome-MT+TIP contact tool

A detailed analysis of contacts between podosomes and MT+TIPs has not been performed until now, although contact events between microtubules and podosomes, as well as their impact on podosome dynamics, were already observed earlier[62]. Primary human macrophages display numerous (>300) relatively stable podosomes, allowing, on the one hand, to study contacts between MT+TIPs and podosomes in a detailed manner. On the other hand, the large number of podosomes requires automated analysis, especially to prevent researcher-biased selection of targets.

5.3.1 ContactAnalyzer

This tool is created for contact analysis from two channels of interest. The initial objects of interest are podosomes and microtubules. Basically, this tool uses the tracks and spots created by the ImageJ plugin TrackMate[211]. What type of movie information is used to generate the TrackMate reference/channel file does not matter to this program – so it is also usable for any other source of TrackMate files in XML format.

5.3.2 Definition of terms

Because of the complexity of the contact analysis, a defined usage of terms is necessary. For that reason, in the following part, the main terms used and how they were defined for this work are explained.

Reference file

The reference file is a TrackMate-generated XML file based on the less dynamic target, i.e., podosomes in the present case. It consists of spots and tracks as defined below.

Channel file

The channel file is a TrackMate-generated XML file as well, consisting of spots only. Again, this is suited for the more dynamic target; here, it was used for the MT+TIPs.

Spots

Spots are signals that are detected by TrackMate and are defined by a coordinate with x, y, t, where t is the respective frame of the live cell movie. The spot size is determined in TrackMate as blob size (8 px for podosomes; 5 px for MT+TIPs).

Tracks

Tracks are a list of spots that are linked from frame to frame. Here, tracks follow podosomes over the movie with the number of frames (and corresponding time) displaying the podosome lifetime.

Detection diameter

The detection diameter is a value on which the intersection calculation of the ContactAnalyzer is based. The detection diameter can be freely chosen for the podosomes ("referenceDiameter") and MT+TIPs ("channelDiameter"). If the detection diameter is wider than the blob size (i.e., object size), contacts will be detected in the vicinity of podosomes.

Raw contact

A raw contact is a detected overlap of the detection radius of a podosome with the detection radius of an MT+TIP. The intersection area calculation is described in 5.3.4.3.

Consecutive contact

A consecutive contact is a list of raw contacts that are linked from frame to frame. Therefore, the raw contact with the most overlapping area is calculated, and a detailed description of the method, based on an intersection matrix, can be found in 5.3.4.4.2. A consecutive contact is MT+TIPs contacting podosomes over several subsequent frames; thus, the corresponding time equals the contact duration.

5.3.3 Workflow

For the analysis of contacts, live cell movies with the Visitron SD-TIRF system were acquired. TIRF was used to reduce the acquired signals to the focal plane of podosomes, which are located at the basal part of macrophages adhering to the glass. Movies were acquired for 30 minutes with a frame rate of two seconds per frame. For these live cell movies, different conditions were used, e.g., macrophages where podosome components are depleted or different +TIP markers were overexpressed.

The ImageJ plugin TrackMate[211] XML files containing the coordinates and tracks of podosomes and MT+TIP coordinates of microtubule plus ends were created. The finding of coordinates is based on the LoG detector function of TrackMate, which applies Laplacian of Gaussian filter to the image with a user-defined threshold (sigma) and a blob size that fits the targeted object, i.e., here, 5 px for microtubules and 8 px for podosomes. TrackMate calculates in the Fourier space, and in the filtered image, maxima are found. Further, with the help of the LAP tracker, spots of podosomes are combined into tracks in two steps: first, spots are linked from frame to frame to build track segments. Second, those are combined in a further step

according to defined parameters like gap closing. Here, applied parameters included a maximal distance of 4 px for the frame-to-frame linking and allowed gap-closing of maximal one frame missing and a maximal distance of 4 px as well. No track splitting or merging was assumed, and no track filtering inside TrackMate was applied. The calculations and results were saved in XML format.

As explained below, those generated XML files were used as input files for the developed ContactAnalyzer program to extract and generate statistical data for tracks, spots, and contacts. The resulting output data files (in more detail described in 5.3.5) were further analyzed using Excel and GraphPad Prism.

5.3.4 ContactAnalyzer function

The program always processes one reference file (podosome channel) with one channel file (MT+TIP channel). This can be done with a single pair (single) or with a whole directory full of files matching a specific name pattern (directory). Those are the two basic commands. These commands are followed by a list of parameters, defining which operations and customizations are required for this data run. In the end, a CSV file will be provided with the most important statistics, a txt file with the log output, and, depending on requested parameters, additional detailed files.

5.3.4.1 Execute ContactAnalyzer

The ContactAnalyzer program is based on the .NET 6 technology that is used to provide a console application. That means there is no graphical user interface, so it requires a command line to be started. Those commands were written into a batch file (.bat) to start the ContactAnalyzer with the respective parameters for a more user-friendly execution. This makes running different configurations on multiple data sets more manageable and consistent.

The following commands were used:

- directory (-d) with referenceFileSuffix (-r) and channelFileSuffix (-c): Absolute or relative path to the directory where the XML files are saved, with suffix patterns to match respective podosome and MT+TIP files.
- referenceDiameter <integer>: The diameter used for intersection calculation for spots in a reference file, i.e., detection diameter, uses the blob size given in TrackMate XML when not defined here. For graphs in this work, a detection diameter of 12 px was used if not stated otherwise.

- channelDiameter <integer>: Diameter used for intersection calculation for spots in channel file. The diameter of 5 px was defined here as well as in TrackMate for MT+TIPs.
- drawImages (switch): Draws images to a subfolder in the output directory with the processed podosome spots in blue and MT+TIPs in red.
- outputPath: The folder for output files (absolute or relative) defines where the generated files should be saved.
- outputFilename: Name of output files without a file extension. Further reports will have automatic suffixes (like <filename>.trackLength.CSV).
- writeParametersToCsvResultFile (switch): Writes the parameters used to calculate result into CSV file.
- writeTrackLengths (switch): Writes a separate CSV with statistics of track lengths.
- writeContactDurations (switch): Writes a separate CSV with statistic of contact durations.
- ignoreTracksInFirstOrLastFrame (switch): Ignores every track that begins in the first frame and/or ends in the last frame. Those tracks would live outside of the scope and influence results. This filter was not used for graphs in this work if not stated otherwise.
- writeMeanTrackContacts (switch): Writes a separate CSV with statistics of mean track contacts in each frame for each track length.
- minimumTrackLength <integer>: filters tracks for defined minimum length before calculating contacts in each frame for each track. If not stated otherwise, a minimum track length of 30 frames (corresponding to one minute) was used.

For data quality-check the following commands are used:
(The results are not saved as CSV file.)

- intersectionAreaFrequency (switch): Write intersection area frequency, i.e., how often certain areas were detected.
- numberOfContactsPerSpot (switch): Write number of contacts per spot.

Example text of a batch file:

..\TrackContactAnalyzer.exe directory -r "w?TIRF561.xml" -c "488*.xml" --referenceDiameter "12" --channelDiameter "5" -d D:\ResultsXML_Files\ctrl --outputPath "D:\Results\#PODO-MT-CONTACTS\Results\ctrl" --drawImages --intersectionAreaFrequency --numberOfContactsPerSpot --writeParametersToCsvResultFile --writeTrackLengths --writeContactDurations --writeMeanTrackContacts --minimumTrackLength 30

5.3.4.2 Reading of inputs and filtering

By referring to a directory with -d in the command line (for example, D:\ResultsXML_Files\ctrl), the program is guided to the prepared XML files. They are read and the usage of naming patterns matches respective reference (podosome) and channel (MT+TIPs) files. The suffix of the files identifies the file as a reference or channel file (-r "w?TIRF561.xml" -c "488*.xml"); the part in front of the suffix has to be identical to be matched. In the case of active filters (XML given filter; command MinimumTrackLength, Starts in the first frame/Ends in the last frame), the reference file will only proceed with the selected files. Further, the scientific notation in XML files gets corrected for subsequent calculations.

5.3.4.3 Calculating raw contacts

The intersection of two spots is calculated via a circular intersection of both spot coordinates and their given detection diameter (two-dimensional).

5.3.4.3.1 Process

For calculating a raw contact, first, a podosome track is selected. Then, for each spot of this track, all MT+TIP spots of the respective frame are checked for an overlap with the detection diameter of the podosome. If the spots have an intersection area of >0, this is a raw contact and will be stored. The program will continue frame by frame until the end of the track. Subsequently, this process will be repeated with the next track until all tracks are examined. For performance reasons, this process runs parallelly for several tracks.

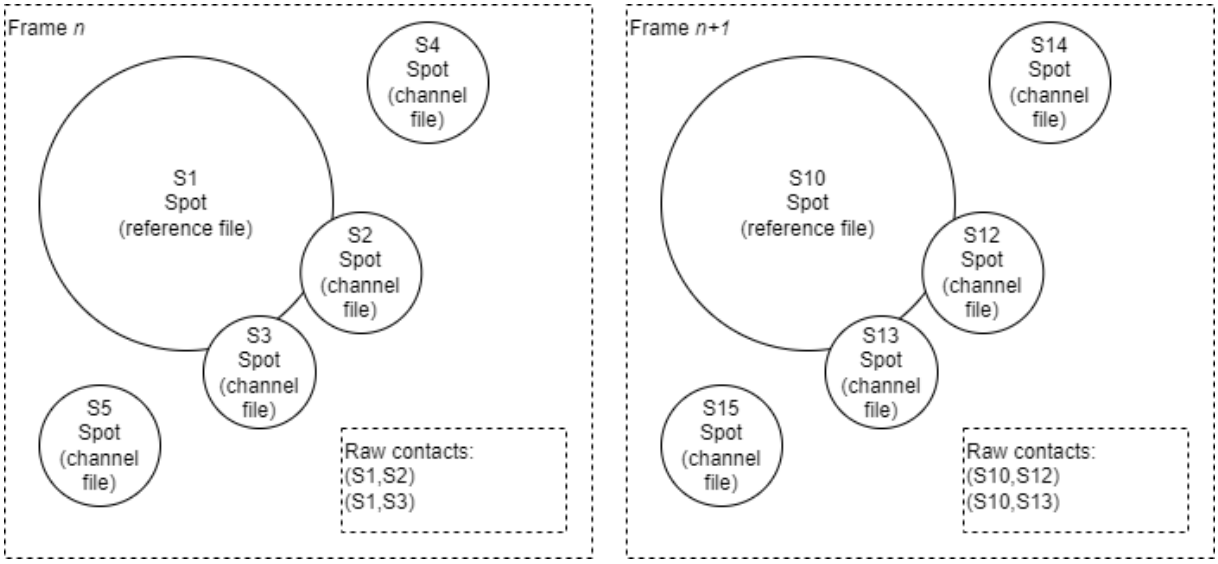

Figure 4: Raw Contact Example.

Two subsequent frames with a detection radius of podosome track with two spots (S1 in frame n, S10 in frame n+1) and several MT+TIPs (Spot channel file). S2, S3, S12 and S13 show an overlap with spots of the podosome track. Four raw contacts (S1, S2); (S1, S3); (S10, S12) and (S10, S13) will be stored as raw contact.

5.3.4.3.2 Intersection calculation

Before the circle-circle intersection area is calculated for a spot pair, there are three pre-tests to reduce the needed computational power. Since for all calculations the distance of the centers of both spots is needed, the following computation is done for each spot pair:

Distance between C0 and C1 (Pythagorean Theorem)

$$d = \sqrt{(x_0 - x_1)^2 + (y_0 - y_1)^2}$$

First, do the circles intersect? If the distance between the spots is greater than the sum of the radii, the program will return zero for the intersection area:

$$d > r_0 + r_1$$

return: intersection area = 0 px

The second pre-test looks for one circle being in the other circle; in this case, the program will return the area of the smaller circle:

$$d < |r_0 - r_1|$$

Area $C_0 = \pi * r_0^2$; *Area* $C_1 = \pi * r_1^2$

return: intersection area = A_{small}

The third pre-test checks for identical circles. If this is found true, the area of the first circle is given as a result:

$$d = 0 \;\; \& \;\; r_0 = r_1$$

return: intersection area = $\pi * r_0^2$

If the spot pair does not belong to one pre-test group, it will be analyzed with the following computation based on a published calculation[214]. For the calculation of the circle-circle intersection area following variables were defined. In this example (Figure 5), r_1 corresponds to the detection diameter of a podosome divided by two, respectively r_0 corresponds to the detection diameter MT+TIP by two. Further, the center coordinates of each spot are given and the distance can be calculated by the Pythagorean Theorem.

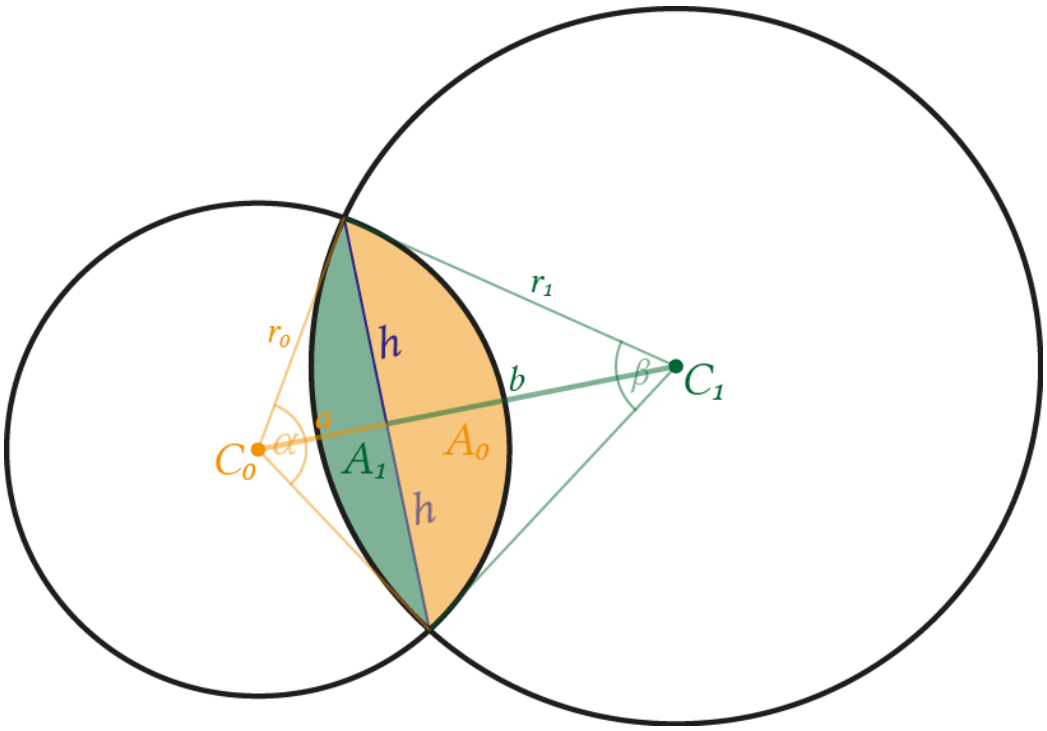

Figure 5: Geometry for intersection calculation

Two segments of a pair of overlapping circles are used to calculate the intersection area[214]

Known variables:

Coordinates (x_1,y_1) of C_1 (center of podosome detection circle)

Coordinates (x_0,y_0) of C_0 (center of MT+TIP detection circle)

r_1 = detection diameter podosome/2

r_0 = detection diameter MT+TIP/2

$$d = \sqrt{(x_0 - x_1)^2 + (y_0 - y_1)^2}$$

Calculated variables:

$$a = \frac{{r_0}^2 - {r_1}^2 + d^2}{2d}$$

$$b = d - a$$

$$h = \sqrt{{r_0}^2 - a^2}$$

$$\alpha = \tan^{-1}(h, r_0) * 2 + 2\pi \quad mod\ 2\pi \quad (1)$$

$$\beta = \tan^{-1}(h, r_1) * 2 + 2\pi \quad mod\ 2\pi$$

Final calculation to obtain the intersection area:

$$A_{intersection} = A_0 + A_1$$

$$A_0 = \frac{{r_0}^2}{2} * (\alpha - \sin\alpha)$$

$$A_1 = \frac{{r_1}^2}{2} * (\beta - \sin\beta)$$

[1] *mod* stands for *modulo* and means that this function results repeat every *2π*

5.3.4.4 Calculating consecutive contacts

A contact is consecutive if a spot from a track in frame n also is in contact with the spot in frame n+1 (any number of following contacts in frames without interruption) as defined above. For calculating the intersection between two MT+TIPs spots, the same method is used as described for the intersection area of a podosome and an MT+TIP spot.

5.3.4.4.1 Process

All possible spot pairs are checked for their intersection area to determine raw contacts in subsequent frames as consecutive contacts. The results are added to a matrix, and the highest value for an overlapping area is identified. The spot pair belonging to this value is stored as a consecutive contact, and these spots are removed from the matrix. In subsequent iterations, all further potential consecutive contacts will be identified by overlap until the intersection matrix is empty.

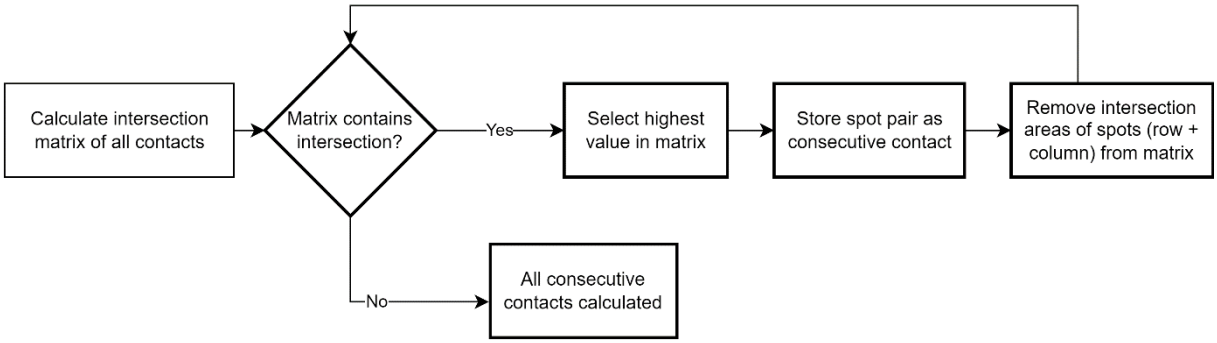

Figure 6: Consecutive contact loop

Flow diagram showing the steps of the program for the decision if raw contacts have to be combined to a consecutive contact.

5.3.4.4.2 Matrix calculation example

An example of three iterations of the here used matrix calculations is provided for better comprehension in Figure 7. We assume a frame n containing four raw contacts (S1-S4) and the subsequent frame n+1 with three raw contacts (S5-S7). The intersection area of all possible combinations between the spots from frame n with those of frame n+1 is calculated as described earlier.

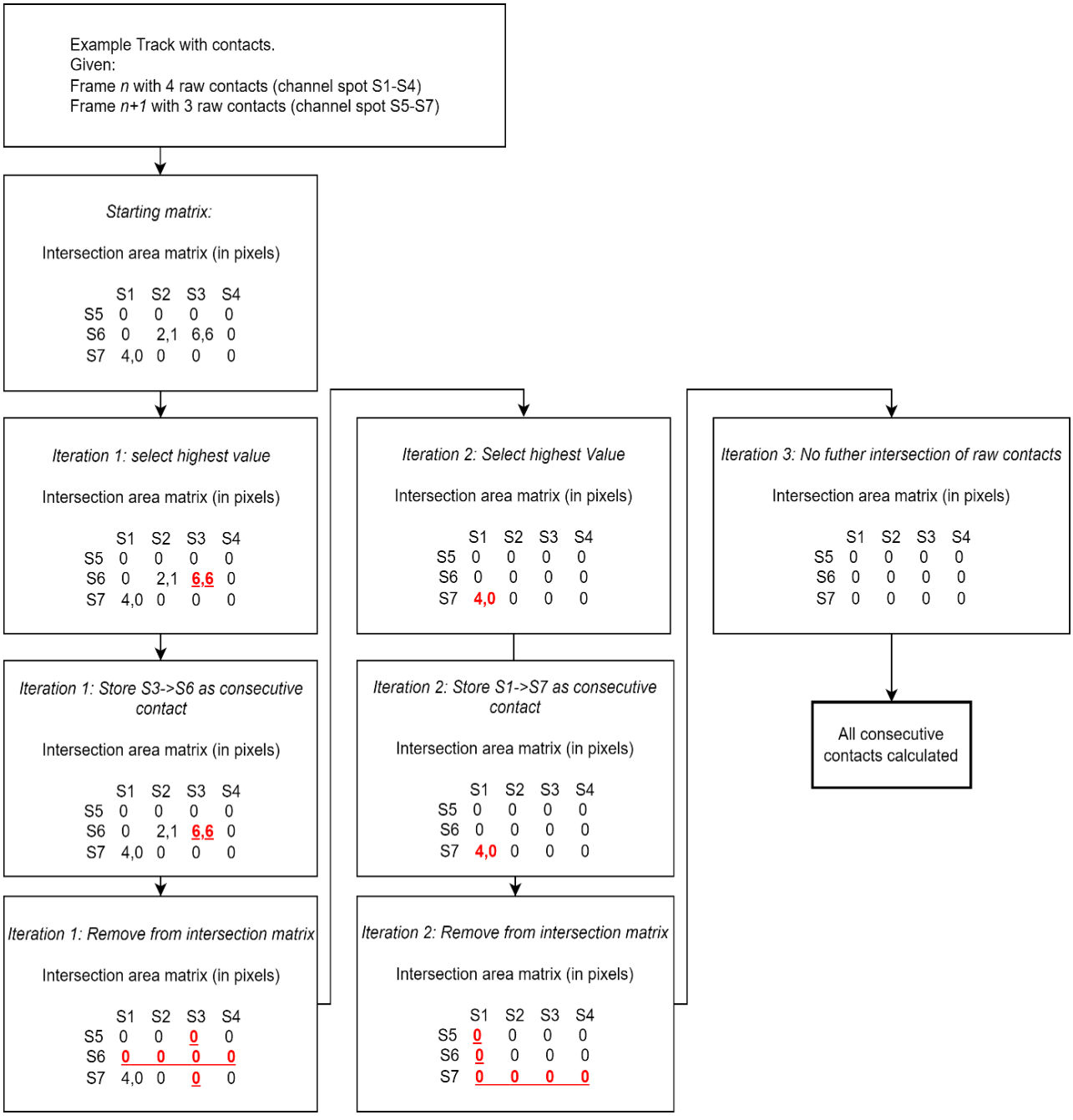

Figure 7 Example matrixes.

Three iterations of program loop with imaginary intersection areas of spots between frame n and frame n+1 od a given example track. Removal of found and stored consecutive contacts until intersection matrix is empty. The possible intersections are processed from the highest to lowest value.

5.3.5 ContactAnalyzer output

The output provided by the ContactAnalyzer for a pair of movies, for example of a podosome reference channel and the respective MT+TIP channel, includes the main file with statistical data for the

- number of podosome tracks,
- the mean podosome track duration (in frames),
- number of MT+TIP spots,
- number of raw contacts,
- number of consecutive contacts,
- mean contact duration (in frames)

Further, this file lists the used parameters like detection diameters, input and output directory path, file matching pattern, minimum track length, and others. Moreover, further files can be created if their parameter is activated. Their contents are summarized below.

ContactDuration file

A “ContactDuration” file will also be created if this parameter is activated. Here for each movie pair, the amount of consecutive contacts for each contact duration is listed separately, as well as the sum and mean number of a certain duration. For example

Cell	1 frame	2 frames	3 frames
cell 1	20	5	2
cell 2	10	9	4
sum	30	14	6
mean	15	7	3

TrackLength file

If the parameter “TrackLength” is activated, a separate file will be generated that lists the number of certain track lengths comparably structured as the list above.

TrackContact file

Another selectable output file called “TrackContacts” can be generated. Here, the mean contact number for a particular track length will be displayed. It is a very detailed list that provides insight into the number of contacts per track, which can be traced back to single frames.

Log file

Further, each run of the program automatically generates a log file, where all the input files, their matching, and the included parameters are documented. In addition, supplementary data like the number of frames, the number of triple or double contacts per spot, and the frequency of certain intersection areas are displayed. Those numbers are helpful for quality control processes.

5.4 MT-podosome contact pipeline

Here, the final established pipeline for contact analysis is shown as an overview. First, the knockdown of the target protein was performed on day ten post-isolation of macrophages. This was followed by overexpression of LifeAct-RFP for podosome visualization and overexpression of +TIP marker for microtubule plus ends, respectively. This was followed by live cell image acquisition after 4.5 hrs incubation.

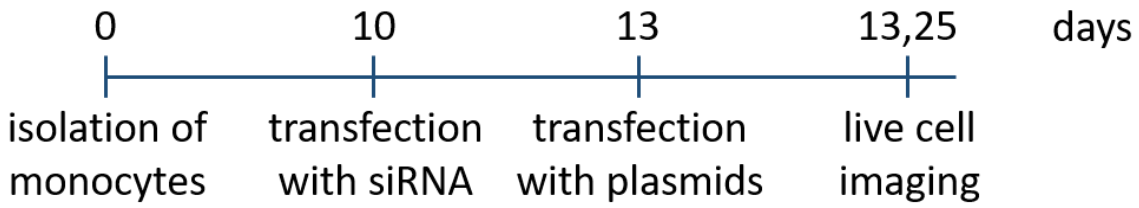

Figure 8: Experimental workflow for contact analysis.
Time course of experimental procedures to gain contact data for different conditions. SiRNA was used to achieve the different knockdown conditions, for visualization of podosomes the LifeAct-RFP plasmid and a MT+TIP marker e.g. EB3-GFP were used.

5.5 Statistics

For the analysis of the subsequently presented graphs, the respective data set was tested for a normal (Gaussian) distribution by plotting the frequency distribution and performing a normal/log-normal Quantile-Quantile-Plot (QQ plot). Most data sets showed a lognormal distribution as commonly observed in biological data. Therefore, comparing more than two conditions, the non-parametric Kruskal-Wallis test followed by Dunn's multiple comparison post hoc test was performed. On the data sets also a natural logarithm transformation was performed with an ordinary one-way ANOVA and a Dunnett's multiple comparison post hoc test. Both led to the same significances. However, only the first variant is presented here because of the decreased readability of non-linear scales of the latter.

6 Results

6.1 Development of podosome MT+TIP contact tool

A detailed analysis of contacts between podosomes and MT+TIPs has not been performed until now, although contact events between microtubules and podosomes, as well as their impact on podosome dynamics, were already observed earlier[62, 215]. Primary human macrophages display numerous (>300) relatively stable podosomes, allowing, on the one hand, to study contacts between MT+TIPs and podosomes in a detailed manner. On the other hand, the large number of podosomes requires automated analysis, especially to prevent the researcher-biased selection of targets.

6.1.1 Stepwise development of a contact analysis

One difficulty in analyzing contacts between two objects, e.g., podosomes and MT+TIPs, is the correct detection of the structures. Especially movies displaying live cell imaging, which is restricted in laser power to ensure cell viability, suffer from a sub-optimal signal-to-noise ratio.

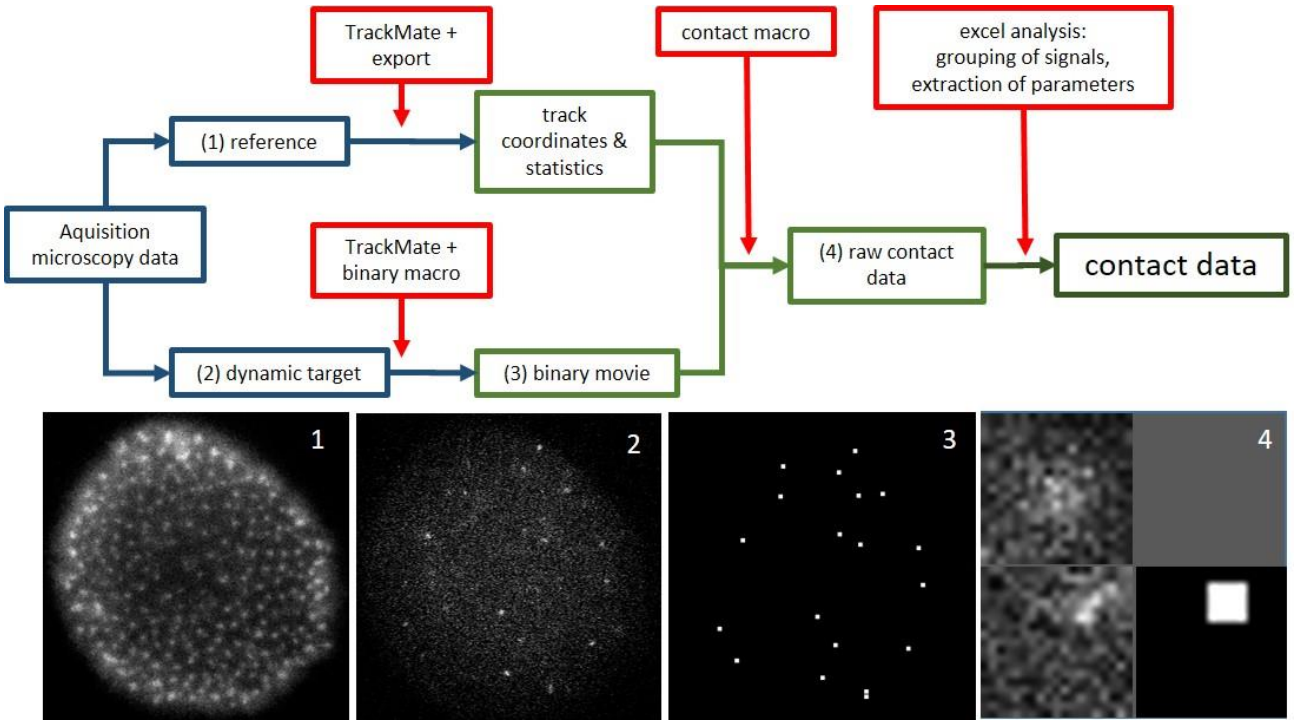

Figure 9: Macro based contact analysis.

Workflow and process of first working contact analysis, based on image analysis after TrackMate. Initially the live cell movies are recorded (1,2). These were then processed with TrackMate to gain track coordinates and a binary movie of the +TIP signals (3). That data subsequently was combined by the contact macro to obtain raw contact data (4). With further analysis in Excel the final contact data was acquired.

The resulting high amount of background signals hampers the target localization. To solve this problem, TrackMate was used, which is an ImageJ plugin that applies a sophisticated algorithm to locate objects based on a blob size and a manually set threshold. Further, this tool can combine the detected objects into tracks. In the first approach, the data from TrackMate (coordinates of spots and track information) were used in an image-based manner for contact detection. Therefore, two macros were generated (Robert Herzog, unpublished). The first one generated binary images with the MT+TIP coordinates for a background-free target signal. The second macro used the track information of the podosomes to extract the respective area in the MT+TIP file.

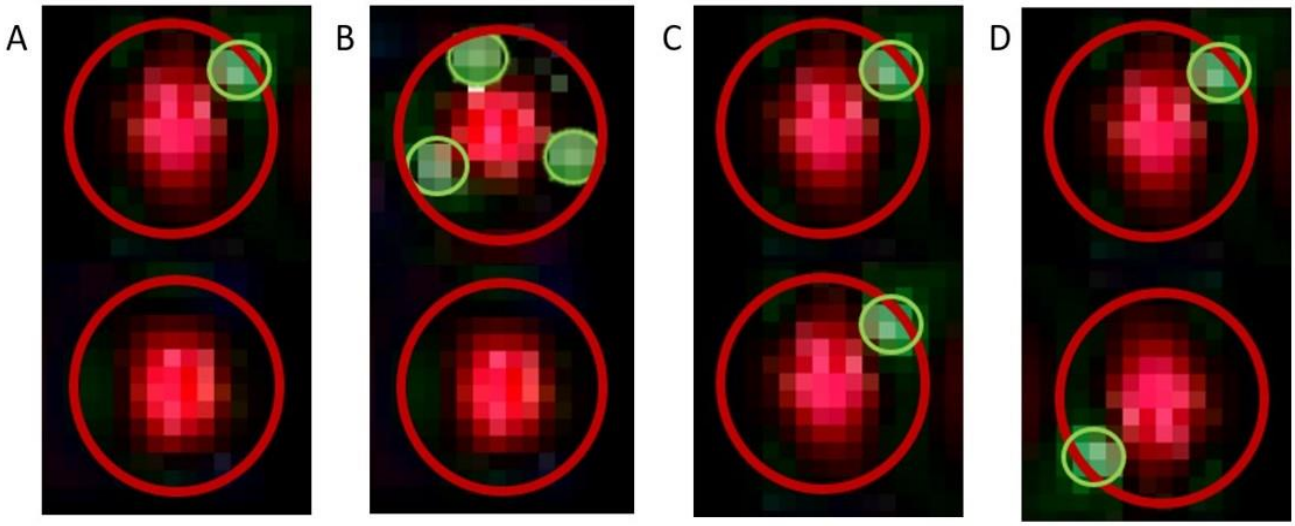

Figure 10: Artificial example contacts.

Artificial example contacts A-D, in the upper row frame n, in the lower row frame n+1 is shown. A depicts a single raw contact, B shows a podosome simultaneously contacted by three MT+TIPs. In C an example for a consecutive contact is shown, where one can assume that the MT+TIP in frame n+1 is the same as above. In D two non-consecutive raw contacts are displayed. In the bottom part the contact readouts of the first image-based analysis (V1) and the “ContactAnalyzer” (V2) are shown. A difference in the resulting output for contact even B and D can be seen.

Unfortunately, an image-based analysis (version 1) leads to a loss of advanced spot information in the process, as it only gives the number of podosomes contacted by microtubules but allows no further information about the amount and position of contacts. For example, one podosome with several simultaneous contacts (Figure 10, B) cannot be distinguished from a single contact (Figure 10, A). Further, the exact localization of a spot is required for the correct combination of raw contacts to consecutive contacts. Because of information loss in the image-based analysis, no difference between contacts of type C and D (Figure 10) could be detected; both would result in a consecutive contact. Additionally, Excel was not suited to perform the needed calculations for the vast number of podosomes and MT+TIPs that arise from the standard data sets of >900 frames per cell. For that reason, an optimized software-based program, “ContactAnalyzer” (version 2), was developed.

6.1.2 ContactAnalyzer

This tool is created for contact analysis from two channels of interest, considering and addressing the pitfalls described in 6.1.1 and Figure 10. While it was initially developed and subsequently used in this Ph.D. project to analyze microtubule +TIPs and podosomes, it is also suitable for detecting similar spot-like structures and is compatible with any form of TrackMate-XML-file.

6.1.2.1 New workflow established

For the analysis of contacts, live cell movies with the Visitron SD-TIRF system were acquired. TIRF (total internal reflection) microscopy was used to reduce the acquired signals to the focal plane of podosomes, which are located at the basal part of macrophages adhering to the glass. Movies were acquired for 30 minutes with a frame rate of 0.5 frames per second. For these live cell movies, different conditions, like overexpression or depletion of specific podosome components, were used.

Using the ImageJ plugin TrackMate[211], XML files were created that contain the coordinates and tracks of podosomes and coordinates of MT+TIPs. The finding of coordinates is based on the LoG detector function of TrackMate, which applies Laplacian of Gaussian filter to the image with a user-defined threshold (sigma) and a blob size that fits the targeted object, i.e., here, 5 pixels for microtubules and 8 pixels for podosomes. TrackMate makes calculations in the Fourier space, and maxima are found in the filtered image. Further, with the help of the LAP tracker, spots of podosomes are combined into tracks in two steps: spots are linked from frame to frame to build track segments. Then, those are combined in a second step according to defined parameters like gap closing. Here applied parameters included a maximal distance of

4 pixels for the frame-to-frame linking and allowed gap-closing of maximal one frame missing and a maximal distance of 4 pixels as well. No track splitting or merging was assumed, and no track filtering inside TrackMate was applied. The calculations and results were saved in XML format.

Those generated XML files were used as input files for the newly developed ContactAnalyzer program to extract and generate statistical data for tracks, spots, and contacts, as explained below (the definition of the parameters and wording can be found in 5.3.2). The resulting output data files (described in more detail in 5.3.5) were further analyzed using Excel and GraphPad Prism.

6.1.2.2 ContactAnalyzer function

The developed program processes at least one reference file (podosome channel) with at least one channel file (MT+TIP channel), further defined as a data pair. This can be done with a single pair (single) or with a whole directory full of files matching a specific name pattern (directory). These commands are followed by a list of parameters, defining which operations and customizations are required for this run of data. For this propose, the acquired live cell movies XML file are read by the ContactAnalyzer. Thereby, information like the number of tracks, their length, and the number of spots can be extracted. The filters and coordinates, as well as the defined parameter of ContactAnalyzer analysis, are applied and all data stay accessible for the program. After a comparison of the reference- and channel files, the ContactAnalyzer calculates the raw contacts. In the second step, these raw contacts are analyzed for being consecutive. In the end, there will be a CSV file provided with the most important statistics and a txt file with the log output, and depending on requested parameters, additional more detailed files. The latter contains information about the number of tracks and spots, the track length of podosomes, the number of raw and consecutive contacts, as well as the contact duration and chosen parameters. The workflow of the program is shown as an overview in Figure 11.

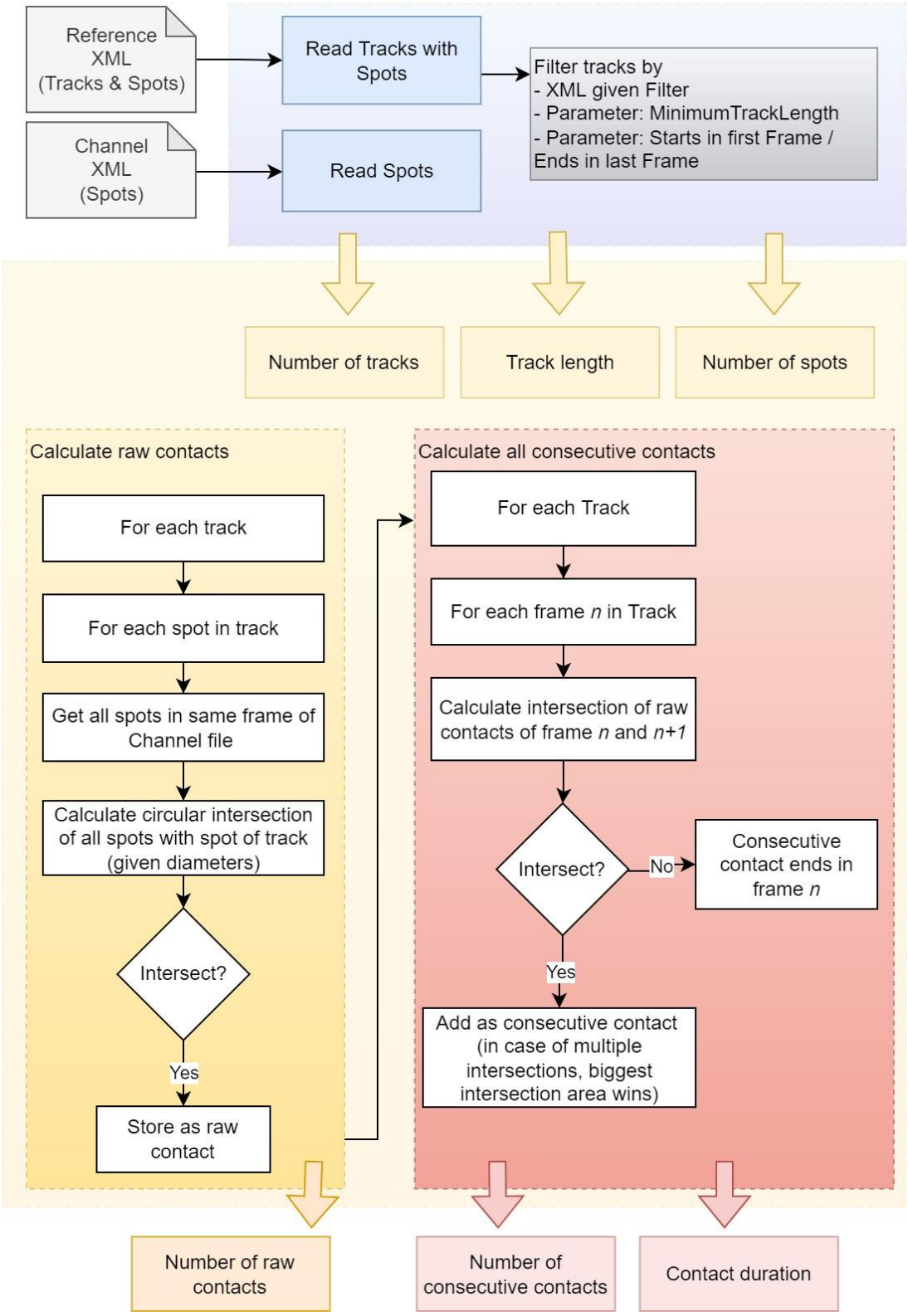

Figure 11: ContactAnalyzer procedure overview

First, the acquired live cell movies XML files as input for the ContactAnalyzer are generated (grey paper symbol). These data files are read (blue box) and the filters, parameters and coordinates get extracted and stay accessible (light yellow background box). From this data pool, the number of tracks, their length and the number of spots can be extracted. All data will be used in the first step to calculate the raw contacts (orange box). In the second step these raw contacts will be analyzed for being consecutive (red box). In the end of the program run, result files will contain the information about the number of tracks and spots, the track length of podosomes, the number of raw and consecutive contacts, as well as the contact duration.

6.1.2.3 Validation/Quality control

For the here-used movies, a diameter of 8 pixels for podosomes and 5 pixels for MT+TIP led to the best TrackMate results and met the average podosome/MT+TIP size. These parameters depend on the movie resolution and must be adjusted for differently acquired data. Detailed analysis of example movies showed that in present movies of particular resolution used for this work, the contact detection diameter of 12 pixels for podosomes based on the average podosome diameter of 8 pixels should reduce the amount of false or not recognized contacts.

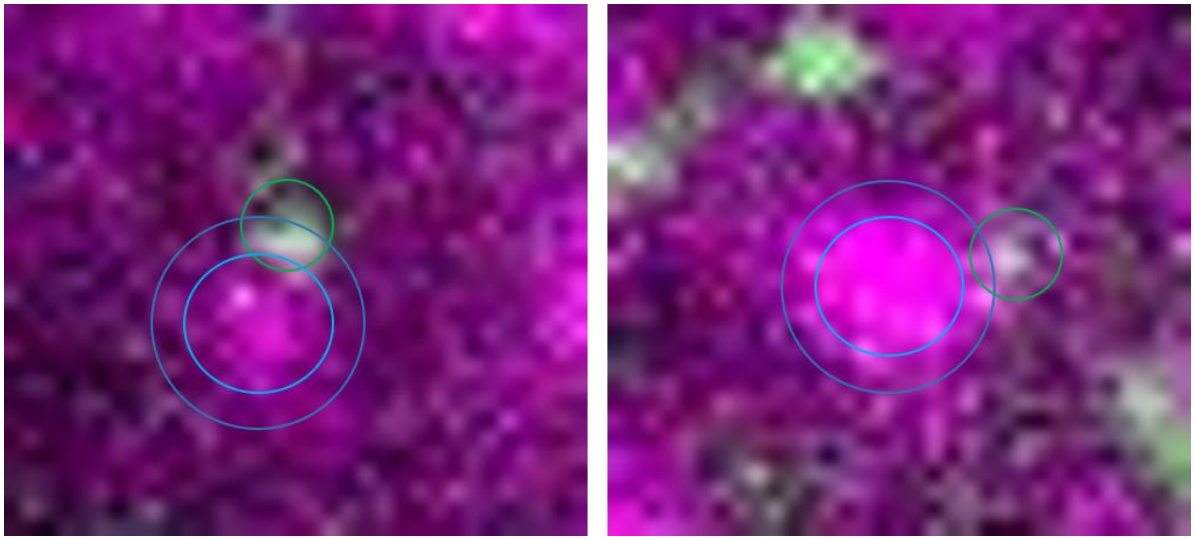

Figure 12: Examples for detection parameters for small and big podosomes.
In this graphic, zoom-ins of spinning disk TIRF images are shown, with LifeAct-RFP in magenta visualizing podosomes and EB3-GFP in green for the MT+TIPs. The light blue circle depicts the 8 pixels blob size for podosome detection, the green circles the 5 pixel blob size for MT+TIP detection. The dark blue circle shows the 12 pixels “DetectionDiameter” set in ContactAnalyzer for contact detection. If only the podosome blob size of 8 pixels was taken for contact assessment, the contact on the right for the bigger podosome would be missed.

6.2 Impact of different podosome components on other podosome & cell characteristics

Initially, a decision on which podosome-associated proteins should be targeted and assessed for their impact (of their depletion) on the general podosome characteristics was needed.

6.2.1 Different target selection and preparation

Most selected targets were already published as podosome components or even with their localization with respect to the podosome core. Nevertheless, a further podosome cap protein could be identified during this work: Drebrin.

6.2.1.1 Drebrin - new podosome cap characterization

For nearer characterization of the drebrin localization in primary human macrophages, podosomes of wild type cells and cells with expression of a drebrin-GFP construct were

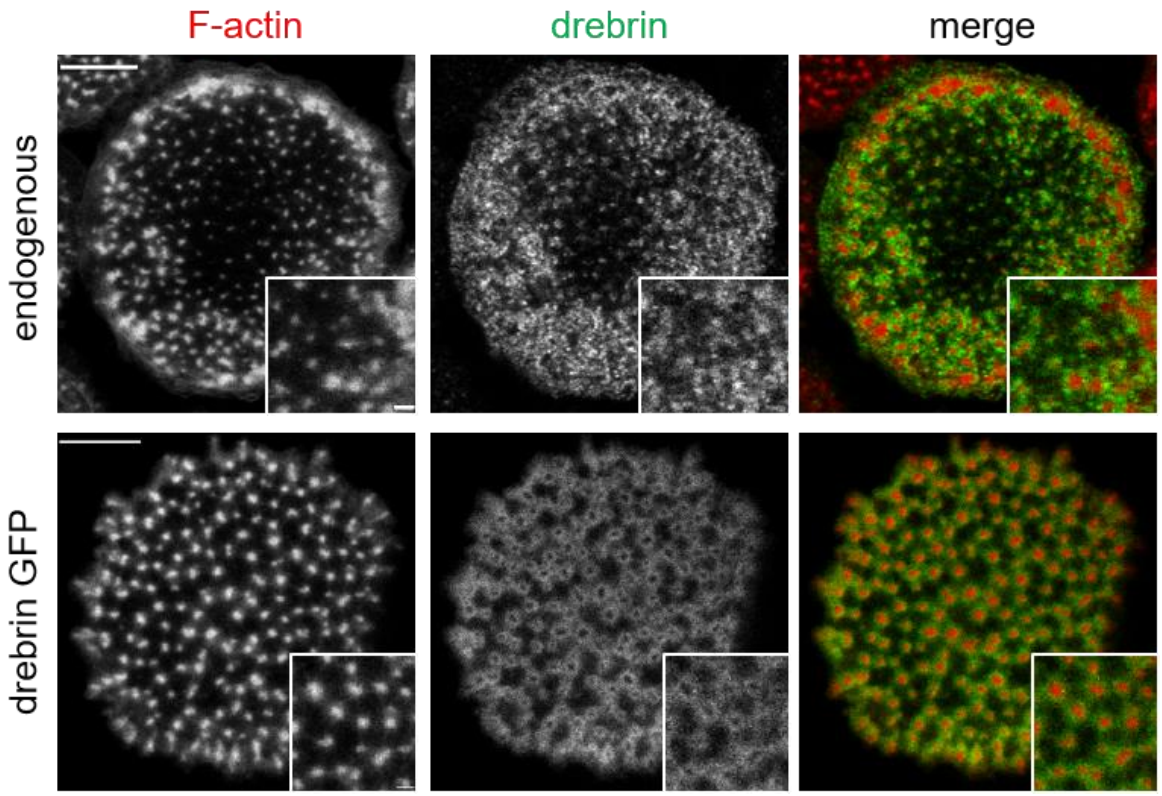

Figure 13: Endogenous and GFP drebrin localize to podosomes.
With an antibody against drebrin the localization of endogenous drebrin (upper row, green) in close proximity to podosomes (red, F-actin labelled by Alexa568 conjugated phalloidin) was found. This distribution was visible as well for the drebrin-GFP construct (lower row, green). Scale bar 7µm, in the inset 1 µm.

observed by confocal microscopy in the course of this work. At the ventral plane, when the podosome core signal is most intense, visualized with phalloidin staining for F-actin, the endogenous drebrin signal appeared as a ring-like protein (Figure 13, upper row). Further, it was shown that the drebrin-GFP construct recapitulates the podosome localization of the endogenous protein (Figure 13, lower row). Interestingly, the endogenous drebrin staining revealed that the expression level might vary between cells. Whereas some cells showed a bright antibody staining against drebrin, others appeared rather dim.

For better visualization of drebrin localization, stacks were acquired, i.e., several planes for the same field of view were imaged. In the subsequent 3D rendering of the confocal microscopy image stack, the signal of drebrin envelopes the F-actin signal in the upper part (Figure 14). Hence, drebrin seems to form a cap-like assembly like α-actinin.

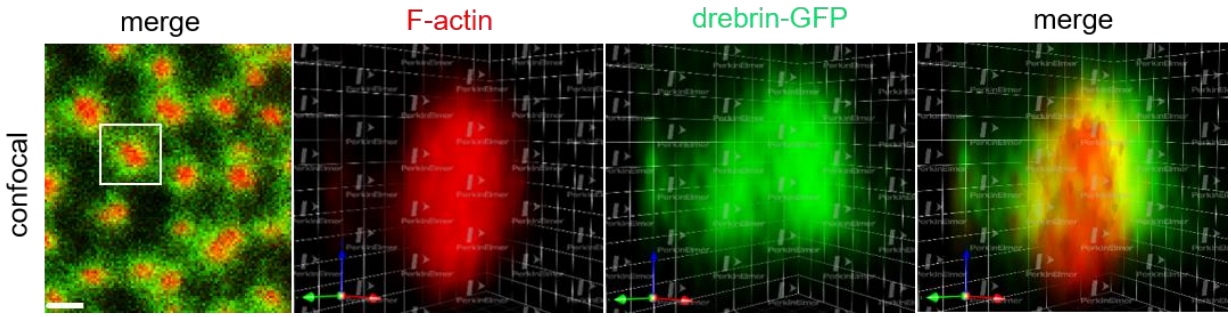

Figure 14: Confocal image of F-actin and drebrin and zoom with 3D rendering.
Podosomes were visualized by F-actin staining with Alexa568-conjugated phalloidin (red). Drebrin-GFP (green) was overexpressed. The area of the white box was used for a 3D display, showing a cap-like intensity for drebrin.

In addition to the general recruitment to podosomes, with the help of the ImageJ-based macro Poji[210], the detailed localization of drebrin respective to the typical core (F-actin), cap (α-actinin), and ring (vinculin) proteins was analyzed. In the lowest and middle layers (Figure 15, plane -2 and plane 0), the intensity of the drebrin signal is lightly increased in the edge region of the podosome but much less than the signal of vinculin. In the top layer (Figure 14, plane +4), the intensity increases from the edge to the middle of the podosome, comparable to the signal of α-actinin. Hence, drebrin shows a cap-like profile. Further, drebrin seems to be more expansive in comparison to α-actinin since in the upper two layers (plane 0 and plane +4), the intensity of drebrin is higher at the rims than that of α-actinin.

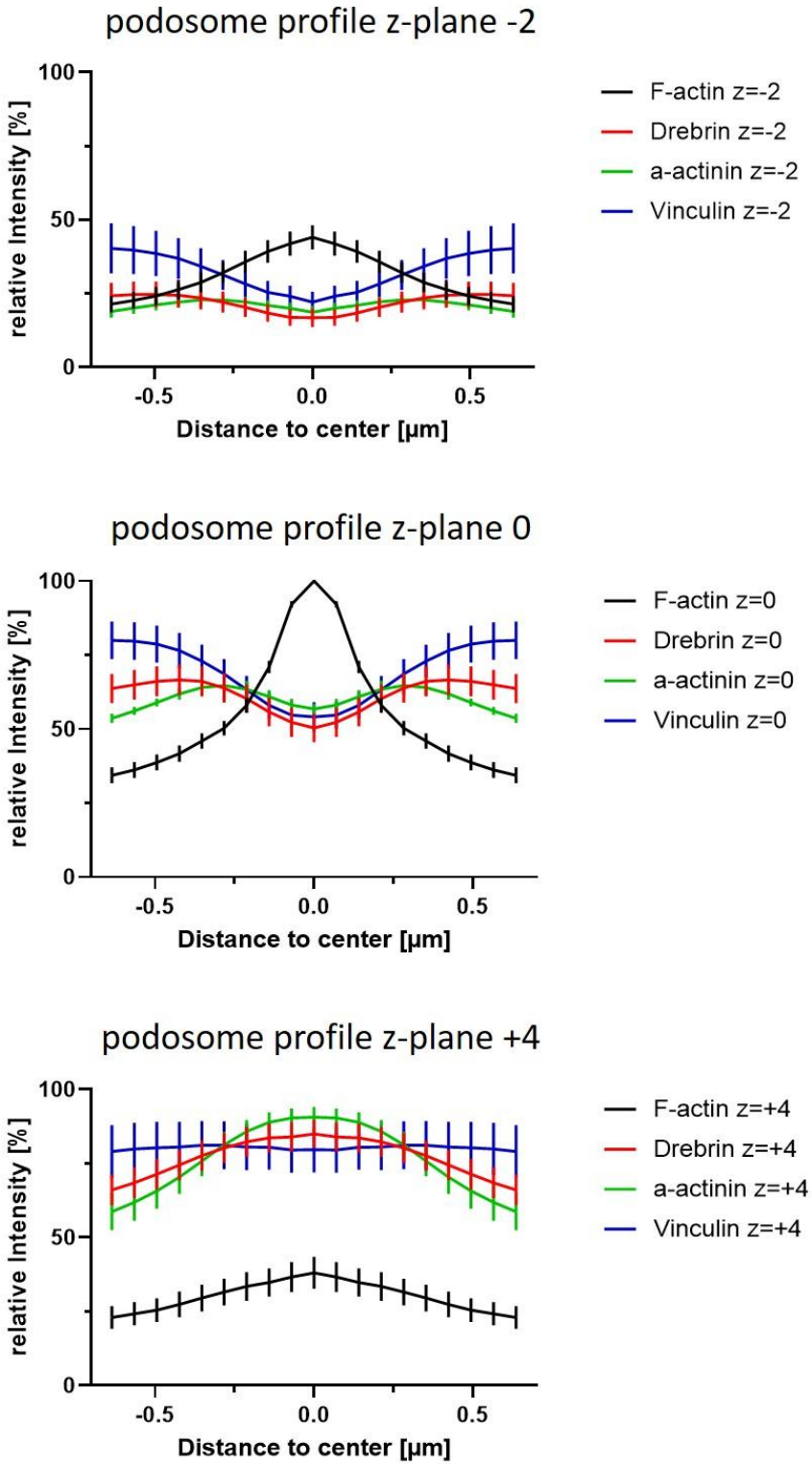

Figure 15: Drebrin profile analysis with Poji.

The intensity of drebrin (red) in three z-planes respective to typical proteins of the core (F-actin, black), cap (α-actinin, green) and ring (vinculin, blue) is shown. The first graph displays the ventral plane, the second graph is at a z-plane with the highest actin intensity and the third graph depicts the profile measurement at the top of the core. Whereas the profile of drebrin (red) shows a ring-like intensity like vinculin (blue) in the central z-plane, it shows a core-like peak in the upper plane (3rd graph), displaying a comparable profile to α-actinin (green).

6.2.1.2 Knockdown verification

For the knockdown conditions in this thesis, already published siRNA sequences for the different targets were used (used siRNA listed in Table 11). Nevertheless, these were tested for efficiency and repeatedly controlled to ensure the quality of the respective results. The efficiency for the knockdown of target proteins with specific siRNA was at least 55 %, resulting in the remaining expression between 0.2-45 %. In case of higher levels of remaining proteins, these samples were not used for further experiments. Figure 16 shows typical Western Blot results for the respective target proteins and their calculated remaining expression levels.

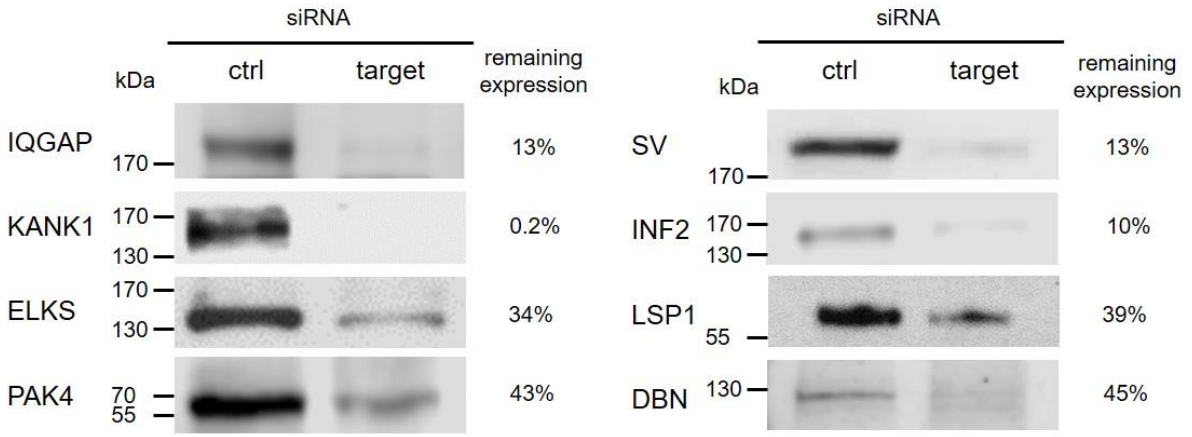

Figure 16: Representative Western blots of different targets.

Displayed are representative Western blot results of the used knockdown conditions. The remaining protein expression ranged from a very efficient knockdown with 0.2% (KANK1) to the least efficient knockdown condition with 45% (DBN). kDa: kilo Dalton; ctrl: control condition; target: condition with knockdown of target protein.

6.2.2 Cell characteristics of knockdown conditions

In the beginning, the different basic cell characteristics were analyzed to assess the potential effects of the knockdown of several targets. Therefore, a minimum of 8 cells per condition, up to 52 cells for the control condition, were analyzed.

6.2.2.1 Cell size and podosome number

The most apparent impact of cytoskeleton-regulation proteins is the one on the size of cells. By using the before mentioned Poji macro[210], the cell area in µm² after depletion of respective proteins in comparison to control cells was determined. An already published effect[57] of the INF2 knockdown to reduce the cell size was reproduced at a significant level (p=0.0018). A reduction of the cell size from the control average of 419 µm² to 210 µm² was observed. No significant change in the general cell size was measured for all other cell conditions.

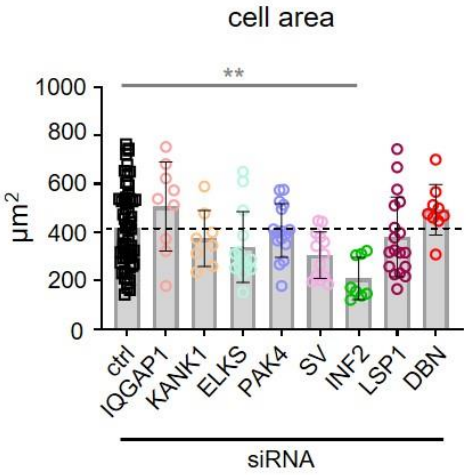

siRNA	Mean	SD	SEM	p-value
ctrl	419	165	22	
INF2	210	88	31	0.0018
IQGAP1	506	184	61	0.5339
KANK1	375	116	41	0.9853
ELKS	339	146	39	0.4197
LSP1	381	164	39	0.9575
SV	305	96	27	0.0942
PAK4	408	111	28	0.9997
Drebrin	493	104	35	0.7233

Figure 17: Cell area analysis and statistics.
Analysis of the cell area showed that the depletion of INF2 leads to significant smaller cells compared to the control condition. There were no other significant differences observed for the cells depleted for the other targeted proteins. In the graph, each bar depicts the mean of the condition with error bars for the SD. Each data point is equivalent to the measurement of a cell. The table on the right side summarizes the mean cell area, SD, SEM and p-value for each condition.

Further, the number of podosomes (Figure 18) was analyzed as a second general and fundamental characteristic of macrophages. Here, a change in the INF2 knockdown condition compared to the control cells could be observed: The number of podosomes was significantly (p=0.0131) reduced to an average of 168 podosomes per cell, compared to 317 podosomes per cell on average for a control cell. All other conditions showed no significantly different numbers of podosomes compared to the control condition.

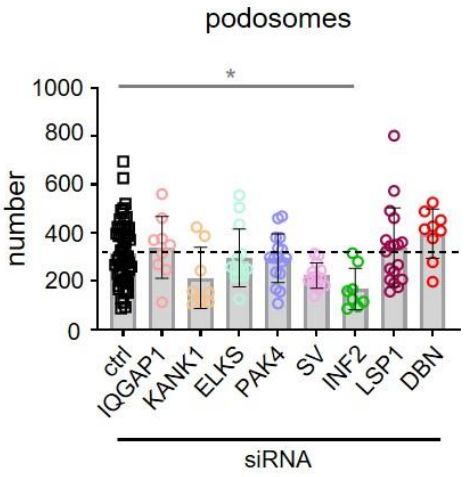

siRNA	*Mean*	*SD*	*SEM*	*p-value*
ctrl	317	131	17	
INF2	168	86	30	0.0131
IQGAP1	340	128	43	0.9977
KANK1	213	127	45	0.1915
ELKS	297	120	32	0.9976
LSP1	340	163	38	0.9925
SV	223	52	15	0.1076
PAK4	296	101	25	0.9971
Drebrin	397	102	34	0.4219

Figure 18: Number of podosomes in one frame and statistics.

Here, the number of podosomes in a still image of cells with different conditions are shown. It could be observed that cells depleted for INF2 have a reduced number of podosomes. Other conditions showed no differences compared to the control cells. In the graph, each bar depicts the mean of the condition with error bars for the SD. Each data point is equivalent to the measurement of a cell. The table on the right side summarizes the mean cell area, SD, SEM and p-value for each condition.

6.2.2.2 Podosome density

The podosome density was analyzed as a quotient of the number of podosomes divided by the cell area since, in the analyzed macrophages, the podosomes were quite evenly distributed.

Even though INF2-depleted cells showed a significantly reduced cell area and number of podosomes, the podosome density is not significantly different from the control cells because both reduction phenomena compensate each other. A significant reduction (p=0.0035) in the podosome density to 0.54 podosomes per µm^2 was observed only in the condition with depleted KANK1 cells, as the podosome number was lightly reduced, whereas the cell area did not change at all (Figure 17, Figure 19). Moreover, the LSP1 knockdown led to a significant increase to 0.9 podosomes per µm^2 (p=0.0322). This was due to a higher number of podosomes in a cell area equal to the wild type cells. In all other conditions, no significant difference from the control was observed.

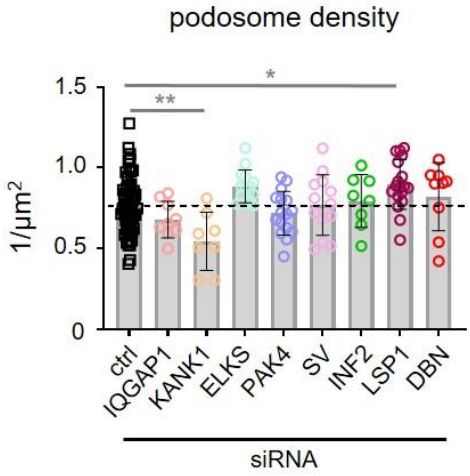

siRNA	Mean	SD	SEM	p-value
ctrl	0.77	0.18	0.02	
INF2	0.79	0.16	0.06	0.9995
IQGAP1	0.68	0.11	0.04	0.6557
KANK1	0.54	0.18	0.06	0.0035
ELKS	0.89	0.10	0.03	0.1276
LSP1	0.90	0.15	0.04	0.0322
SV	0.77	0.19	0.05	>0.9999
PAK4	0.72	0.14	0.03	0.9256
Drebrin	0.82	0.21	0.07	0.9666

Figure 19: Podosome density and statistics.

Podosome density as ration of podosome number and cell area showed significant differences of control condition and KANK1 depleted cells as well as LSP1 depleted cells. KANK1 depleted cells show a reduction in podosome density, whereas it is increased for LSP1 depleted cells. Other analyzed conditions showed no significant difference to the control cells. In the graph, each bar depicts the mean of the condition with error bars for the SD. Each data point is equivalent to the measurement of a cell. The table on the right side summarizes the mean cell area, SD, SEM and p-value for each condition.

6.2.2.3 Podosome size

The size, in this case the diameter of average podosomes, was analyzed to see if the depletion of the target proteins impacts the general podosome structure. Therefore, the mean normalized actin profile was plotted and a Gaussian curve was fitted. Further, the full width at half height (FWHH) was determined mathematically as described for a data sample in Figure 20: Example Gaussian fit.

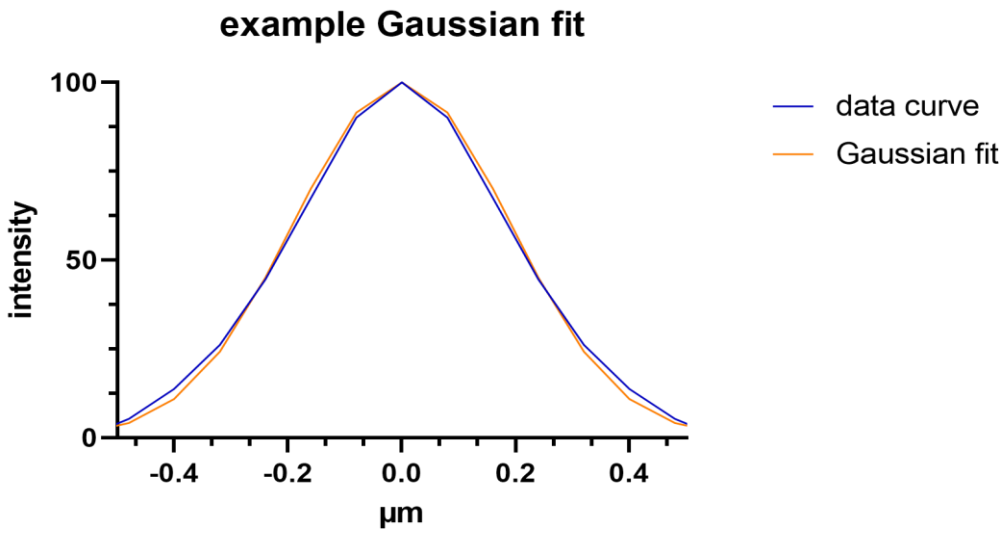

Figure 20: Example Gaussian fit.

To each data curve (blue) a Gaussian fit (orange) was plotted and the FWHH (full width at half height) determined. For the Gaussian fit the function $f(x)=A*e^{-(x-\mu)^2/(2\sigma^2)}$ was used. The FWHH was calculated using $FWHH=2\sqrt{(2*\ln 2)}\sigma$.

The average intensity profile of each condition was normalized to zero – the lowest intensity in the rim of the podosome and 100 for the highest F-actin intensity in the center of the podosome (Figure 21). With light-colored lines, the area of error is marked. For a more detailed view, a zoomed-in graph was plotted in the area of 50 % intensity (Figure 22).

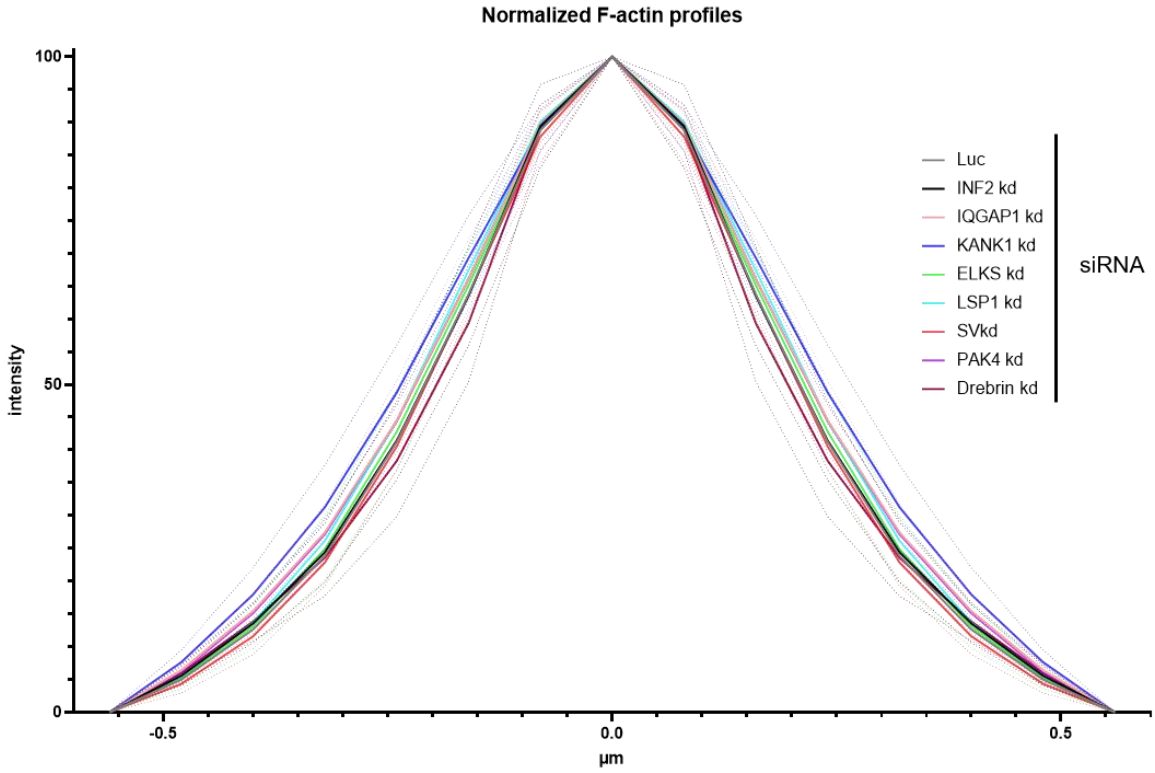

Figure 21: Normalized F-actin profiles.

Here the intensities of mean F-actin profiles of the control condition (grey line) and depleted conditions are plotted. For each data curve an error curve is added with light-coloured lines.

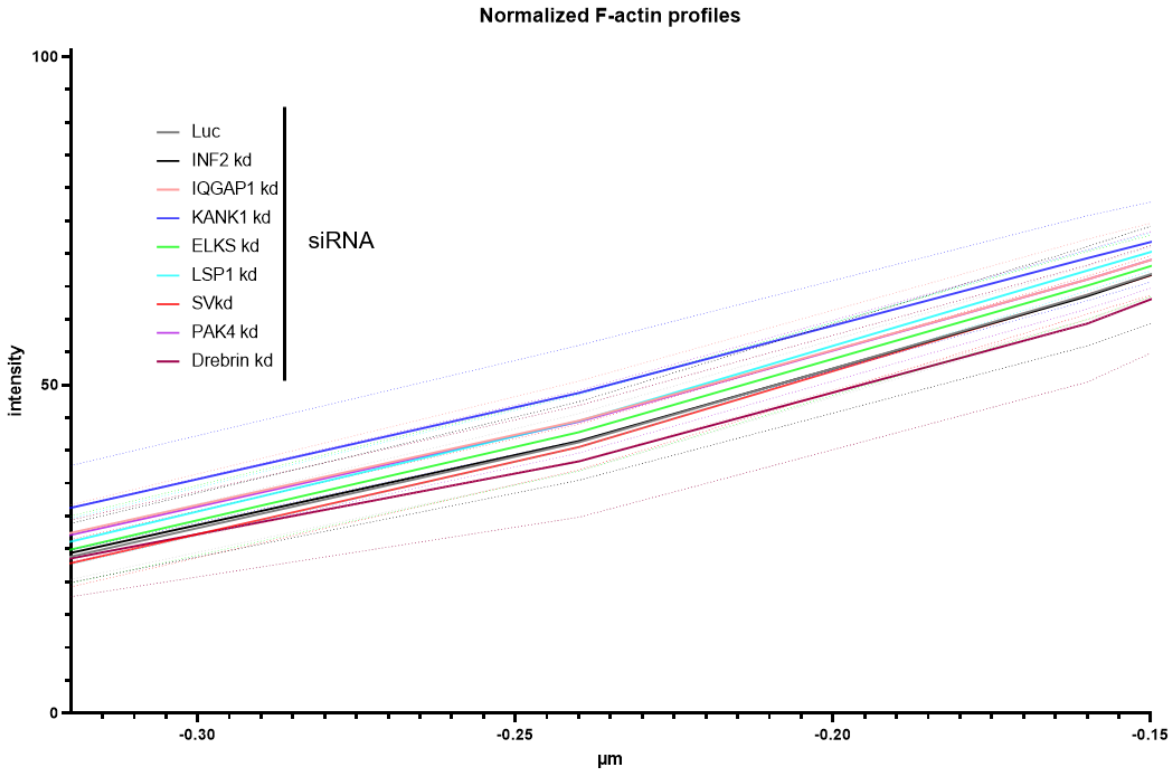

Figure 22: Zoom in normalized F-actin profile graph.

Close up of the area around half intensity for a more detailed impression of curve differences.

Based on the above-described Gaussian fitted curves, the FWHH was calculated.

Table 15: Calculated FWHH for different knockdown conditions, kd: knockdown.

Condition	Full width at half height (FWHH) in µm	% of control
Luc	0.429	
INF2 kd	0.433	101
IQGAP1 kd	0.451	105
KANK1 kd	0.473	110
ELKS kd	0.436	102
LSP1 kd	0.447	104
SV kd	0.422	98
PAK4 kd	0.450	105
drebrin kd	0.421	98

For the average podosome size, no noticeable size differences were observed. Nevertheless, a tendency of an average smaller drebrin or ELKS depleted podosome compared to the control and a tendency of a wider KANK1 depleted podosome was measured.

6.3 Software-based analysis of MT+TIP – podosome contacts

For the analysis of contacts between podosomes and MT+TIPs, not only the software had to be developed, but also the experimental setup had to be established. Therefore, different MT+TIP markers were tested for the visualization of contacts. In the second step, macrophages depleted of different targets were then analyzed with the chosen marker.

6.3.1 MT+TIP marker selection and analysis

First, it was required to assess which +TIP marker is suitable for the contact analysis. The used marker has to be relatively bright with a good signal-to-noise ratio and further to be as close to the front of the +TIP as possible. Another critical trait is that the chosen +TIP marker should interfere with the +TIP function as little as possible. To identify a suitable marker, the potential of CLIP170, EB1, and EB3 as contact markers was assessed. Therefore, podosome and MT+TIP numbers, raw and consecutive contact numbers, as well as the contacts per podosome and the contact duration by overexpression of these markers together with LifeAct-RFP in otherwise untreated macrophages were analyzed. Per condition 9 to 14 experiments were performed.

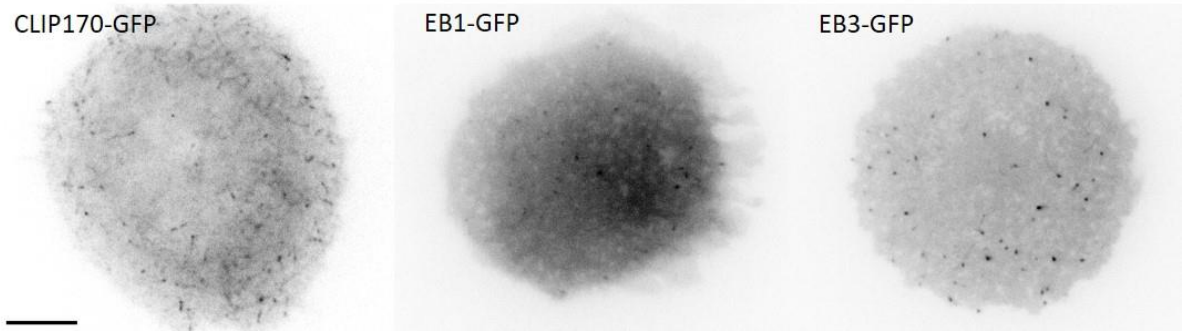

Figure 23: Overexpression of different +TIPs.
Inverted spinning DISK TIRF images of CLIP170-GFP (left), EB1-GFP (center), and EB3-GFP (right). CLIP170-GFP overexpression presents with many +TIPs and an uneven background. EB1-GFP overexpression shows strikingly low numbers of +TIPs and a low signal-to-noise-ratio. EB3-GFP overexpression showed a good signal-to-noise-ratio and less staining of MT lattice compared to CLIP170-GFP overexpression. Scale bar 7µm.

6.3.1.1 Number of podosomes and MT+TIPs

First, the number of podosomes per cell over the course of a 30-minute movie was analyzed. Here no significant differences in the three overexpression conditions with means between 846 and 1006 of podosome numbers (Figure 24) were observed.

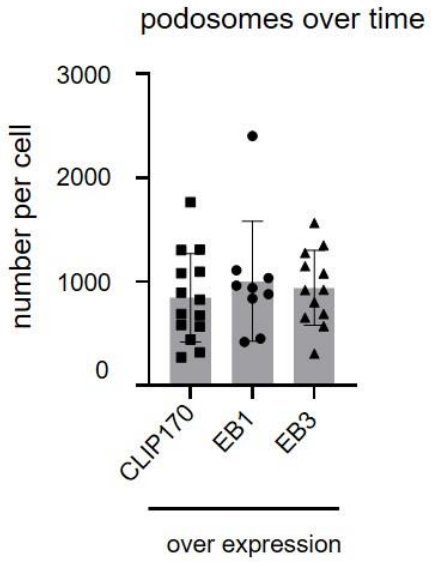

OE	Mean	SD	SEM	p-value
CLIP170	846	426	114	>0.9999
EB1	1006	577	192	>0.9999
EB3	942	361	104	>0.9999

Figure 24: Number of podosomes over time and statistics with different MT+TIP overexpressions. Here is the number of podosomes over time in 30 minutes movies shown. There is no significant difference in podosome number when the +TIPs CLIP170, EB1 or EB3 are over expressed.

Moreover, the amount of MT+TIPs (Figure 25) that were visible in the podosome plane by TIRF was analyzed. The number of +TIPs differs very much between these three overexpression conditions. The highest podosome number was observed for CLIP170, with a mean of 87302 MT+TIPs, and the lowest number with 15728 MT+TIPs for EB1 overexpression. These two conditions differ (highly) significantly, with a p-value of 0.0006. EB3 overexpression leads to a mean number of 57984 +TIPs, being in between those two extremes, with a significance of p=0.0255 compared to EB1 and no significant difference compared to CLIP170 overexpression.

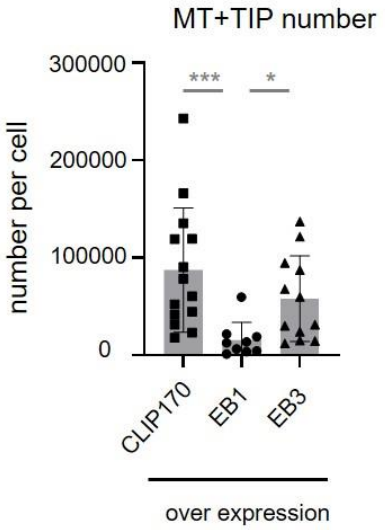

OE	Mean	SD	SEM	p-value	
CLIP170	87302	63771	17044	0.0006	CLIP170 vs. EB1
EB1	15728	17923	5974	0.8551	CLIP170 vs. EB3
EB3	57984	43796	12643	0.0255	EB1 vs. EB3

Figure 25: Number of MT+TIPs detected in the TIRF mode and statistics.
The number of MT+TIPs in a 30 minutes movies is shown. There is a significant difference in MT+TIP number between CLIP170 and EB1 as well as between EB1 and EB3.

6.3.1.2 Number of raw contacts

During analysis of the number of raw contacts, a (highly) significant difference between the condition overexpressing CLIP170 with a mean of 46692 raw contacts and the condition overexpressing EB1 with a mean of 13008 raw contacts, differing with a p-value of 0.0027, was observed. On the other hand, cells with overexpression of EB3 showed a medium number of raw contacts averaging 26337, with no significant difference to both CLIP170 and EB1 cells (Figure 26).

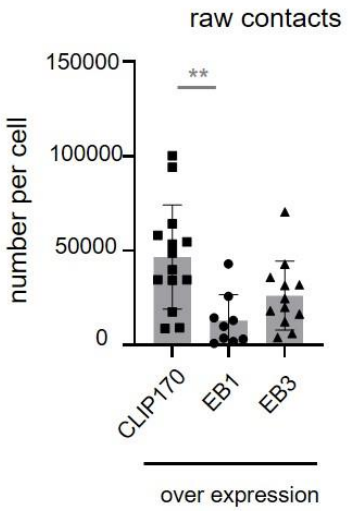

OE	Mean	SD	SEM	p-value	
CLIP170	46692	27511	7353	0.0027	CLIP170 vs. EB1
EB1	13008	13786	4595	0.2205	CLIP170 vs. EB3
EB3	26337	18256	5270	0.3138	EB1 vs. EB3

Figure 26: Number of raw contacts and statistics.
In the analysis of raw contacts was a significant difference in raw contacts between cells with CLIP170 and EB1 overexpression observed. No significant difference in raw contacts between cells with EB1 and EB3 or EB3 and CLIP170 overexpression was measured.

6.3.1.3 Number of consecutive contacts

Further, the interest arose if the number of consecutive contacts and the number of contacts per podosome is altered when different +TIP markers are overexpressed (Figure 27, Figure 28). A high amount of contacts was observed with a mean of 26962 +TIPs when CLIP170 was

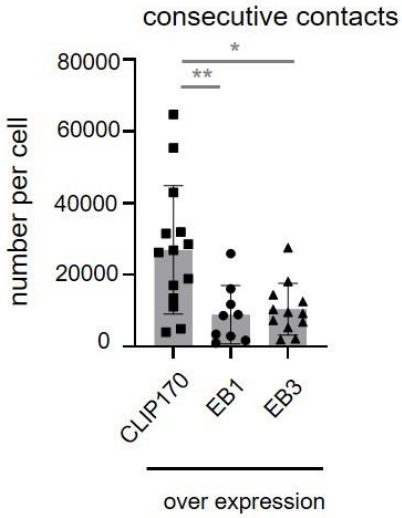

OE	Mean	SD	SEM	p-value	
CLIP170	26962	17844	4769	0.0070	CLIP170 vs. EB1
EB1	8927	8134	2711	0.0293	CLIP170 vs. EB3
EB3	10441	7181	2073	>0.9999	EB1 vs. EB3

Figure 27: Number of consecutive contacts and statistics.
In the analysis of consecutive contacts was a significant difference in consecutive contacts between cells with CLIP170 and EB1 as well as with EB3 overexpression observed. No significant difference in consecutive contacts between cells with EB1 and EB3 over expression was measured.

overexpressed (Figure 27). It was significantly higher than measured for EB1 with 8927 +TIPs (p=0.0070), and also compared to that of EB3 overexpression (10441 +TIPs, p=0.0293) there was a significant increase.

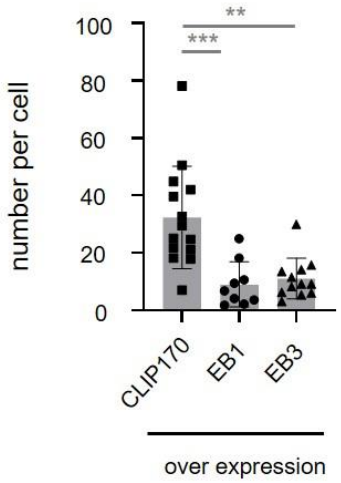

OE	Mean	SD	SEM	p-value	
CLIP170	32	18	5	0.0010	CLIP170 vs. EB1
EB1	9	8	3	0.0027	CLIP170 vs. EB3
EB3	11	7	2	>0.9999	EB1 vs. EB3

Figure 28: Number of consecutive contacts per podosome and statistics.
In the analysis of consecutive contacts per podosome was a significant difference between cells with CLIP170 and EB1 as well as with EB3 overexpression observed. No significant difference in consecutive contacts per podosome between cells with EB1 and EB3 over expression was measured.

Similar differences were measured for those contacts when normalized to the number of podosomes, i.e., consecutive contacts per podosome (Figure 28). Here also, the highest numbers were found in cells with CLIP170 overexpression with 32 contacts/podosome, significantly more than EB1 with 9 contacts/podosome (p=0.0010) and EB3 with 11 contacts per podosome (p=0.0027). No significant difference was observed between the EB1 and EB3 overexpression conditions.

6.3.1.4 Contact duration

The following parameter assessed was the contact duration (Figure 29). Here it was observed that EB1 again showed the lowest values of the three +TIP markers, with a mean contact duration of 2.6 seconds being significantly lower than for CLIP170 with 3.72 seconds (p=0.0292) and also lower compared to EB3 with 5.16 seconds as mean contact duration (p=0.0001). Further, for CLIP170 overexpression compared to EB3 overexpression, a significant difference with p = 0.0353 was observed.

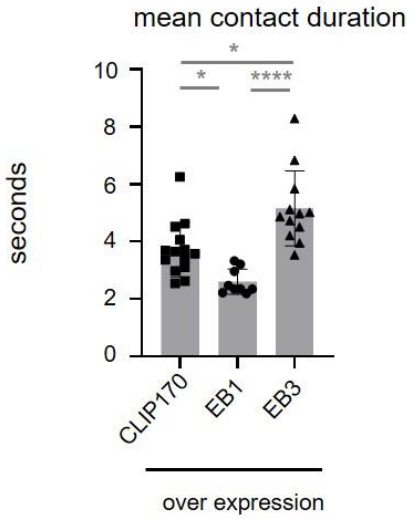

OE	Mean	SD	SEM	p-value	
CLIP170	3.72	0.95	0.25	0.0292	CLIP170 vs. EB1
EB1	2.60	0.44	0.15	0.0353	CLIP170 vs. EB3
EB3	5.16	1.31	0.38	<0.0001	EB1 vs. EB3

Figure 29: Mean contact duration and statistics.
For the mean contact duration, significant differences between all conditions were observed. EB3 overexpressing cells display the highest contact duration, followed by CLIP170 and then with EB1 showing the lowest contact duration.

6.3.2 Impact of different podosome components on contacts

To gain insights about podosome components influencing the contacts, macrophages were depleted of several components. These targets were found or known to be either cap (LSP1, supervillin, INF2, drebrin), ring (PAK4), or associated (IQGAP, ELKS, KANK1) proteins of podosomes. All following measurements were performed by overexpression of the +TIP marker EB3 and for podosome visualization LifeAct-RFP and knockdown of the respective target. As before, 30-minutes TIRF movies with a frame rate of one frame per two seconds were used for the analysis. Per condition, a minimum of 8 cells was analyzed, up to 52 cells for the control condition.

6.3.2.1 Number of podosomes and MT+TIPs

The detection of podosomes and MT+TIPs was performed on TIRF data to restrict the analyzed microtubule signals to those occurring within the basal, substrate-attached plane of the cell, where podosomes are located. The detection is mainly based on TrackMate, as described above. For several analyzed knockdown conditions, no significant difference in the number of podosomes was found (Figure 30). However, compared with the control average of 1508 podosomes per cell over the movie time, a tendency for fewer podosomes in cells

depleted of INF2 with a mean of 867 podosomes was observed with a p-value of 0.06, in line with the significant reduction of the podosome number of INF2 depleted cells in section 6.2.2.1.

In the analysis of the MT+TIPs, an increase to 53503 MT+TIPs in the IQGAP knockdown was observed (Figure 31). However, no significant difference in MT+TIP number compared to the control, with a mean of 23021 MT+TIPs, was found in all other knockdown conditions.

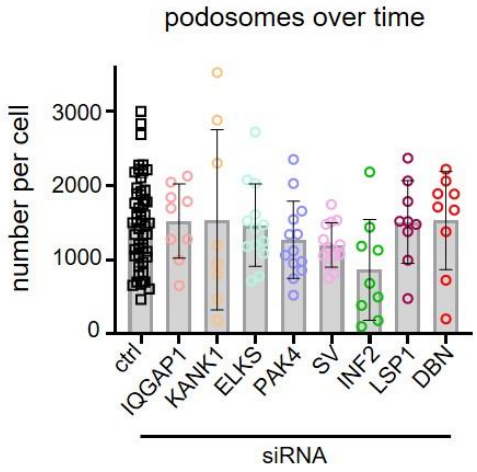

siRNA	Mean	SD	SEM	p-value
ctrl	1508	600	83	
IQGAP1	1525	499	166	>0.9999
KANK1	1540	1215	429	>0.9999
ELKS	1470	553	154	>0.9999
PAK4	1272	519	144	>0.9999
SV	1202	299	83	0.8744
INF2	867	679	226	0.0618
LSP1	1512	556	185	>0.9999
DBN	1531	661	220	>0.9999

Figure 30: Number of podosomes over time in different knockdown conditions and statistics.
No significant difference in the number of podosomes that were tracked during 30 minutes in a cell. A tendency of a decreased amount of podosomes was observed in INF2 depleted cells with a p-value of 0.0618.

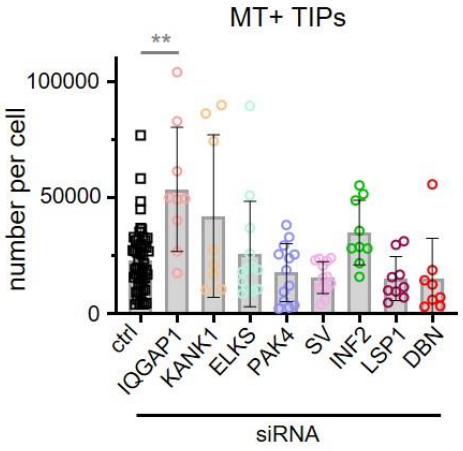

siRNA	Mean	SD	SEM	p-value
ctrl	23021	14139	1961	
IQGAP1	53503	26756	8919	0.0146
KANK1	41982	35112	12414	>0.9999
ELKS	25625	22666	6286	>0.9999
PAK4	17607	12496	3466	>0.9999
SV	15431	6871	1906	0.8619
INF2	34853	13935	4645	0.2949
LSP1	15073	9481	3160	0.9224
DBN	15037	17353	6135	0.3341

Figure 31: Number of MT+TIPs over time in different knockdown conditions and statisics.
A significant difference in the number of MT+TIPs that were tracked during 30 minutes in a cell was found for IQGAP1 depleted cells. All other conditions show comparable amounts of MT+TIPs in the podosomal plane.

6.3.2.2 Number of raw contacts

First, all raw contacts were analyzed. As a raw contact counts each MT+TIP signal in a detection diameter of 12 px of a podosome, using 30 minutes live cell movies. These contacts were calculated using ContactAnalyzer as described in 5.3.4.3 “Calculation of raw contacts”. A significantly reduced number of raw contacts in drebrin-depleted cells was observed, with a mean of 883 raw contacts, compared to an average of 5530 raw contacts in the control condition (Figure 32). Also, a relatively small standard deviation can be seen in these cells. In contrast to drebrin-depleted cells, the conditions with INF2 andIQGAP1 knockdown show tendentially a higher yet not significant mean than control cells, whereas KANK1 and ELKS knockdown show tendentially more lower data points than control cells, with all four havening an extensive spread of the measured values of single cells.

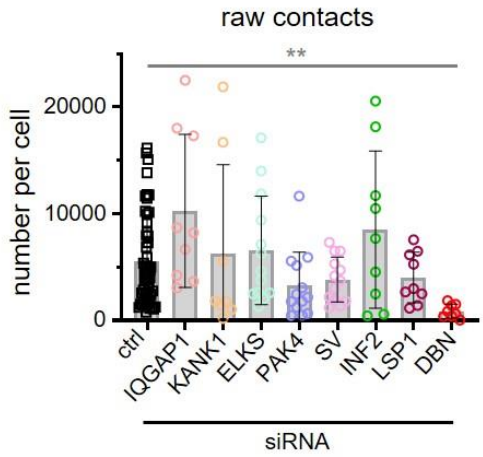

siRNA	*Mean*	*SD*	*SEM*	*p-value*
ctrl	5530	4301	597	
IQGAP1	10264	7166	2389	0.3190
KANK1	6307	8288	2930	>0.9999
ELKS	6568	5085	1410	>0.9999
PAK4	3269	3146	873	0.5431
SV	3830	2113	586	>0.9999
INF2	8521	7362	2454	>0.9999
LSP1	4028	2373	791	>0.9999
DBN	883	643	228	0.0010

Figure 32: Number of raw contacts and statistics.

The number of detected raw contacts of EB3-GFP positive MT+TIPs around LifeAct-RFP positive podosome in a detection diameter of 12 px in a 30 minutes movie is shown. Drebrin depleted cell show a significant ($p = 0.001$) reduced amount of raw contacts (mean DBN 883, mean control 5530), whereas the other conditions do not differ significantly.

6.3.2.3 Number of consecutive contacts

Further, the number of consecutive contacts was analyzed (Figure 33). Consecutive contact means that subsequent raw contacts that are assumedly the same MT+TIP over two or several frames are combined into a single signal. Here a significantly (p=0.0013) reduced number of consecutive contacts in drebrin-depleted cells (mean 760) compared to the control condition (mean 4507) was observed as well. However, the other conditions do not differ significantly from the control.

Further, normalization of these consecutive contacts to the number of podosomes that were present in the respective cells of different conditions was performed. Therefore, the number of contacts per podosome (Figure 34) was analyzed. For example, in drebrin-depleted cells, the number of contacts per podosome was with 0.5 significantly (p-value = 0.0008) lower compared to the control with 3.4 consecutive contacts per podosome. Although cells with a knockdown of INF2 show a wide variability of values, significantly more consecutive contacts per podosome were observed compared to luciferase-treated control cells. Similarly to the contact data before, a wide variability of values can be seen for several conditions like INF2, IQGAP1, KANK1, or ELKS knockdown.

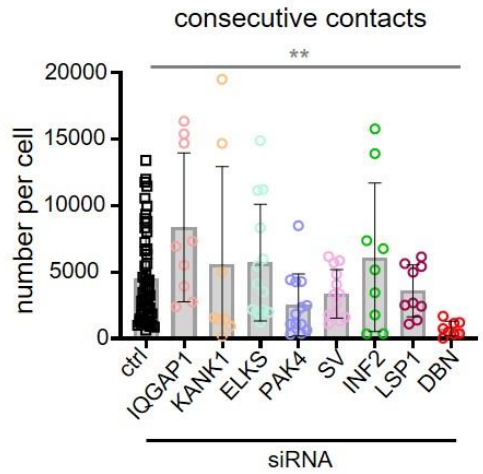

siRNA	Mean	SD	SEM	p-value
ctrl	4507	3492	484	
IQGAP1	8357	5591	1864	0.2806
KANK1	5587	7337	2594	>0.9999
ELKS	5707	4377	1214	>0.9999
PAK4	2523	2321	644	0.3553
SV	3352	1825	506	>0.9999
INF2	6100	5564	1855	>0.9999
LSP1	3588	1943	648	>0.9999
DBN	760	551	195	0.0013

Figure 33: Number of consecutive contacts and statistics.

The number of detected consecutive contacts, i.e. consecutive raw signals are added to a singe consecutive contact, of EB3-GFP positive MT+TIPs around LifeAct-RFP positive podosome in a detection diameter of 12 px in a 30 minutes movie is shown. Drebrin depleted cell show a significant (p = 0.0013) reduced amount of consecutive contacts (mean DBN 760, mean control 4507), whereas the other conditions do not differ significantly.

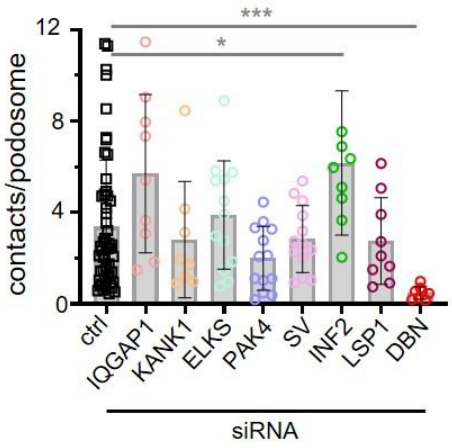

siRNA	*Mean*	*SD*	*SEM*	*p-value*
ctrl	3.4	2.9	0.4	
IQGAP1	5.7	3.5	1.2	0.2609
KANK1	2.8	2.5	0.9	>0.9999
ELKS	3.9	2.4	0.7	>0.9999
PAK4	2.0	1.4	0.4	>0.9999
SV	2.8	1.5	0.4	>0.9999
INF2	6.2	3.2	1.1	0.0458
LSP1	2.8	1.9	0.6	>0.9999
DBN	0.5	0.3	0.1	0.0008

Figure 34: Number of consecutive contacts per podosome and statistics.

The ratio of consecutive contacts per LifeAct-RFP positive podosomes is shown. INF2 depleted cells display an increased contacts per podosome ($p = 0.0458$), drebrin depleted cells show a reduced amount of contacts per podosome ($p = 0.0008$), whereas the other conditions do not differ significantly.

6.3.2.4 Contact duration

To further characterize the contacts between podosomes and MT+TIPs, a detailed analysis of the duration of these contacts was performed (Figure 35). Here cells with INF2 knockdown showed a significantly increased contact duration from 2.5 to 2.8 seconds, whereas cells with a knockdown of LSP1 showed a significantly reduced contact duration of 2.2 seconds compared to the control condition. Drebrin-depleted cells, which showed in the previous characteristics differences, do not differ significantly from the control. This is also valid for IQGAP1, KANK1, ELKS, PAK4, and supervillin.

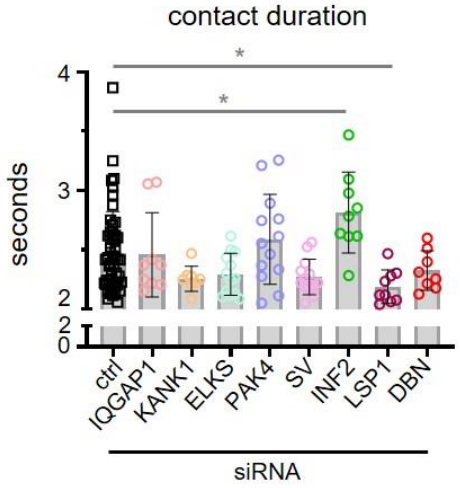

siRNA	Mean	SD	SEM	p-value
ctrl	2.5	0.3	0.0	
IQGAP1	2.5	0.4	0.1	>0.9999
KANK1	2.3	0.1	0.0	0.8355
ELKS	2.3	0.2	0.0	0.8342
PAK4	2.6	0.4	0.1	>0.9999
SV	2.3	0.2	0.0	0.3796
INF2	2.8	0.3	0.1	0.0470
LSP1	2.2	0.1	0.0	0.0359
DBN	2.3	0.2	0.1	>0.9999

Figure 35: Mean contact duration in seconds and statistics.
The mean contact duration in seconds between EB3-GFP positive MT+TIPs around LifeAct-RFP positive podosome in a detection diameter of 12 pixels is shown. INF2 depleted cells display an increased contact duration ($p = 0.0470$), LSP1 depleted cells show a decreased contact duration ($p = 0.0359$), whereas the other conditions do not differ significantly.

In the more differentiated analysis of the contact durations, the frequencies of different contact lengths instead of their means were used (Figure 36). It was observed that in the control (luciferase siRNA treated cells), around 87% of contacts are one frame long (0-2 seconds), 12% of contacts show a duration between 4 and 10 s, and 0.6% of contacts were detected with a duration of 10 to 20 seconds. Compared to the control, INF2-depleted cells show less short (0-2 s; 79 %) and more longer-lived contacts (2-10 s 20 %; 10-20 s 1 % and >20 s 0.13 %). In contrast, LSP1-depleted cells show more shorter-lived (0-2 s; 92 %) and less longer-lived contacts (2-10 s 8 %; 10-20 s 0.16 % and >20 s 0.01 %).

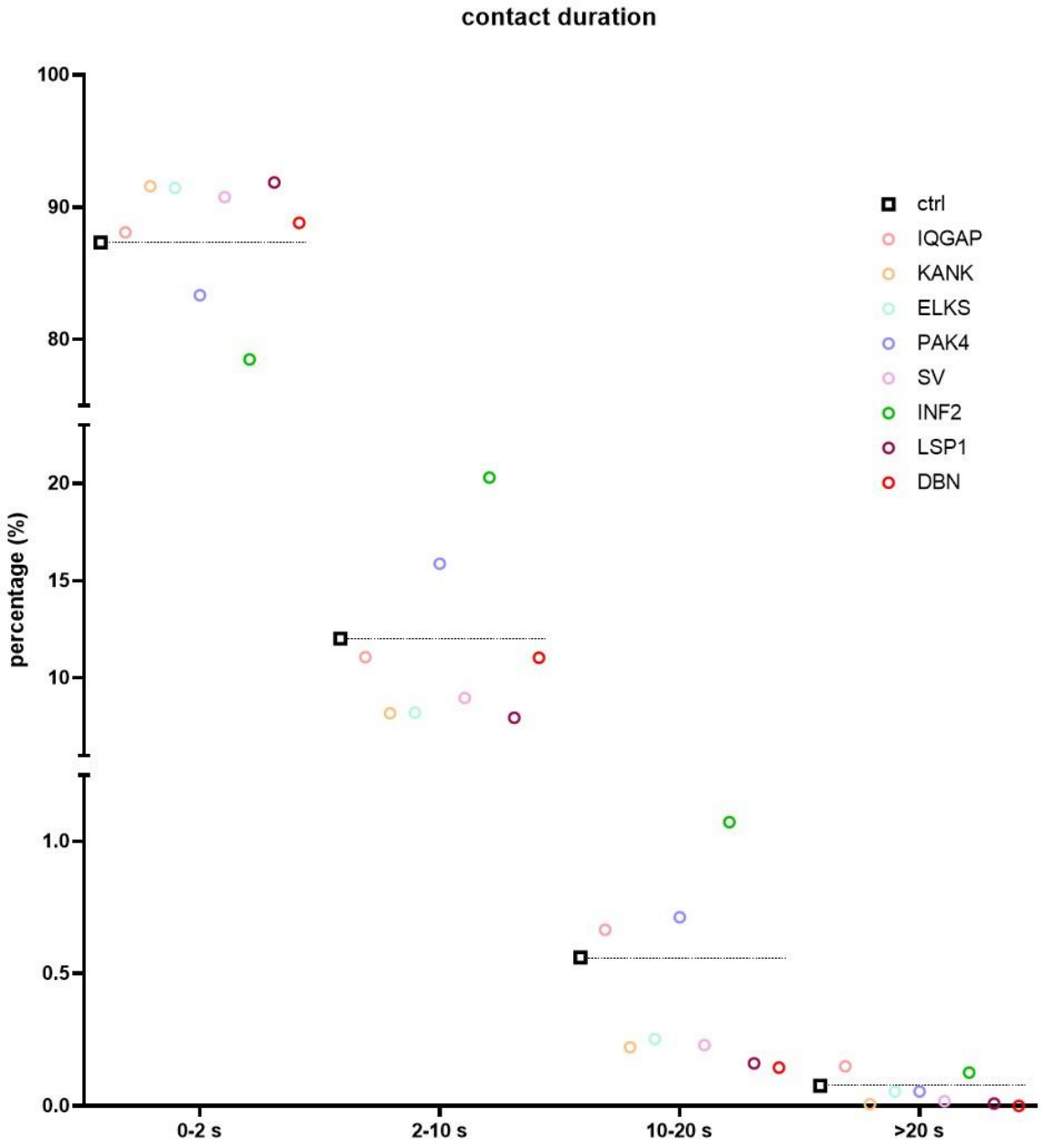

	%			
	0-2 s	2-10 s	10-20 s	>20 s
Luc	87	12	0.56	0.08
IQGAP	88	11	0.67	0.15
KANK	92	8	0.22	0.01
ELKS	91	8	0.25	0.06
PAK4	83	16	0.71	0.06
SV	91	9	0.23	0.02
INF2	79	20	1.07	0.13
LSP1	92	8	0.16	0.01
DBN	89	11	0.15	0.00

Figure 36: Detailed contact duration and grouped values.

The detailed analysis of contact duration shows the amount of contacts of a certain duration per cell as percentage (%).

6.4 Functional consequences of altered podosome composition & contact behavior

To assess the changes in podosome function upon depletion of different targets, podosome dynamics, i.e., the lifetime, was analyzed. Further, the ability of treated macrophages to degrade rhodamine-labeled gelatin as a read-out of microtubule-based vesicular trafficking was assessed. In addition, the amount of the cell surface-associated pool of MT1-MMP was measured.

6.4.1 Podosome dynamics

The podosome lifetime was studied to analyze the potential impact of the depletion of the proteins and/or the altered contact behavior on the podosome dynamics.

The podosome lifetime was measured by analysis of the track length of podosome tracks in 30-minute TIRF movies (Figure 37). The mean podosome lifetime is reduced in cells depleted for KANK1 compared to the control condition. Since a tendency for a reduced lifetime in INF2 knockdown and a potentially increased lifetime in LSP1 knockdown was observed, the podosome lifetime was analyzed more thoroughly, i.e., the frequency for each lifespan is potted instead of the mean (Figure 38). Here it could be observed that especially in the INF2 or KANK1 depleted cells, there are no long-living podosomes present as the lifetime was no longer than 18 minutes (for KANK1 KD) or 24 minutes (for INF2 KD) in comparison to the more than 30 minutes for all other conditions.

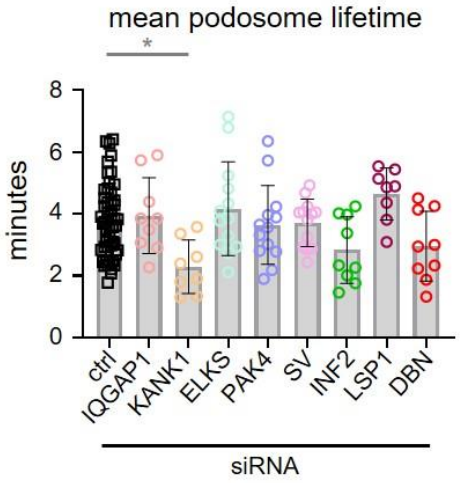

siRNA	Mean	SD	SEM	p-value
ctrl	3.80	1.19	0.17	
IQGAP1	3.95	1.23	0.41	>0.9999
KANK1	2.29	0.86	0.30	0.0117
ELKS	4.17	1.51	0.42	>0.9999
PAK4	3.65	1.27	0.35	>0.9999
SV	3.71	0.76	0.21	>0.9999
INF2	2.83	1.08	0.36	0.3023
LSP1	4.65	0.84	0.30	0.3333
DBN	2.96	1.13	0.38	0.7338

Figure 37: Mean podosome lifetime and statistics.

The mean of all LifeAct-RFP positive podosomes within one cell is shown. KANK1 depleted cells display a decreased podosome lifetime ($p = 0.0117$), whereas the other conditions do not differ significantly.

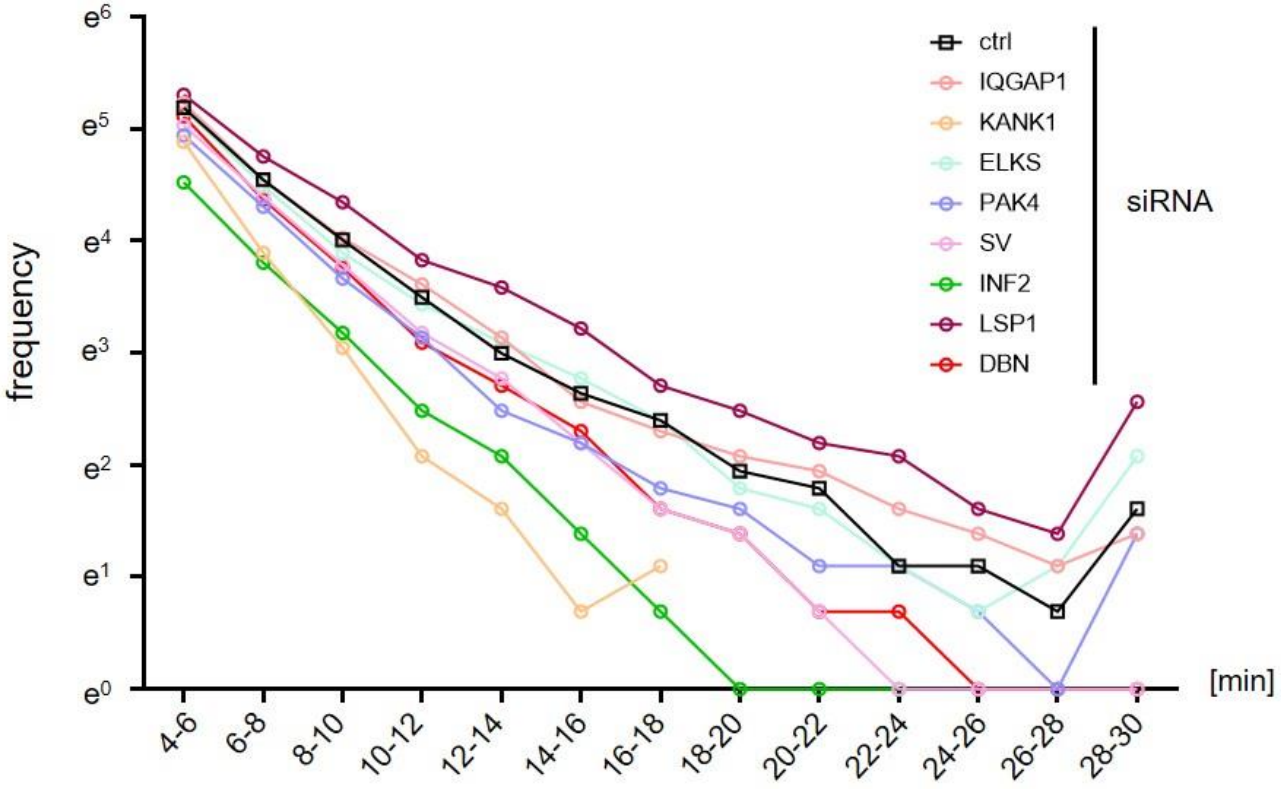

siRNA	Mean [min]	SD	SEM	p-value	
ctrl	8,50	51	14		
IQGAP1	8,60	53	15	>0.9999	ns
KANK1	6,48	37	10	<0.0001	****
ELKS	8,66	50	14	>0.9999	ns
PAK4	8,21	40	11	0.1450	ns
SV	7,67	45	12	0.0374	*
INF2	7,28	27	7	<0.0001	****
LSP1	9,39	58	16	0.3596	ns
DBN	7,66	47	13	0.0520	ns

Figure 38: Detailed podosome lifetime and statistics.

It is the detailed frequency distribution shown for different lifetimes of tracked podosomes on a non-linear scale (natural logarithm). No graph means there were no podosomes of this lifetime duration (zero cannot be plotted in a natural log scale). The graph for KANK1 knockdown, INF2 knockdown and SV knockdown differ significantly of that from the control.

6.4.2 Podosome architecture/structure

For more detailed insights, the podosomes in the knockdown conditions for their size, the profile behavior of the typical podosome components, and other characteristics as described in the following part. For this detailed analysis, it was chosen to focus on the conditions that showed already alterations in the previous analysis and are potentially crucial for the subsequent recruitment of proteins to podosome structures (i.e., drebrin, INF2, and KANK1 knockdown). Further, a knockdown of EB3 was also analyzed to assess the impact of the chosen +TIP marker.

The analysis of the detailed podosome architecture was based on the ImageJ macro Poji[210]. For drebrin-, EB3-, INF2- and KANK1-depleted cells, the staining and intensity measurement of three main components were performed: F-actin for the core, α-actinin for the cap and vinculin for the ring of podosomes. The images were acquired as stacks, i.e., imaging different focal planes, and plane z=0 was chosen for the analysis. This plane was defined by the most intense phalloidin signal for F-actin. The core, cap, and ring staining intensity were measured for two values, the whole cell (Figure 39, A, C, E) and the combined podosome intensity (CPA). The latter includes only the podosome area and excludes the cortex and the area between podosomes (Figure 39, B, D, F).

The measurement showed that none of the knockdowns affected the whole cell F-actin level. However, the loss of INF2 and KANK1 increased the F-actin portion in podosomes. In the case of the α–actinin staining, a decrease was measured in the whole cell for the INF2 knockdown, whereas the other conditions had unchanged levels. Interestingly, the recruitment of the cap intensity was not decreased by INF2 depletion. Nevertheless, an increase in the α–actinin intensity in the combined podosome area was measured for the drebrin knockdown. Lastly, the vinculin intensity was assessed. Whereas a decrease in the vinculin staining for the whole cell was observed for EB3-, INF2- and KANK1-depleted cells, a decreased vinculin intensity at podosomes was measured only for INF2 and KANK1 siRNA-treated cells.

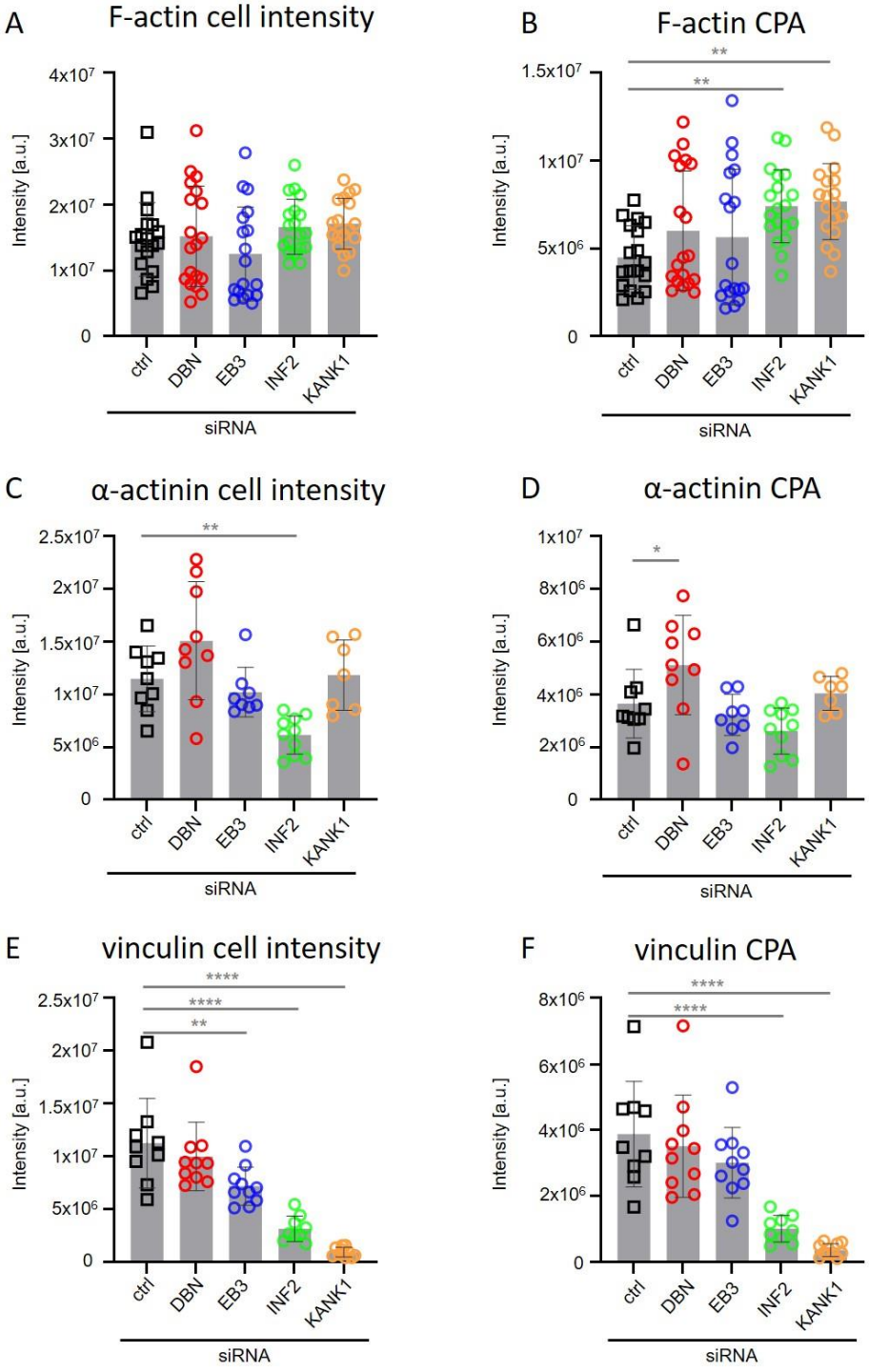

Figure 39: Core, ring and cap staining intensities.

Analysis of core, ring and cap with Poji for the whole cell and combined podosome area (CPA) in plane z=0. For the analysis of the core (A,B) F-actin staining by phalloidin was used, for the cap (C,D) endogenous staining of α-actinin and for the ring (E,F) staining of vinculin was performed. z=0 was defined by the most intense F-actin plane. A) The F-actin staining showed no differences for the condition in the whole cell. B) F-actin measurement restricted to the podosome are showed increased intensity for INF2- and KANK1-depleted cells. C) Whereas a decrease of α-actinin staining for INF2 knockdown was observed in the whole cell, D) and increase for the cap staining in the CPA of drebrin-depleted cells was measured. E) Although a decreased vinculin intensity was measured in the cells depleted of EB3, INF2 or KANK1, F) at podosomes a decrease was observed only for INF2 or KANK1 siRNA treated cells.

6.4.3 Degradation capability

To further analyze the functional consequences of altered podosome-MT+TIP contact behavior and/or the effect of depleted podosome proteins, the capability of the different conditions to degrade rhodamine-labeled gelatin was assessed. Therefore, macrophages were seeded on coverslips that were coated with rhodamine-labeled gelatin. Representative cells for the analyzed conditions are shown in (Figure 40). For each condition, a minimum of 12 field-of-views were taken, and the intensity of the remaining rhodamine-gelatin under the cells was measured (Figure 41). A significant increase in the degradation capability was observed in cells depleted of drebrin or EB3 with p-values of 0.0007 and 0.0059, respectively. The simultaneous knockdown of drebrin and EB3 did not lead to a significant difference compared to the control condition. For the knockdown of INF2 or KANK1, a significant decrease in the degradative activity was measured, with p-values of 0.0001 and 0.0036, respectively.

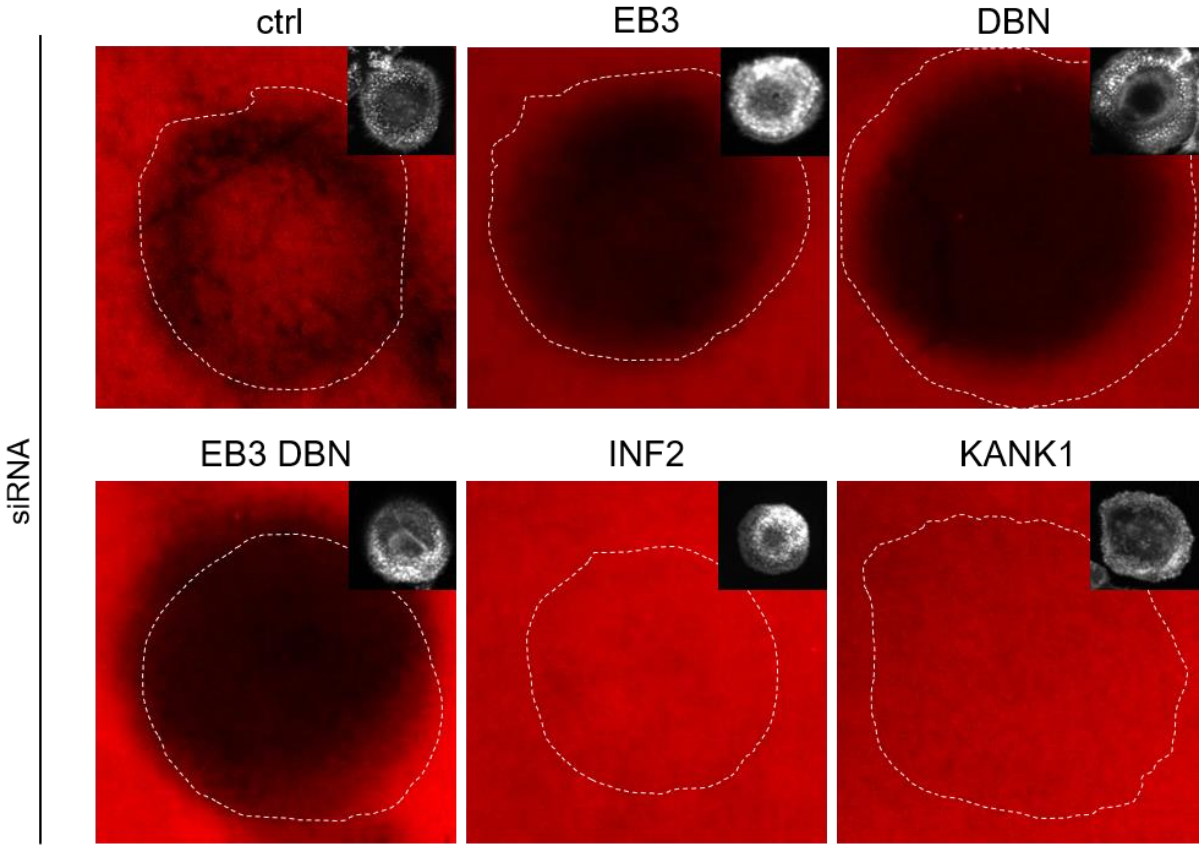

Figure 40: Representative images of rhodamine-gelatin degradation with knockdown cells.
For cells depleted of EB3, drebrin or both a stronger degradation of rhodamine-gelatin compared to the control cells was observed. In contrast depletion of INF2 or KANK1 leads to a near total loss of rhodamine-gelatin degradation. The inset shows an F-actin staining with phalloidin of the respective cell.

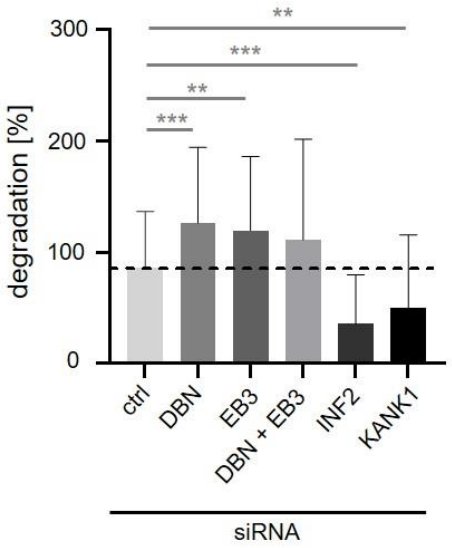

siRNA	Mean	SD	SEM	p-value
ctrl	91	9	1	
double	89	9	1	0.0717
DBN	87	12	1	0.0007
EB3	87	11	1	0.0059
INF2	96	7	1	0.0001
KANK1	96	7	1	0.0036

Figure 41: Degradation capability of different knockdown conditions and statistics.
Here is shown that in comparison to the control condition the depletion of EB3 or drebrin leads to a significant increase in gelatin degradation. The simultaneous depletion of both proteins does not enhance the effect. The depletion of INF2 or KANK1 reduces the observed degradation capability significantly.

6.4.4 MT1-MMP surface levels

To find possible reasons for the increased degradation capability of macrophages that were depleted of EB3 or drebrin, and decreased degradation capability of INF2- or KANK1 knockdown cells, the amount of MT1-MMP at the cell surface was assessed. Therefore, living primary human macrophages were detached and stained with a primary conjugated antibody, and one sample was stained with an isotype control antibody for background subtraction. Since no permeabilization is performed, only the MT1-MMP that is surface exposed is stained by the antibody and then detected by FACS measurement. To reduce endocytosis events, cells were kept permanently on ice after staining. Per condition, 3 x 10^4 cells were acquired.

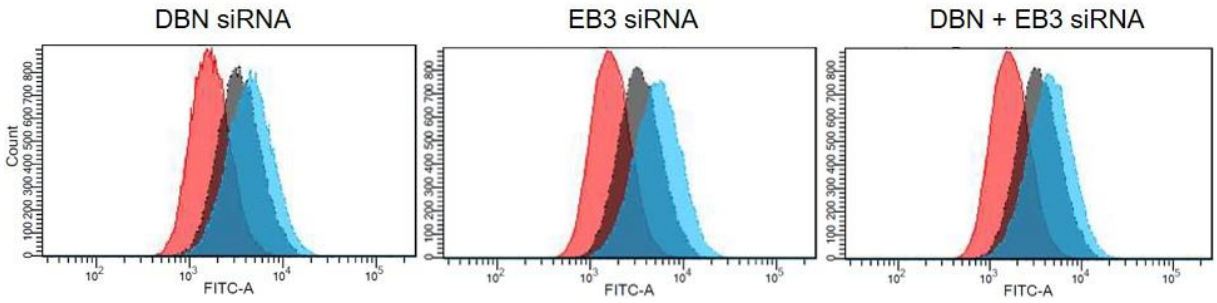

Figure 42: Histogram of drebrin and/or EB3 knockdown condition.

FACS Histograms of drebrin, EB3 and double knockdown condition is shown. The red curve is the isotype control that is used to subtract background. In grey the control condition, treated with a non-targeting siRNA, is shown. The blue curve corresponds to the respective knockdown condition. For all three siRNA treatments a right-shift of the curve can be observed, equating a higher measured staining intensity.

A significantly increased MT1-MMP surface level for EB3 and also for drebrin knockdown cells was found. The double knockdown did not lead to an increase further than that of one siRNA treatment alone. For INF2 and KANK1 knockdown conditions, a slight increase in the amount of surface MT1-MMP was observed (Figure 43).

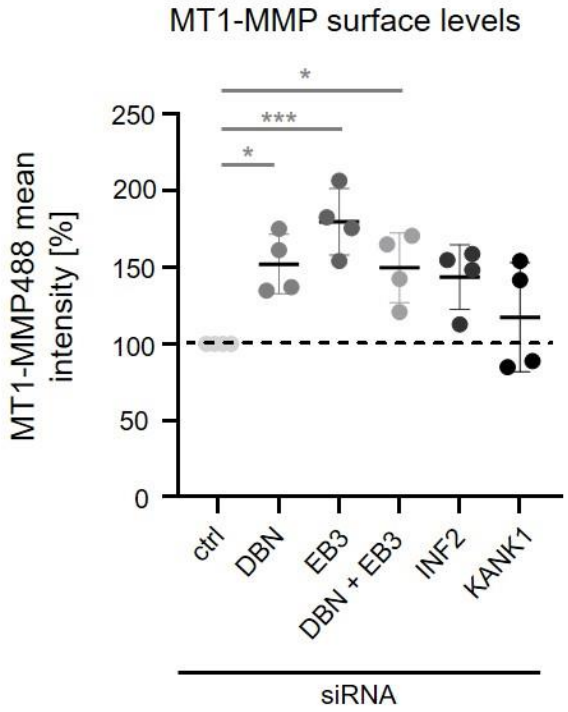

Figure 43: FACS results for MT1-MMP surface levels.

MT1-MMP surface levels were stained with a primary conjugated antibody against MT1-MMP in different knockdown conditions and subsequently measured by FACS. Per data point 3 x 10^4 cells were acquired.

7 Discussion

The focus of this work was the stepwise development of the software-based program "ContactAnalyzer" and its successful application for the investigation and quantification of intracellular contacts between podosomes and microtubule plus ends.

Development of ContactAnalyzer

Since the discovery of podosomes in the 1980s by David-Pfeuty and Marchisio[26, 216], they have been the subject of research in different cell systems and research questions. After the first characterization of the main components, scientists became more interested in a detailed analysis of their structure and regulation. Recently, Poji[210], a macro-based podosome analysis tool, was published by our lab to enable the detailed and more objective structural analysis of many podosomes. This tool will help to answer many questions about the localization of specific components relative to the actin core of the podosome. The more is known about the podosome, the more interest arises in the regulation and interaction with other cell structures and the functional consequences.

It is becoming increasingly clear that the actin and the microtubule network are intertwined at multiple levels, thus, affecting and regulating each other. For example, microtubule ends probe the actin-rich cellular cortex influencing the F-actin structures[147, 148], and on the other hand, the microtubule catastrophe rate is influenced by the branched F-actin network density[149, 150]. Moreover, podosomes were observed to be contacted by microtubules, thereby altering podosome dynamics[62]. Further, the site-directed tethering of microtubules to podosomes is required to deliver cargo like MT1-MMP or soluble MMPs[69, 82, 83, 140]. Therefore, gaining more insights into the contact behavior of podosomes and microtubule plus ends, as well as potential functional consequences resulting from those contacts an important field for further research.

However, most interaction and contact analyses were performed between microtubules and focal adhesions. Often contacts are not measured directly, but focal adhesion disassembly is used as a read-out after nocodazole (an MT depolymerizing agent) washout[217]. Nevertheless, contacts were also counted in a limited number of fixed cells, for example, with double staining of vinculin and tubulin[218]. Although the live cell analyses of contacts were carefully performed, for example, including controls like “dummy contacts”[219], the nature of the manual analyses made the assessment of high numbers of events unlikely. Therefore, often only a few cells were analyzed over a short period of time (1-4 minutes), and manually around 20 microtubules per condition were followed [220]. Further, these contact analyses were performed mainly in goldfish fibroblasts with relatively spare microtubule arrays and, therefore, not readily transferable to mammalian cells, which typically show dense microtubule networks.

Manual detection is more complicated because podosomes are more dynamic and numerous than focal adhesions. The average lifespan of focal adhesions is 20 to 90 minutes[221-223], usually with less than 60 FAs in a cell[224, 225]. In comparison, macrophages display around 300 podosomes per cell with a lifetime of 2-20 minutes[38, 60]. Therefore, only a few studies have been published that directly assess the contacts between microtubules and podosomes, and they rely on indirect read-outs. Those read-outs can be podosome number after nocodazole-washout, labeled MT localizing at the ventral side of a cell at substrate patches for podosome contacts[199] or DEM (digital elevation models) of podosome and microtubule showing proximity without quantification[226]. To date (to my knowledge), only three published research articles[62, 215, 227] performed live cell experiments with subsequent direct contact analysis between podosomes and microtubule plus ends. Zhu et al. showed in A7r5 rat smooth muscle cells that usually an EB3-labeled +TIP was present before a podosome forms[227]. Therefore, they analyzed a circle with a 1.5 µm diameter at coordinates of 100 newly formed podosomes on EB3-GFP signal in the previous 12 frames (equivalent to 1 minute). The other two studies were performed in primary human macrophages with CLIP170-GFP as +TIP marker and RFP-LifeAct for podosome visualization, with manual analysis of contacts. Presumably, due to the time-consuming process of manual contact detection, the number of analyzed podosomes was a minimum of 9 per condition[215] in one case, and a total of 731 podosomes[62] in the other.

Since contacts between podosomes and microtubules are challenging to assess in detail, there was a need to develop a tool to analyze statistically significant amounts of podosome-MT+TIP contacts. Therefore, an image-based analysis of live cell movies was started (6.1.1 Stepwise development of a contact analysis) by correlating podosome localization with binary MT+TIP signals. In the first version, a loss of information was encountered due to the image-based analysis. On the one hand, the conversion of the microtubule +TIP channel into binary images and, on the other hand, the binary results of contacts. This means only a yes or no answer if there is an MT+TIP signal in the area of a detected podosome. A coordinate-based analysis with the newly programmed “ContactAnalyzer” was successfully developed and validated to improve data extraction from live cell movies. The development of ContactAnalyzer solved shortcomings of the previous attempts concerning the proper detection of multiple simultaneous contacts, better interpretation of consecutive contacts, and enabled the assessment of more detailed contact information by analyzing many podosomes within a reasonable time. This tool can now be used for different other questions as well, for example, to assess the contact behavior of MTs and focal adhesions or between vesicles and podosomes or other target structures.

Limits TrackMate/ContactAnalyzer

Although the development of this software-based analysis is a considerable improvement for contact analysis, there are still some limitations that have to be kept in mind. First, the specificity of the analysis depends on the quality of acquired microscopy movies. Further, the input files for the ContactAnalyzer program are generated by the object-tracking macro TrackMate. TrackMate requires the user to set a manual threshold for object recognition, which might be a source of aberrations. Additionally, only one blob size can be used, therefore, no adjustment for podosomes of different sizes was conducted. A similar shortcoming can be found in the ContactAnalyzer. Here, only one detection diameter is chosen for all podosomes and, optionally, another one for all MT+TIPs. In the case of podosome size differences, false positive or false negative contacts can be obtained, for big or small podosomes, respectively. Therefore, an individual assessment of analysis quality comparable to here performed verifications should be considered when used for differently acquired data and other approaches. Further, the directionality of moving +TIPs is not assessed in the current version of the ContactAnalyzer. Considering the +TIP course, and maybe even speed, in relation to podosome coordinates could improve the data and exclude false positives that, although close to a podosome, are presumably moving by and not actively contacting it. A differentiated analysis for speed can further improve the understanding of contact parameters.

Drebrin as new podosome cap component

Drebrin (developmentally regulated brain protein) was initially found in the embryonal chicken brain in 1985[176]. Therefore, it was mainly analyzed in a neuronal context and identified as an essential factor for neurite and dendrite elongation[177-182]. Here, the detailed localization of drebrin at podosomes in primary human macrophages is described for the first time. In particular, drebrin was identified as a novel component of the podosome cap. This was determined by using a 3-dimensional profile architecture of podosomes using Poji. Endogenous drebrin and drebrin-GFP were found to display a cap formation, i.e., a ring-like formation on the ventral side of the cell and a core-like on top of the podosome. Functioning in binding and bundling of F-actin fits with the localization of drebrin to the cap, which consists primarily of cross-linked and bundled filaments. Further, it was assessed by Poji analysis that drebrin localizes, compared to α-actinin, which is another bona fide cap protein[228], to a more peripheral part of the cap. Being in the peripheral, i.e., cytosol-accessible, layer of the podosome cap appears to be in line with drebrin being accessible for contact by microtubule +TIPs, making it an excellent candidate for being involved in the targeting process.

EB3 as a suitable +TIP marker

To establish a pipeline for live cell contact analysis in the system of primary human macrophages, the assessment of the best-suited markers for +TIPs was essential. Three +TIP markers that were already used in other contact studies[62, 215, 227] as a marker for growing microtubule plus ends (EB1, EB3, CLIP170) were tested for their qualification as part of the contact analysis pipeline. This assessment was an essential preliminary experiment since microtubule +TIP markers can have an impact on microtubule stability, dynamics[119-123], and, therefore, possibly also on this contact analysis. Also, the visual quality of the overexpression (OE), characterized by a good signal-to-noise ratio for more precise results, was tested.

The number of podosomes was comparable between cells with overexpression of EB1-, EB3- , or CLIP170-GFP (Figure 24). On the other hand, overexpressing these proteins leads to changes in the number of recorded +TIPs. While a very high number of +TIPs was detected in the CLIP170-GFP overexpression, only a low number of +TIPs was measured after EB1-GFP overexpression. These two differed with a p-value of 0.0006 very significantly from each other. EB3-GFP overexpression led to a number of +TIPs between the results for EB1 and CLIP170 (Figure 25). These differences in detected microtubule plus end numbers can have several reasons. On the one hand, the overexpression of +TIPs on its own has effects on microtubules[120,121,137]. Therefore, the stability and polymerization rate are potentially altered between the overexpression conditions. On the other hand, it was not assessed yet whether there are distinct microtubule subsets in human macrophages, which are preferentially decorated by one or the other +TIP. For more information about potential microtubule subsets, simultaneous endogenous staining of different +TIP markers might be beneficial.

After the number of podosomes and MT+TIPs was assessed, the analysis of contacts was performed. A comparable distribution with high numbers for CLIP170 overexpression, a moderate amount after EB3, and low numbers for EB1 overexpression were detected for raw and consecutive contacts as well as for the number of consecutive contacts per podosome (Figure 26, Figure 27, Figure 28). Since the amount of the visible +TIPs has a great influence on contacts, the EB3-GFP overexpression was chosen as a +TIP marker, which seems not to lead to higher chances of false positives (as CLIP170 might have) or too few contacts to see differences (as might have happened with EB1 OE). Further, EB3 is more proximally located at dynamic microtubule plus-ends than EB1[193]; therefore, it might be better suited to assess the contacts of microtubules to other structures. Additionally, EB3-GFP overexpression showed the best signal-to-noise ratio, ensuring high-quality live cell movies (Figure 23).

Target selection

The contact behavior of MT+TIPs is potentially affected by various podosome substructures. Therefore, known or recently identified proteins of the cap (INF2, supervillin, LSP1, drebrin), cortical microtubule stabilization complex (CMSC) proteins known for microtubule interaction (KANK1, ELKS), and podosome-associated hub or regulatory proteins (IQGAP1, PAK4) were chosen and tested if their depletion has effects on the contact parameters. Since only a limited number of candidates could be analyzed in the scope of this work, targets were chosen that were known to affect microtubule dynamics in other cell systems or in the context of focal adhesions. PAK4, for example, is known to influence podosome size and number[79, 156] and additionally plays a role in microtubule dynamics regulation[157-160]. Comparably, IQGAP1 was also found to interact with microtubules[163] and to play a role in the exocytosis[229] of MT1-MMP at invadopodia[165]. Furthermore, proteins of the CMSC[201-204], like KANK1 or ELKS, were shown to support the capture of microtubules at the cortex and were linked to mediating the contact between microtubules and focal adhesions[196, 198-200]. Finally, members of the podosome cap were chosen. Not only is the cap on the surface of the podosome structure, and therefore presumably easily accessible by microtubules, but it has several components known to regulate podosomes and interact with microtubules. For example, INF2 was shown to impact podosome formation[57], to affect their size[57], and was also found to bind, bundle and stabilize microtubules[173-175] and affect their posttranslational modifications[171, 174]. Therefore, it was assumed that these proteins might also play a role in the contact between podosomes and microtubules.

The general podosome parameters in still images were assessed to ensure that the changes were explicitly based on the respective depletion of a protein and not because of a general change in podosome structure (6.2.2). Smaller cell size was measured for cells depleted of INF2, which was already observed in an earlier study[57]. Additionally, an INF2 depletion also led to a comparable decrease in the number of podosomes, which resulted in an unchanged podosome density compared to the control. On the other hand, the podosome density was increased for LSP1-depleted cells and decreased in KANK1-depleted cells. The latter effect was shown in THP-1 as well. Here, the depletion of KANK1 led to a GEF-H1-mediated assembly of myosin IIA resulting in the disruption of podosomes[199]. However, the localization and behavior of GEF-H1 in human primary macrophages was not assessed yet.

After the primary assessment of the general cell and podosome parameters, the contact behavior was measured. First, the amount of MT+TIPs and podosomes in 30-minute live cell movies were analyzed. There were no significant differences in the number of podosomes or MT+TIPs in all different knockdown conditions. Therefore, it can be concluded that differences in other parameters, such as contacts and contact duration of drebrin, INF2, and LSP1

knockdown cells, are not due to differences in podosome amount or not due to differences in MT+TIP amount either. Noteworthy, especially in KANK1 and IQGAP1 knockdown, was found to have high standard deviations, i.e., wide variability of the measured data. The potential reasons for this variability are discussed below in the context of podosome microtubule contacts.

Analysis of these targets for impact on podosome-MT+TIP contact

After assessing the podosome and MT+TIP numbers, the analysis of the contacts between EB3-labeled microtubule +TIPs with podosomes was performed (Figure 32, Figure 33). Raw, as well as consecutive contacts, were strongly reduced (to remaining ~6 % compared to the control cells) for the drebrin knockdown condition; all other depletions did not lead to significant changes. Further, the spread of measured data points for the drebrin knockdown condition was strikingly less wide than observed for all other conditions, including the control. However, a wide variability of values was observed, especially in IQGAP, KANK1, ELKS, and INF2 knockdown, leading to a substantial standard deviation. This wide variability of values might be due to differences in the efficiency of the knockdowns. Although the efficiency was assessed by Western blotting, the acquisition of the live cell movies is performed on single cells, whereas Western blotting shows the mean of the cells of that sample. Therefore, the remaining expression level of the target proteins for the single analyzed cells is unknown. A further reason for higher variances might be the cell system: human primary macrophages are isolated from different donors, therefore displaying a different genetic background.

It was concluded that drebrin-depleted cells show impairment in podosome targeting by MT+TIPs since it was observed that the number of raw contacts is strongly decreased (more than 6-fold), although the number of podosomes and MT+TIPs does not differ from the control. Earlier, drebrin was found to bind EB3 directly [190] and also shown to form a complex with EB3, myosin IIB, and βII spectrin[230], possibly explaining the measured decrease in raw contacts. Furthermore, the number of measured consecutive contacts was significantly ($p = 0.0013$) lower than the control. These results suggest that drebrin plays a vital role in mediating the contact between podosomes and EB3-positive microtubule +TIPs.

In contrast to drebrin, a significant increase in contacts per podosome was observed for INF2 knockdown cells. Although INF2 knockdown cells were smaller in size, they still showed more contacts per podosome since they had lower numbers of podosomes and a comparable amount of MT+TIP contacts. This hints at a negative regulatory function of INF2 concerning the contact between podosomes and EB3-positive microtubule +TIPs. A potential mechanism

could be, for example, a sterical shielding of other cap components, like drebrin, from the microtubule plus ends. A superresolution approach, characterizing the spatial layers of the cap in high resolution, should be considered to gain more insights if this might be the case.

Intriguingly, when the contact duration was analyzed, i.e., the length of the contacts that were occurring in the different conditions, no changes in drebrin knockdown compared to the control condition were found. On the other hand, alterations in the contact duration were found for the cells with knockdown of cap proteins INF2 or LSP1, which were significantly in- or decreased, respectively. Potentially, the negative effect of INF2 on microtubule-podosome targeting is also playing a restrictive role in the process of sustaining the contact. On the other hand, LSP1, which was inconspicuous concerning the targeting, might be involved in stabilizing a microtubule-podosome contact. Although being part of the same podosome structure, i.e., the cap, INF2, LSP1, and drebrin seem to have different effects on the contact behavior of MT+TIPs with podosomes, indicating that not the cap structure itself but its individual components, play specific roles in the regulation of podosome-MT+TIP contact. Further, in this work, for example, drebrin appears wider than cap protein α-actinin, suggesting that the localization of cap proteins within this structure may vary and thus their accessibility for microtubule +TIPs.

Interestingly, no significant differences were found for KANK1 knockdown cells, neither in the number of contacts nor the contact duration, although KANK1 was reported to have essential functions at focal adhesions to bind talin, recruit CMSC proteins and therefore connect the adhesion structure with microtubules[196]. In the THP-1 human monocytic leukemia cell line, the KANK1 knockdown led to fewer microtubules in the ventral focal plane. Therefore, it was concluded that it plays a contact-mediating role for podosomes as well[199]. However, this effect was not as striking in this analysis, which might be due to more stable podosomes in human primary macrophages. THP-1 cells form podosomes only upon treatment with transforming growth factor beta 1 (TGFβ1) and undergo differentiation into macrophage-like cells[199]. For those cells, a complete disruption of podosomes was observed when treated with KANK1 siRNA, which was not observed in cells used in this work.

Nevertheless, in primary human macrophages depleted for KANK1, there is a tendency for fewer contacts and a shorter contact duration visible; however, the wide variability of values resulted in a non-significant outcome. This could argue for a more redundant role of KANK1 in human primary macrophages compared to THP-1 cells, as, for example, a ring-like localization of KANK2 was found at those podosomes[199]. Therefore, an analysis of KANK2 localization and analysis of the double knockdown of KANK1 and KANK2 in human primary macrophages might be interesting to perform. Additionally, it has to be considered that all detected podosomes and EB3-positive microtubules are included in this analysis; a differentiated

analysis of precursor and successor podosome subpopulations or analysis with different microtubule +TIP markers could show other results, as those subpopulations show for example differences in their dynamics. Further, for KANK1 knockdown cells, a significantly shortened lifetime was observed, as discussed later, with very dynamic podosomes, which might have increased the rate of false positive contacts. Therefore, the sample size should be increased to gain more reliable results and probably combined with a KANK1 staining after movie acquisition to ensure that only cells with an effective knockdown will be included in the analysis.

Nevertheless, from these results, it can be concluded that targeting podosomes and sustaining a contact are different processes since the number of contacts and the contact duration were altered independently from each other. Another interesting parameter that should be addressed in the future is the frequency of contacts, especially repeatedly contacted podosomes, and their consequences. Repeatedly contacted podosomes were associated with dissolution or fission/fusion of podosomes in former experiments[62], and with few adjustments in the function and evaluation of the program might lead to new insights into these phenomena. Pointing in this direction results not presented within this study showed an increasing number of contacts at the end of the podosome lifespan. This might be due to the altered composition of aging podosomes, such as increased content of supervillin, as shown earlier[58], or other components, which favor these contacts.

Functional consequences of different knockdown conditions

Further, whether the measured differences in contact numbers or contact duration also lead to functional consequences was investigated. Finally, since the podosome function includes adhesion, mechanosensitivity, and the modulation of the extracellular matrix, the degradative ability of macrophages was assessed. Therefore, the podosome lifetime, detailed structure, and capability to degrade gelatin were measured to gain insights into these aspects.

Podosome lifetime analysis

The lifetime of podosomes is also a general functional parameter assessed in this work. Therefore, first, the mean lifetime of podosomes was measured. A significant decrease was observed compared to the control condition after the KANK1 knockdown. Relatably, a lifetime reduction was also shown for podosomes in THP- 1 cells, based on the GEF-H1 release from

microtubules and a subsequent myosin IIA hyper-activation upon KANK1 knockdown[199]. However, the mechanism of this reduction of the podosome lifetime in KANK1-depleted cells has yet to be analyzed in primary human macrophages.

Nevertheless, since the mean lifetime, on its own, only gives limited information about the formation and regulation of podosomes, a more detailed analysis of podosome lifetime was performed by determining the frequency distribution of the different track lengths, i.e., podosome lifetimes. In the detailed lifetime analysis, in addition to KANK1 knockdown cells, macrophages depleted of INF2 show a significantly reduced amount of long-lived podosomes. This result contradicts a slight lifetime increase through an elevated long-lived podosome fraction published earlier in INF2-depleted human primary macrophages[57]. These differences might be due to different acquisition parameters (60x instead of 100x objective, 45 instead of 30 minutes, and a frame rate of 4× min^{-1} instead of 30× min^{-1}) or the Volocity (Perkin Elmer) based analysis instead of the here used TrackMate plugin for ImageJ described above.

Interestingly, although both, INF2 or KANK1 knockdown conditions, display a reduction in long-lived podosomes, they show contrasting results in their contact behavior, as discussed above. This brings to question if the lifetime reduction (or especially reduction of long-lived podosomes) and the contact behavior are not as directly correlated as postulated before[62]. In that case, a correlation between KIF1C-contacted podosomes and their fission or dissolution was observed. This might mean that a smaller or different subset of microtubules was tracked than by the visualization with EB3-GFP, or the overexpression of EB3 or KIF1C itself led to an effect. In addition, the analysis of different podosome subsets, i.e., precursor and successors, might show a further differentiated contact pattern. On the other hand, a detailed analysis of the difference between the number of contacts and their frequency still has to be performed.

Podosome architecture analysis

The intensity of core, cap, and ring staining was measured for two areas, the whole cell and the combined podosome area (CPA), with the latter including only the podosome-covered area and excluding the cortex and the area between podosomes. The measurement showed that none of the knockdowns affected the whole cell F-actin level. However, the loss of INF2 and KANK1 increased the F-actin portion in podosomes. Especially the higher F-actin intensity in INF2-depleted cells seems to be consistent with the published increase of core height and diameter upon INF2 siRNA treatment[57]. In the case of the cap representing α–actinin staining, a decrease was measured for the whole cell for the INF2 knockdown, whereas the other conditions showed unchanged levels. Interestingly, the measurement of the cap intensity was not decreased in INF2-depleted cells when only the podosome-covered area was analyzed. This argues for a regular α–actinin recruitment upon INF2 knockdown.

Strikingly, an increase in the α–actinin intensity in the combined podosome area was measured for the drebrin knockdown. This might indicate competing binding sites for α–actinin and drebrin in the podosome cap, as drebrin was published, for example, to dislocate tropomyosin from actin due to its high-affinity binding[182, 231]. Drebrin could also act as a negative regulator of α–actinin by its actin rearranging functions[185-187]. This finding suggests that a loss of drebrin leads to an altered cap composition. If other cap components are affected as well needs to be addressed in further experiments.

Lastly, the vinculin intensity was assessed. Whereas a decrease in the vinculin staining for the whole cell was observed for EB3-, INF2- and KANK1-depleted cells, a decreased vinculin intensity at podosomes was measured only for INF2 and KANK1 siRNA-treated cells. A decrease in the vinculin recruitment to the podosome ring suggests a change, i.e., a decrease in the contractile actomyosin forces of the structure[66]. Vinculin binds to stretched talin on the one hand; on the other, it stabilizes adhesion structures when tension rises[232]. Therefore, the loss of vinculin recruitment hints at decreased forces and/or stability of podosome rings in INF2- and KANK1 knockdown cells. Interestingly, vinculin, as well as KANK1, bind to talin[207], so instead of competing for binding sites, a cooperative binding mechanism might take place.

Gelatin degradation and surface MT1-MMP levels

Further, the functional consequences of the earlier alterations in contact behavior were investigated. To do so, macrophages that were depleted for the respective target proteins were tested for their ability to degrade rhodamine-labeled gelatin.

On the one hand, a significant loss of degradative capability was observed for INF2 or KANK1 siRNA-treated cells, probably caused by the reduced podosome lifetime in these knockdown conditions. However, on the other hand, a significant increase in the gelatin degradative capability of macrophages depleted of either EB3 or drebrin was observed. Interestingly, a simultaneous knockdown of both proteins did not lead to a further increase, suggesting that those two proteins act in the same pathway, consistent with the finding that the drebrin/EB3 pathway promotes the invasive activity of cancer cells[194].

Further, a possible explanation for the increase in degradation was checked. More degradation can have several non-exclusive reasons. For example, it might be due to increased protrusion of podosomes that would increase the contact between podosome-associated metalloproteases and the substrate. In addition, the lifetime of podosomes might play a role, as well as the amount and activity of proteases.

To gain insights into a potential mechanism, the surface level of MT1-MMP for the different knockdown conditions was measured using FACS. Interestingly, for INF2- or KANK1-depleted

cells, slightly increased MT1-MMP surface levels were detected. This suggests that the impaired degradation capability of these conditions is not due to a lack of protease. However, the activity of MT1-MMP was not assessed. In the case of the other conditions, it was observed that significantly higher amounts of surface MT1-MMP are detectable for cells depleted of EB3 or drebrin. Further, the simultaneous depletion of these two proteins did not show additive effects, consistent with the degradation assay results (Figure 41 and Figure 43). This again strengthens the hypothesis that EB3 and drebrin are part of the same pathway.

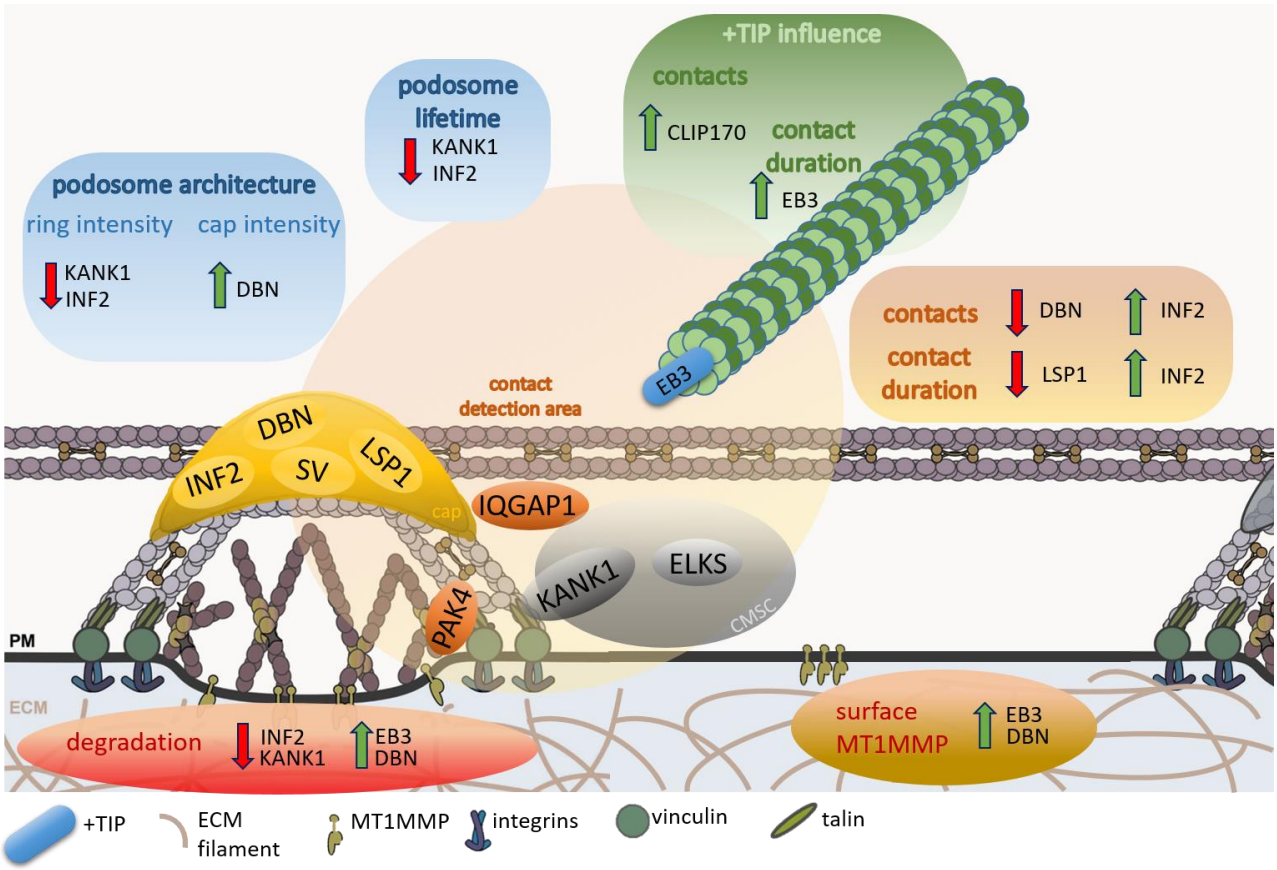

Figure 44: Graphical summary of main results.
Shown is a podosome and the targeted proteins, as well as a EB3 decorated microtubule plus end. The resulting impact of the depletion of the single targets is displayed for the podosome architecture and lifetime (blue boxes), the degradation capability (red ellipse), the MT1-MMP surface amount (orange ellipse) and the contact results (orange box). Further also the assessed impact of +TIP overexpression is displayed (green box). Modified from Weber et al., 2022.

The finding of altered MT1-MMP surface levels argues for a role of drebrin and EB3 in exo- and/or endocytosis. Accordingly, drebrin was shown, on the one hand, to suppress endocytosis[233, 234], for example, mediated by Rab5a positive vesicles[235]. On the other hand,

drebrin was recently published to promote cell migration by inducing integrin β1 endocytosis[236]. Interestingly, also EB3 was shown to play a role in endocytosis as is promotes virus uptake in a size-dependent endocytic pathway[237]. Probably drebrin acts at podosomes as a promoting or suppressing factor in dependence on the interacting protein. The increased MT1-MMP surface levels, accompanied by a significant reduction of microtubule podosome contacts, argue for an endocytosis-promoting function of the drebrin/EB3 interaction. Consequently, the depletion of either of them would lead to the observed accumulation of the protease at the cell surface.

However, it still has to be assessed experimentally whether the endocytosis rate of MT1-MMP is affected by the knockdown of EB3 and/or drebrin. This can be investigated, for example, by performing a biotinylation assay. The hereby-obtained results for primary human macrophages will allow conclusions on whether the elevated MT1-MMP levels are due to different regulatory effects of drebrin and EB3 interaction on endocytosis.

In contrast to the previously described conditions of drebrin and/or EB3 knockdown, a significant decrease in the degradation capability, as well as surface MT1-MMP amount for INF2 knockdown and KANK1 knockdown cells, was measured. The latter two seem to correlate with the significantly decreased podosome lifetime described earlier in this work (6.4.1). Moreover, a measurement of core polymerization dynamics and contractile forces should be considered since the loss of degradative capability, together with the presumably impaired podosome ring, argues for a change in protrusion. This seems consistent with published dampened oscillations of podosomes in INF2-depleted cells[57].

Implications of the new contact analysis

The analysis of contacts of this scale was not yet performed for podosomes or other adhesive structures like focal adhesions. Often smaller data sets were observed and analyzed[220]. In this thesis, a 1000-fold amount of +TIP signals was observed and analyzed per movie, which is only feasible due to the newly developed software-based approach. This large data set facilitates the assessment of different conditions and their impact on microtubule-podosome contacts and now offers the possibility to explore further related questions that could not be addressed previously.

This work initially focused on the tangible connection between microtubule contact with podosomes to facilitate motor protein-dependent MT1-MMP transport to the adhesion sites. Nevertheless, the complexity of this topic became obvious. For example, the preliminary

experiments assessing a suitable +TIP marker for the contact analysis suggest that the microtubules in primary human macrophages consist of different subsets as their number within cells and contact behavior was altered dependent on the overexpressed marker.

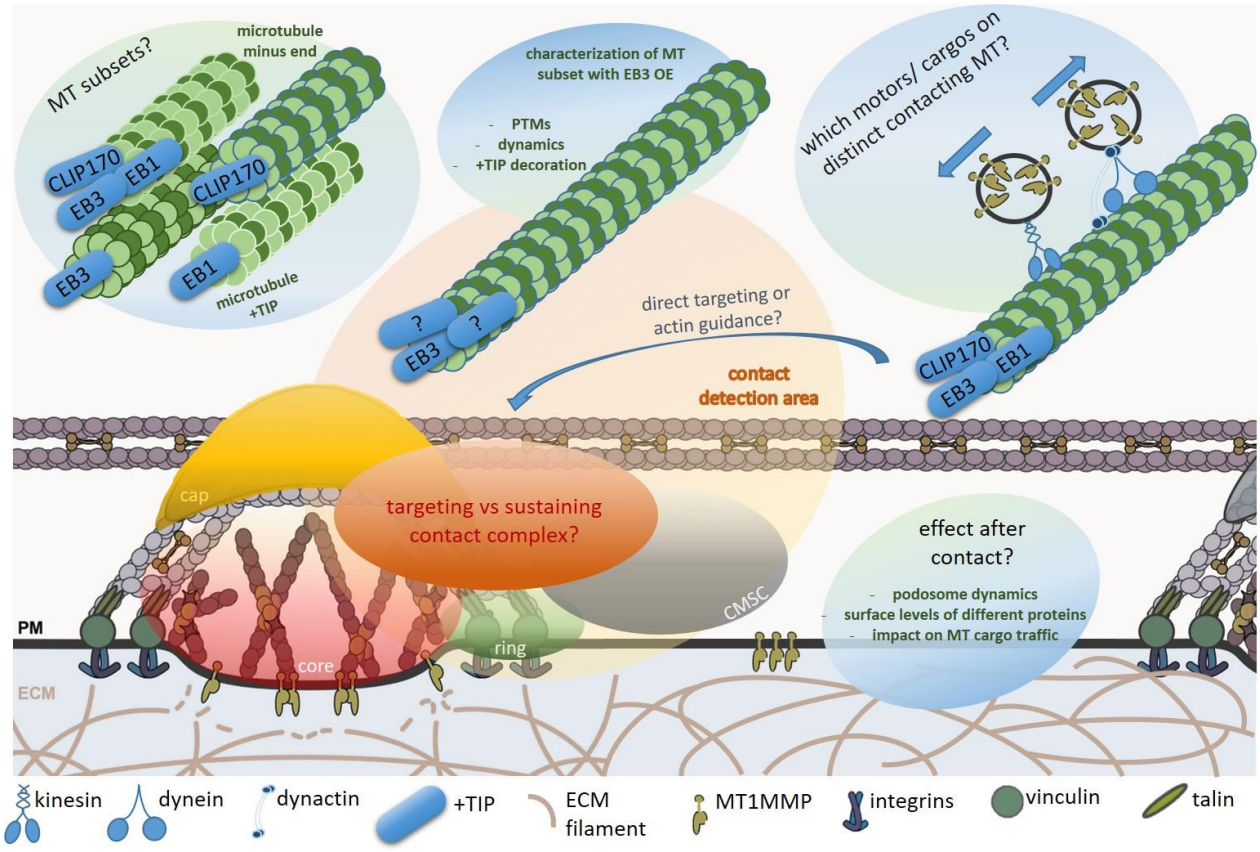

Figure 45: Scheme of open questions.

Graphical summary of some open questions. i) MT subsets are not characterized in conclusion for their impact and functions; ii) the MT subset analyzed here is characterized by EB3, but neither the complete +TIP complex nor the PTMs or dynamics of this specific subset were assessed; iii) the decoration with motor proteins and cargos for this MT subset was not assessed; iv) further effects after podosome MT contact (such as changes in podosome dynamics od surface levels of e.g. integrins) should be investigated and v) potentially a “contacting complex” can be defined including proteins of different structural parts of the podosome like the cap, core, ring or the presumably adjacent CMSC. Modified from Weber et al., 2022.

Potentially differently decorated microtubules not only display differences in targeting podosomes but induces differentiated effects on the adhesion sites. Next to the already mentioned vesicle delivery, processes like podosome dynamics such as fusion, fission,

dissolution, podosome rearrangement, and spacing can be affected. Another aspect might be microtubule contact triggering endocytosis and recycling events.

Especially concerning the latter aspect, continuing work on the role of the drebrin/EB3 pathway seems intriguing — particularly its interconnection with the observed MT1-MMP levels and, therefore, its potential role in endocytosis in primary human macrophages.

One additional conclusion drawn during this work is that the rhodamine-gelatin degradation assay was revealed to serve only as an initial readout for functional consequences of contacts between microtubules and contacts. Although the connection between microtubule contact and vesicle delivery is still valid, podosome degradation capability depends on several aspects, such as regular podosome architecture, different substrate rigidities, and occurring contractile forces. Therefore, more specific experiments need to be performed, or the degradation assay results should be supported by further experiments like surface MT1-MMP detection, as done in this work. Nevertheless, additional experiments should be considered as proposed in the outlook for mechanistic insights.

Further analysis, including the analysis of different microtubule subsets and additional targets, might reveal a more elaborate “contactosome”, a complex of proteins that play a role in the microtubule-podosome contact. It is not excluded that members of this potential complex are allocated in different structures like the podosome ring or cap, as well as the cortical microtubule stabilizing complex, which has been mainly described for focal adhesions.

Collectively, a new tool was developed within this work that allows a significantly improved and more detailed analysis of microtubule-podosome contacts. Besides the characterization of drebrin as a new cap protein, the differential influence of the cap proteins drebrin, LSP1, and INF2 for these contacts could be identified. In addition, a shortened podosome lifespan was recorded for INF2 and KANK1 deletions, which was associated with reduced extracellular matrix degradation. On the other hand, an increase of gelatin degradative capability was observed for cells with drebrin and/or EB3 depletion, correlating with an increase of cell surface located MT1-MMP as well as total MT1-MMP amount, suggesting that the interaction of microtubules decorated with +TIP EB3 and drebrin at the podosome cap plays an important role for endocytosis.

8 Outlook

The analysis of the interaction of two major cytoskeleton components such as microtubules and actin-based podosomes offers many options for further research. In this work, only a small portion of proteins was analyzed for the possible interactome. Other proteins like CLASP (CLIP-associating proteins, CLIP: cytoplasmic linker protein) or APC (adenomatous-polyposis-coli) that were found to induce microtubule growth guided along actin bundles and coordinate axon elongation[238, 239] or directional cell migration[240] could be included in further analyses.

With the development of this version of the “ContactAnalyzer”, a vast amount of data was generated. Moreover, further adjustments to the program, as well as the analysis and evaluation of the data, could lead to more detailed insights concerning the dynamics of microtubule-podosome contacts. Especially the development of the differentiated analysis of podosome subpopulations, i.e., precursors and successors, might be helpful. Furthermore, adding a fate analysis of podosomes after microtubule contact to see its impact on fusion and fission dynamics should be considered as well. Moreover, the directionality and speed of +TIPs could be incorporated and bring further insights. A screening with more +TIP markers can potentially add more information to the general understanding of contact dynamics. For more information about potential microtubule subsets simultaneous endogenous staining of different +TIP marker might be beneficial. Additionally, a proximity-ligation-assay (PLA) between several +TIPs and drebrin or other cap components promises interesting results.

Since the visualization of MT+TIPs already influences the contact dynamics, other microtubule plus end markers should be tested or even constructed, like an EB3-GFP construct that does not bind drebrin. Also, other factors that impact microtubules, like posttranslational modifications (tyrosination, detyrosination, polyglutamylation), should be considered and analyzed.

An exciting outcome of this work was the results of the functional consequences found when analyzing the ability of the treated macrophages to degrade extracellular matrix. It was shown that the gelatin degradation is reduced, and the concrete mechanism has yet to be found. Potential cues might be gained by performing the degradation assay on other substrates like collagen or fibronectin as well. Further, also the activity of the different proteases might be assessed, the endocytosis analyzed by biotinylation assays and protrusion force tested with Elastic Resonator Interference Stress Microscopy (ERISM) to gain more mechanistic insights for the connection between the contacts, the degradative capability of podosomes and the MT1-MMP levels.

9 List of abbreviations

Abbreviation	
+TIPs	microtubule plus-end tracking proteins
µm	micro meters
ADP	adenosine diphosphate
ANOVA	analysis of variance
Arp2/3	actin related protein 2/3
ATP	adenosine triphosphate
CD44	cluster of differentiation protein 44
CDC42	cell division control protein 42
CH-domain	calponin homology domain
CLASP1	CLIP-associating protein 1
CLIP170	Cytoplasmic linker protein 170
CMSC	cortical microtubule stabilizing complex
CPA	combined podosome area
CSV	comma-separated values, file format
DAD	diaphanous autoregulatory domain
DBN	drebrin
DID	diaphanous inhibitory domain
drebrin	developmentally regulated brain protein
e. g.	exempli gratia
EB1	end binding protein 1
EB3	end binding protein 3
ECM	extracellular matrix
ELKS	protein rich in the amino acids E, L, K and S
ER	endoplasmatic reticulum
ERISM	Elastic Resonator Interference Stress Microscopy

FA	focal adhesions
FACS	fluorescence activated cell sorting
F-actin	filamentous actin
FMNL1	formin-like protein 1
FWHH	full width at half heigh
G-actin	globular actin
GDP	guanosine diphosphate
GEF	guanine nucleotide exchange factor
GFP	green fluorescent protein
GTP	guanosine triphosphate
HEK293	human embryonic kidney fibroblast cell line
HUVEC	human endothelial cells
i. e.	id est
INF2	inverted formin 2
IQGAP	IQ motif containing GTPase-activating protein
KANK1	KN motif and ankyrin repeat domain-containing complex
KD	knockdown
kDa	kilo Dalton
LSP1	lymphocyte-specific protein 1
MAPs	microtubule-associated proteins
min	minutes
MMPs	matrix metalloproteases
MT	microtubule
MT1-MMP	membrane type 1 – matrix metalloprotease
MTOC	microtubule organizing center
n	sample size
OE	overexpression

p	p-value
PAK4	p21-activated kinase 4
PAMPs	pathogen-associated molecular patterns
PFM	Protrusion Force Microscopy
Poji	podosome analysis by Fiji
PTMs	posttranslational modifications
px	pixels
QQ-Plot	Quantile-Quantile-plot
RFP	red fluorescent protein
RNA	ribonucleic acid
ROCK	Rho-associated protein kinase
ROS	reactive oxygen species
s	seconds
SD	standard deviation
SEM	standard error of the mean
siRNA	small interfering RNA
SKAP	small kinetochore-associated protein
SV	supervillin
TAMs	tumor-associated macrophages
TGF-β	transcriptional growth factor β
TIRF(-M)	total internal reflection (microscopy)
WASP	Wiskott–Aldrich Syndrome protein
XML	extensible markup language, file format

10 List of figures

11 List of tables

12 References

1. Zhao, Y., Zou, W., Du, J. & Zhao, Y. The origins and homeostasis of monocytes and tissue-resident macrophages in physiological situation. *Journal of cellular physiology* **233**, 6425-6439 (2018).
2. van Furth, R. & Cohn, Z.A. The origin and kinetics of mononuclear phagocytes. *The Journal of experimental medicine* **128**, 415-435 (1968).
3. de Kruif, P. *The Microbe Hunters*. (Harcourt, Brace and Jovanovich, San Diego, 1954).
4. Maximow, A.A. *The Macrophages or Histiocytes.*, Vol. II. (Special Cytology, New York; 1932).
5. Ginhoux, F. & Jung, S. Monocytes and macrophages: developmental pathways and tissue homeostasis. *Nature reviews. Immunology* **14**, 392-404 (2014).
6. Yona, S. *et al.* Fate mapping reveals origins and dynamics of monocytes and tissue macrophages under homeostasis. *Immunity* **38**, 79-91 (2013).
7. Schulz, C. *et al.* A lineage of myeloid cells independent of Myb and hematopoietic stem cells. *Science (New York, N.Y.)* **336**, 86-90 (2012).
8. Merad, M. *et al.* Langerhans cells renew in the skin throughout life under steady-state conditions. *Nat Immunol* **3**, 1135-1141 (2002).
9. Gordon, S. & Taylor, P.R. Monocyte and macrophage heterogeneity. *Nature Reviews Immunology* **5**, 953-964 (2005).
10. Murray, P.J. & Wynn, T.A. Protective and pathogenic functions of macrophage subsets. *Nature reviews. Immunology* **11**, 723-737 (2011).
11. Murray, P.J. *et al.* Macrophage activation and polarization: nomenclature and experimental guidelines. *Immunity* **41**, 14-20 (2014).
12. Ginhoux, F., Schultze, J.L., Murray, P.J., Ochando, J. & Biswas, S.K. New insights into the multidimensional concept of macrophage ontogeny, activation and function. *Nat Immunol* **17**, 34-40 (2016).
13. Sica, A. & Mantovani, A. Macrophage plasticity and polarization: in vivo veritas. *J Clin Invest* **122**, 787-795 (2012).
14. Mogensen, T.H. Pathogen recognition and inflammatory signaling in innate immune defenses. *Clin Microbiol Rev* **22**, 240-273, Table of Contents (2009).
15. Varol, C., Mildner, A. & Jung, S. Macrophages: development and tissue specialization. *Annu Rev Immunol* **33**, 643-675 (2015).
16. Gordon, S. Phagocytosis: An Immunobiologic Process. *Immunity* **44**, 463-475 (2016).
17. Mantovani, A. *et al.* The chemokine system in diverse forms of macrophage activation and polarization. *Trends Immunol* **25**, 677-686 (2004).
18. Lawrence, T. & Natoli, G. Transcriptional regulation of macrophage polarization: enabling diversity with identity. *Nature reviews. Immunology* **11**, 750-761 (2011).
19. Mills, C.D., Harris, R.A. & Ley, K. Macrophage Polarization: Decisions That Affect Health. *J Clin Cell Immunol* **6** (2015).
20. Biswas, S.K. & Mantovani, A. Macrophage plasticity and interaction with lymphocyte subsets: cancer as a paradigm. *Nat Immunol* **11**, 889-896 (2010).
21. Mantovani, A., Allavena, P., Sica, A. & Balkwill, F. Cancer-related inflammation. *Nature* **454**, 436-444 (2008).
22. Friedl, P. & Wolf, K. Plasticity of cell migration: a multiscale tuning model. *The Journal of cell biology* **188**, 11-19 (2010).
23. Van Goethem, E., Poincloux, R., Gauffre, F., Maridonneau-Parini, I. & Le Cabec, V. Matrix architecture dictates three-dimensional migration modes of human macrophages: differential involvement of proteases and podosome-like structures. *Journal of immunology* **184**, 1049-1061 (2010).

24. Wiesner, C., Le-Cabec, V., El Azzouzi, K., Maridonneau-Parini, I. & Linder, S. Podosomes in space: macrophage migration and matrix degradation in 2D and 3D settings. *Cell adhesion & migration* **8**, 179-191 (2014).
25. Linder, S. The matrix corroded: podosomes and invadopodia in extracellular matrix degradation. *Trends in cell biology* **17**, 107-117 (2007).
26. David-Pfeuty, T. & Singer, S.J. Altered distributions of the cytoskeletal proteins vinculin and alpha-actinin in cultured fibroblasts transformed by Rous sarcoma virus. *Proceedings of the National Academy of Sciences of the United States of America* **77**, 6687-6691 (1980).
27. Lehto, V.P., Hovi, T., Vartio, T., Badley, R.A. & Virtanen, I. Reorganization of cytoskeletal and contractile elements during transition of human monocytes into adherent macrophages. *Laboratory investigation; a journal of technical methods and pathology* **47**, 391-399 (1982).
28. Osiak, A.E., Zenner, G. & Linder, S. Subconfluent endothelial cells form podosomes downstream of cytokine and RhoGTPase signaling. *Experimental cell research* **307**, 342-353 (2005).
29. Varon, C. *et al.* Transforming growth factor beta induces rosettes of podosomes in primary aortic endothelial cells. *Molecular and cellular biology* **26**, 3582-3594 (2006).
30. Gimona, M., Kaverina, I., Resch, G.P., Vignal, E. & Burgstaller, G. Calponin repeats regulate actin filament stability and formation of podosomes in smooth muscle cells. *Molecular biology of the cell* **14**, 2482-2491 (2003).
31. Burgstaller, G. & Gimona, M. Actin cytoskeleton remodelling via local inhibition of contractility at discrete microdomains. *Journal of cell science* **117**, 223-231 (2004).
32. Moreau, V., Tatin, F., Varon, C. & Génot, E. Actin can reorganize into podosomes in aortic endothelial cells, a process controlled by Cdc42 and RhoA. *Molecular and cellular biology* **23**, 6809-6822 (2003).
33. Schachtner, H. *et al.* Megakaryocytes assemble podosomes that degrade matrix and protrude through basement membrane. *Blood* **121**, 2542-2552 (2013).
34. Johansson, M.W. *et al.* Eosinophils adhere to vascular cell adhesion molecule-1 via podosomes. *Am J Respir Cell Mol Biol* **31**, 413-422 (2004).
35. Linder, S., Nelson, D., Weiss, M. & Aepfelbacher, M. Wiskott-Aldrich syndrome protein regulates podosomes in primary human macrophages. *Proceedings of the National Academy of Sciences of the United States of America* **96**, 9648-9653 (1999).
36. Burns, S., Thrasher, A.J., Blundell, M.P., Machesky, L. & Jones, G.E. Configuration of human dendritic cell cytoskeleton by Rho GTPases, the WAS protein, and differentiation. *Blood* **98**, 1142-1149 (2001).
37. Marchisio, P.C. *et al.* Cell-substratum interaction of cultured avian osteoclasts is mediated by specific adhesion structures. *The Journal of cell biology* **99**, 1696-1705 (1984).
38. Destaing, O., Saltel, F., Geminard, J.C., Jurdic, P. & Bard, F. Podosomes display actin turnover and dynamic self-organization in osteoclasts expressing actin-green fluorescent protein. *Molecular biology of the cell* **14**, 407-416 (2003).
39. Zamir, E. & Geiger, B. Molecular complexity and dynamics of cell-matrix adhesions. *Journal of cell science* **114**, 3583-3590 (2001).
40. Albiges-Rizo, C., Destaing, O., Fourcade, B., Planus, E. & Block, M.R. Actin machinery and mechanosensitivity in invadopodia, podosomes and focal adhesions. *Journal of cell science* **122**, 3037-3049 (2009).
41. Linder, S. Invadosomes at a glance. *Journal of cell science* **122**, 3009-3013 (2009).
42. Yamaguchi, H. *et al.* Molecular mechanisms of invadopodium formation: the role of the N-WASP-Arp2/3 complex pathway and cofilin. *The Journal of cell biology* **168**, 441-452 (2005).
43. Linder, S. *et al.* The polarization defect of Wiskott-Aldrich syndrome macrophages is linked to dislocalization of the Arp2/3 complex. *Journal of immunology* **165**, 221-225 (2000).
44. Mizutani, K., Miki, H., He, H., Maruta, H. & Takenawa, T. Essential role of neural Wiskott-Aldrich syndrome protein in podosome formation and degradation of

extracellular matrix in src-transformed fibroblasts. *Cancer research* **62**, 669-674 (2002).
45. Pfaff, M. & Jurdic, P. Podosomes in osteoclast-like cells: structural analysis and cooperative roles of paxillin, proline-rich tyrosine kinase 2 (Pyk2) and integrin alphaVbeta3. *Journal of cell science* **114**, 2775-2786 (2001).
46. Linder, S. & Aepfelbacher, M. Podosomes: adhesion hot-spots of invasive cells. *Trends in cell biology* **13**, 376-385 (2003).
47. Zambonin-Zallone, A. *et al.* Immunocytochemical distribution of extracellular matrix receptors in human osteoclasts: a beta 3 integrin is colocalized with vinculin and talin in the podosomes of osteoclastoma giant cells. *Experimental cell research* **182**, 645-652 (1989).
48. van den Dries, K. *et al.* Dual-color superresolution microscopy reveals nanoscale organization of mechanosensory podosomes. *Molecular biology of the cell* **24**, 2112-2123 (2013).
49. Walde, M., Monypenny, J., Heintzmann, R., Jones, G.E. & Cox, S. Vinculin binding angle in podosomes revealed by high resolution microscopy. *PloS one* **9**, e88251 (2014).
50. Linder, S. & Wiesner, C. Tools of the trade: podosomes as multipurpose organelles of monocytic cells. *Cellular and molecular life sciences : CMLS* **72**, 121-135 (2015).
51. Labernadie, A. *et al.* Protrusion force microscopy reveals oscillatory force generation and mechanosensing activity of human macrophage podosomes. *Nature communications* **5**, 5343 (2014).
52. Labernadie, A., Thibault, C., Vieu, C., Maridonneau-Parini, I. & Charrière, G.M. Dynamics of podosome stiffness revealed by atomic force microscopy. *Proceedings of the National Academy of Sciences of the United States of America* **107**, 21016-21021 (2010).
53. van den Dries, K. *et al.* Interplay between myosin IIA-mediated contractility and actin network integrity orchestrates podosome composition and oscillations. *Nature communications* **4**, 1412 (2013).
54. Akisaka, T., Yoshida, H., Suzuki, R. & Takama, K. Adhesion structures and their cytoskeleton-membrane interactions at podosomes of osteoclasts in culture. *Cell and tissue research* **331**, 625-641 (2008).
55. Luxenburg, C. *et al.* The architecture of the adhesive apparatus of cultured osteoclasts: from podosome formation to sealing zone assembly. *PloS one* **2**, e179 (2007).
56. Mersich, A.T., Miller, M.R., Chkourko, H. & Blystone, S.D. The formin FRL1 (FMNL1) is an essential component of macrophage podosomes. *Cytoskeleton (Hoboken, N.J.)* **67**, 573-585 (2010).
57. Panzer, L. *et al.* The formins FHOD1 and INF2 regulate inter- and intra-structural contractility of podosomes. *Journal of cell science* **129**, 298-313 (2016).
58. Bhuwania, R. *et al.* Supervillin couples myosin-dependent contractility to podosomes and enables their turnover. *Journal of cell science* **125**, 2300-2314 (2012).
59. Cervero, P., Wiesner, C., Bouissou, A., Poincloux, R. & Linder, S. Lymphocyte-specific protein 1 regulates mechanosensory oscillation of podosomes and actin isoform-based actomyosin symmetry breaking. *Nature communications* **9**, 515 (2018).
60. Weber, K., Hey, S., Cervero, P. & Linder, S. The circle of life: Phases of podosome formation, turnover and reemergence. *European journal of cell biology* **101**, 151218 (2022).
61. Evans, J.G., Correia, I., Krasavina, O., Watson, N. & Matsudaira, P. Macrophage podosomes assemble at the leading lamella by growth and fragmentation. *The Journal of cell biology* **161**, 697-705 (2003).
62. Kopp, P. *et al.* The kinesin KIF1C and microtubule plus ends regulate podosome dynamics in macrophages. *Molecular biology of the cell* **17**, 2811-2823 (2006).

63. Proag, A., Bouissou, A., Vieu, C., Maridonneau-Parini, I. & Poincloux, R. Evaluation of the force and spatial dynamics of macrophage podosomes by multi-particle tracking. *Methods (San Diego, Calif.)* **94**, 75-84 (2016).
64. Proag, A. *et al.* Working Together: Spatial Synchrony in the Force and Actin Dynamics of Podosome First Neighbors. *ACS Nano* **9**, 3800-3813 (2015).
65. Bouissou, A. *et al.* Podosome Force Generation Machinery: A Local Balance between Protrusion at the Core and Traction at the Ring. *ACS Nano* **11**, 4028-4040 (2017).
66. del Rio, A. *et al.* Stretching single talin rod molecules activates vinculin binding. *Science (New York, N.Y.)* **323**, 638-641 (2009).
67. Linder, S. & Wiesner, C. Feel the force: Podosomes in mechanosensing. *Experimental cell research* **343**, 67-72 (2016).
68. Linder, S., Wiesner, C. & Himmel, M. Degrading devices: invadosomes in proteolytic cell invasion. *Annu Rev Cell Dev Biol* **27**, 185-211 (2011).
69. Wiesner, C., Faix, J., Himmel, M., Bentzien, F. & Linder, S. KIF5B and KIF3A/KIF3B kinesins drive MT1-MMP surface exposure, CD44 shedding, and extracellular matrix degradation in primary macrophages. *Blood* **116**, 1559-1569 (2010).
70. Huveneers, S., Arslan, S., van de Water, B., Sonnenberg, A. & Danen, E.H. Integrins uncouple Src-induced morphological and oncogenic transformation. *The Journal of biological chemistry* **283**, 13243-13251 (2008).
71. Yu, C.H. *et al.* Integrin-matrix clusters form podosome-like adhesions in the absence of traction forces. *Cell reports* **5**, 1456-1468 (2013).
72. Pal, K., Tu, Y. & Wang, X. Single-Molecule Force Imaging Reveals That Podosome Formation Requires No Extracellular Integrin-Ligand Tensions or Interactions. *ACS Nano* (2022).
73. Luxenburg, C., Winograd-Katz, S., Addadi, L. & Geiger, B. Involvement of actin polymerization in podosome dynamics. *Journal of cell science* **125**, 1666-1672 (2012).
74. Sit, S.-T. & Manser, E. Rho GTPases and their role in organizing the actin cytoskeleton. *Journal of cell science* **124**, 679-683 (2011).
75. van den Dries, K., Linder, S., Maridonneau-Parini, I. & Poincloux, R. Probing the mechanical landscape - new insights into podosome architecture and mechanics. *Journal of cell science* **132** (2019).
76. van den Dries, K. *et al.* Modular actin nano-architecture enables podosome protrusion and mechanosensing. *Nature communications* **10**, 5171 (2019).
77. Gu, Z., Kordowska, J., Williams, G.L., Wang, C.L. & Hai, C.M. Erk1/2 MAPK and caldesmon differentially regulate podosome dynamics in A7r5 vascular smooth muscle cells. *Experimental cell research* **313**, 849-866 (2007).
78. Van Audenhove, I., Debeuf, N., Boucherie, C. & Gettemans, J. Fascin actin bundling controls podosome turnover and disassembly while cortactin is involved in podosome assembly by its SH3 domain in THP-1 macrophages and dendritic cells. *Biochimica et Biophysica Acta (BBA) - Molecular Cell Research* **1853**, 940-952 (2015).
79. Gringel, A. *et al.* PAK4 and alphaPIX determine podosome size and number in macrophages through localized actin regulation. *Journal of cellular physiology* **209**, 568-579 (2006).
80. Hey, S., Ratt, A. & Linder, S. There and back again: Intracellular trafficking, release and recycling of matrix metalloproteinases. *Biochim Biophys Acta Mol Cell Res* **1869**, 119189 (2022).
81. Pal, K., Zhao, Y., Wang, Y. & Wang, X. Ubiquitous membrane-bound DNase activity in podosomes and invadopodia. *Journal of Cell Biology* **220** (2021).
82. Wiesner, C., El Azzouzi, K. & Linder, S. A specific subset of RabGTPases controls cell surface exposure of MT1-MMP, extracellular matrix degradation and three-dimensional invasion of macrophages. *Journal of cell science* **126**, 2820-2833 (2013).
83. El Azzouzi, K., Wiesner, C. & Linder, S. Metalloproteinase MT1-MMP islets act as memory devices for podosome reemergence. *The Journal of cell biology* **213**, 109-125 (2016).

84. Rafiq, N.B.M. *et al.* Forces and constraints controlling podosome assembly and disassembly. *Philosophical transactions of the Royal Society of London. Series B, Biological sciences* **374**, 20180228 (2019).
85. van Helden, S.F. *et al.* PGE2-mediated podosome loss in dendritic cells is dependent on actomyosin contraction downstream of the RhoA-Rho-kinase axis. *Journal of cell science* **121**, 1096-1106 (2008).
86. Calle, Y., Carragher, N.O., Thrasher, A.J. & Jones, G.E. Inhibition of calpain stabilises podosomes and impairs dendritic cell motility. *Journal of cell science* **119**, 2375-2385 (2006).
87. Yu, X. *et al.* N-WASP coordinates the delivery and F-actin-mediated capture of MT1-MMP at invasive pseudopods. *The Journal of cell biology* **199**, 527-544 (2012).
88. Pollard, T.D. & Borisy, G.G. Cellular motility driven by assembly and disassembly of actin filaments. *Cell* **112**, 453-465 (2003).
89. Ross, J.L., Ali, M.Y. & Warshaw, D.M. Cargo transport: molecular motors navigate a complex cytoskeleton. *Curr Opin Cell Biol* **20**, 41-47 (2008).
90. Alberti, C. Cytoskeleton structure and dynamic behaviour: quick excursus from basic molecular mechanisms to some implications in cancer chemotherapy. *European review for medical and pharmacological sciences* **13**, 13-21 (2009).
91. Asparuhova, M.B., Gelman, L. & Chiquet, M. Role of the actin cytoskeleton in tuning cellular responses to external mechanical stress. *Scandinavian journal of medicine & science in sports* **19**, 490-499 (2009).
92. Tang, D.D. & Gerlach, B.D. The roles and regulation of the actin cytoskeleton, intermediate filaments and microtubules in smooth muscle cell migration. *Respiratory research* **18**, 54 (2017).
93. Svitkina, T. The Actin Cytoskeleton and Actin-Based Motility. *Cold Spring Harbor perspectives in biology* **10** (2018).
94. Spudich, J.A. & Cooke, R. Supramolecular forms of actin from amoebae of Dictyostelium discoideum. *The Journal of biological chemistry* **250**, 7485-7491 (1975).
95. Ledbetter, M.C. & Porter, K.R. A "MICROTUBULE" IN PLANT CELL FINE STRUCTURE. *The Journal of cell biology* **19**, 239-250 (1963).
96. Kim, S. & Coulombe, P.A. Intermediate filament scaffolds fulfill mechanical, organizational, and signaling functions in the cytoplasm. *Genes & development* **21**, 1581-1597 (2007).
97. Mostowy, S. & Cossart, P. Septins: the fourth component of the cytoskeleton. *Nature reviews. Molecular cell biology* **13**, 183-194 (2012).
98. Fujii, T., Iwane, A.H., Yanagida, T. & Namba, K. Direct visualization of secondary structures of F-actin by electron cryomicroscopy. *Nature* **467**, 724-728 (2010).
99. Alberts, B. *et al. Molecular Biology of the Cell*. (Garland Science, 2014).
100. Blanchoin, L., Boujemaa-Paterski, R., Sykes, C. & Plastino, J. Actin dynamics, architecture, and mechanics in cell motility. *Physiological reviews* **94**, 235-263 (2014).
101. Welch, M.D. & Mullins, R.D. Cellular control of actin nucleation. *Annu Rev Cell Dev Biol* **18**, 247-288 (2002).
102. Desai, A. & Mitchison, T.J. Microtubule polymerization dynamics. *Annu Rev Cell Dev Biol* **13**, 83-117 (1997).
103. Akhmanova, A. & Steinmetz, M.O. Tracking the ends: a dynamic protein network controls the fate of microtubule tips. *Nature reviews. Molecular cell biology* **9**, 309-322 (2008).
104. Mimori-Kiyosue, Y. & Tsukita, S. "Search-and-capture" of microtubules through plus-end-binding proteins (+TIPs). *Journal of biochemistry* **134**, 321-326 (2003).
105. Valiron, O., Caudron, N. & Job, D. Microtubule dynamics. *Cellular and molecular life sciences : CMLS* **58**, 2069-2084 (2001).
106. Gundersen, G.G. & Bulinski, J.C. Selective stabilization of microtubules oriented toward the direction of cell migration. *Proceedings of the National Academy of Sciences of the United States of America* **85**, 5946-5950 (1988).

107. Waters, A.M. & Beales, P.L. Ciliopathies: an expanding disease spectrum. *Pediatr Nephrol* **26**, 1039-1056 (2011).
108. Matamoros, A.J. & Baas, P.W. Microtubules in health and degenerative disease of the nervous system. *Brain research bulletin* **126**, 217-225 (2016).
109. Jordan, M.A. & Wilson, L. Microtubules as a target for anticancer drugs. *Nat Rev Cancer* **4**, 253-265 (2004).
110. Job, D., Valiron, O. & Oakley, B. Microtubule nucleation. *Curr Opin Cell Biol* **15**, 111-117 (2003).
111. van der Vaart, B., Akhmanova, A. & Straube, A. Regulation of microtubule dynamic instability. *Biochemical Society transactions* **37**, 1007-1013 (2009).
112. Watanabe, T., Noritake, J. & Kaibuchi, K. Regulation of microtubules in cell migration. *Trends in cell biology* **15**, 76-83 (2005).
113. van de Willige, D., Hoogenraad, C.C. & Akhmanova, A. Microtubule plus-end tracking proteins in neuronal development. *Cellular and Molecular Life Sciences* **73**, 2053-2077 (2016).
114. Janke, C. & Magiera, M.M. The tubulin code and its role in controlling microtubule properties and functions. *Nature reviews. Molecular cell biology* **21**, 307-326 (2020).
115. Roll-Mecak, A. The Tubulin Code in Microtubule Dynamics and Information Encoding. *Developmental cell* **54**, 7-20 (2020).
116. Akhmanova, A. & Kapitein, L.C. Mechanisms of microtubule organization in differentiated animal cells. *Nature reviews. Molecular cell biology* **23**, 541-558 (2022).
117. Katrukha, E.A., Jurriens, D., Salas Pastene, D.M. & Kapitein, L.C. Quantitative mapping of dense microtubule arrays in mammalian neurons. *eLife* **10**, e67925 (2021).
118. Kobayashi, Y. & Mohri, H. Microheterogeneity of alpha and beta subunit of tubulin from microtubules of starfish (Asterias amurensis) sperm flagella. *Journal of molecular biology* **116**, 613-617 (1977).
119. Bodakuntla, S., Jijumon, A.S., Villablanca, C., Gonzalez-Billault, C. & Janke, C. Microtubule-Associated Proteins: Structuring the Cytoskeleton. *Trends in cell biology* **29**, 804-819 (2019).
120. Komarova, Y. *et al.* Mammalian end binding proteins control persistent microtubule growth. *The Journal of cell biology* **184**, 691-706 (2009).
121. Maurer, S.P. *et al.* EB1 accelerates two conformational transitions important for microtubule maturation and dynamics. *Current biology : CB* **24**, 372-384 (2014).
122. Maurer, S.P., Fourniol, F.J., Bohner, G., Moores, C.A. & Surrey, T. EBs recognize a nucleotide-dependent structural cap at growing microtubule ends. *Cell* **149**, 371-382 (2012).
123. Zhang, R., Alushin, G.M., Brown, A. & Nogales, E. Mechanistic Origin of Microtubule Dynamic Instability and Its Modulation by EB Proteins. *Cell* **162**, 849-859 (2015).
124. Hayashi, I. & Ikura, M. Crystal structure of the amino-terminal microtubule-binding domain of end-binding protein 1 (EB1). *The Journal of biological chemistry* **278**, 36430-36434 (2003).
125. Slep, K.C. & Vale, R.D. Structural basis of microtubule plus end tracking by XMAP215, CLIP-170, and EB1. *Molecular cell* **27**, 976-991 (2007).
126. Xia, P. *et al.* Superresolution imaging reveals structural features of EB1 in microtubule plus-end tracking. *Molecular biology of the cell* **25**, 4166-4173 (2014).
127. Mimori-Kiyosue, Y., Shiina, N. & Tsukita, S. The dynamic behavior of the APC-binding protein EB1 on the distal ends of microtubules. *Current biology : CB* **10**, 865-868 (2000).
128. Seetapun, D., Castle, B.T., McIntyre, A.J., Tran, P.T. & Odde, D.J. Estimating the microtubule GTP cap size in vivo. *Current biology : CB* **22**, 1681-1687 (2012).
129. Jiang, K. *et al.* A Proteome-wide screen for mammalian SxIP motif-containing microtubule plus-end tracking proteins. *Current biology : CB* **22**, 1800-1807 (2012).
130. Yue, J. *et al.* Microtubules regulate focal adhesion dynamics through MAP4K4. *Developmental cell* **31**, 572-585 (2014).

131. Komarova, Y.A. *et al.* VE-cadherin signaling induces EB3 phosphorylation to suppress microtubule growth and assemble adherens junctions. *Molecular cell* **48**, 914-925 (2012).
132. Stepanova, T. *et al.* Visualization of microtubule growth in cultured neurons via the use of EB3-GFP (end-binding protein 3-green fluorescent protein). *The Journal of neuroscience : the official journal of the Society for Neuroscience* **23**, 2655-2664 (2003).
133. Ban, R. *et al.* Mitotic regulation of the stability of microtubule plus-end tracking protein EB3 by ubiquitin ligase SIAH-1 and Aurora mitotic kinases. *The Journal of biological chemistry* **284**, 28367-28381 (2009).
134. Laketa, V., Simpson, J.C., Bechtel, S., Wiemann, S. & Pepperkok, R. High-content microscopy identifies new neurite outgrowth regulators. *Molecular biology of the cell* **18**, 242-252 (2007).
135. Arens, J., Duong, T.T. & Dehmelt, L. A morphometric screen identifies specific roles for microtubule-regulating genes in neuronal development of P19 stem cells. *PloS one* **8**, e79796 (2013).
136. Pierre, P., Scheel, J., Rickard, J.E. & Kreis, T.E. CLIP-170 links endocytic vesicles to microtubules. *Cell* **70**, 887-900 (1992).
137. Diamantopoulos, G.S. *et al.* Dynamic localization of CLIP-170 to microtubule plus ends is coupled to microtubule assembly. *The Journal of cell biology* **144**, 99-112 (1999).
138. Lansbergen, G. *et al.* Conformational changes in CLIP-170 regulate its binding to microtubules and dynactin localization. *The Journal of cell biology* **166**, 1003-1014 (2004).
139. Maurin, J., Blangy, A. & Bompard, G. Regulation of invadosomes by microtubules: Not only a matter of railways. *European journal of cell biology* **99**, 151109 (2020).
140. Cornfine, S. *et al.* The kinesin KIF9 and reggie/flotillin proteins regulate matrix degradation by macrophage podosomes. *Molecular biology of the cell* **22**, 202-215 (2011).
141. Galjart, N. Plus-end-tracking proteins and their interactions at microtubule ends. *Current biology : CB* **20**, R528-537 (2010).
142. Shekhar, S., Pernier, J. & Carlier, M.F. Regulators of actin filament barbed ends at a glance. *Journal of cell science* **129**, 1085-1091 (2016).
143. Bearce, E.A., Erdogan, B. & Lowery, L.A. TIPsy tour guides: how microtubule plus-end tracking proteins (+TIPs) facilitate axon guidance. *Frontiers in cellular neuroscience* **9**, 241 (2015).
144. Pollard, T.D. Actin and Actin-Binding Proteins. *Cold Spring Harbor perspectives in biology* **8** (2016).
145. Forscher, P. & Smith, S.J. Actions of cytochalasins on the organization of actin filaments and microtubules in a neuronal growth cone. *The Journal of cell biology* **107**, 1505-1516 (1988).
146. Suter, D.M. & Forscher, P. Substrate-cytoskeletal coupling as a mechanism for the regulation of growth cone motility and guidance. *Journal of neurobiology* **44**, 97-113 (2000).
147. Seetharaman, S. & Etienne-Manneville, S. Microtubules at focal adhesions - a double-edged sword. *Journal of cell science* **132** (2019).
148. Wittmann, T., Bokoch, G.M. & Waterman-Storer, C.M. Regulation of leading edge microtubule and actin dynamics downstream of Rac1. *The Journal of cell biology* **161**, 845-851 (2003).
149. Inoue, D. *et al.* Actin filaments regulate microtubule growth at the centrosome. *The EMBO journal* **38** (2019).
150. Plessner, M., Knerr, J. & Grosse, R. Centrosomal Actin Assembly Is Required for Proper Mitotic Spindle Formation and Chromosome Congression. *iScience* **15**, 274-281 (2019).

151. Griffith, L.M. & Pollard, T.D. Cross-linking of actin filament networks by self-association and actin-binding macromolecules. *The Journal of biological chemistry* **257**, 9135-9142 (1982).
152. Griffith, L.M. & Pollard, T.D. The interaction of actin filaments with microtubules and microtubule-associated proteins. *The Journal of biological chemistry* **257**, 9143-9151 (1982).
153. Henty-Ridilla, J.L., Rankova, A., Eskin, J.A., Kenny, K. & Goode, B.L. Accelerated actin filament polymerization from microtubule plus ends. *Science (New York, N.Y.)* **352**, 1004-1009 (2016).
154. Farhadi, L. *et al.* Actin and microtubule crosslinkers tune mobility and control co-localization in a composite cytoskeletal network. *Soft matter* **16**, 7191-7201 (2020).
155. Dogterom, M. & Koenderink, G.H. Actin-microtubule crosstalk in cell biology. *Nature reviews. Molecular cell biology* **20**, 38-54 (2019).
156. Foxall, E. *et al.* PAK4 Kinase Activity Plays a Crucial Role in the Podosome Ring of Myeloid Cells. *Cell reports* **29**, 3385-3393.e3386 (2019).
157. Bompard, G. & Morin, N. p21-activated kinase 4 regulates mitotic spindle positioning and orientation. *Bioarchitecture* **2**, 130-133 (2012).
158. Bompard, G. *et al.* P21-activated kinase 4 (PAK4) is required for metaphase spindle positioning and anchoring. *Oncogene* **32**, 910-919 (2013).
159. He, Y.T. *et al.* PAK4 Regulates Actin and Microtubule Dynamics during Meiotic Maturation in Mouse Oocyte. *International journal of biological sciences* **15**, 2408-2418 (2019).
160. Callow, M.G., Zozulya, S., Gishizky, M.L., Jallal, B. & Smeal, T. PAK4 mediates morphological changes through the regulation of GEF-H1. *Journal of cell science* **118**, 1861-1872 (2005).
161. Heck, J.N. *et al.* Microtubules regulate GEF-H1 in response to extracellular matrix stiffness. *Molecular biology of the cell* **23**, 2583-2592 (2012).
162. Watanabe, T. *et al.* Interaction with IQGAP1 links APC to Rac1, Cdc42, and actin filaments during cell polarization and migration. *Developmental cell* **7**, 871-883 (2004).
163. Cao, D. *et al.* Signaling Scaffold Protein IQGAP1 Interacts with Microtubule Plus-end Tracking Protein SKAP and Links Dynamic Microtubule Plus-end to Steer Cell Migration. *The Journal of biological chemistry* **290**, 23766-23780 (2015).
164. Fukata, M. *et al.* Rac1 and Cdc42 capture microtubules through IQGAP1 and CLIP-170. *Cell* **109**, 873-885 (2002).
165. Sakurai-Yageta, M. *et al.* The interaction of IQGAP1 with the exocyst complex is required for tumor cell invasion downstream of Cdc42 and RhoA. *The Journal of cell biology* **181**, 985-998 (2008).
166. Bartolini, F. & Gundersen, G.G. Formins and microtubules. *Biochimica et Biophysica Acta (BBA) - Molecular Cell Research* **1803**, 164-173 (2010).
167. Ishizaki, T. *et al.* Coordination of microtubules and the actin cytoskeleton by the Rho effector mDia1. *Nature cell biology* **3**, 8-14 (2001).
168. Palazzo, A.F., Cook, T.A., Alberts, A.S. & Gundersen, G.G. mDia mediates Rho-regulated formation and orientation of stable microtubules. *Nature cell biology* **3**, 723-729 (2001).
169. Chhabra, E.S. & Higgs, H.N. INF2 Is a WASP homology 2 motif-containing formin that severs actin filaments and accelerates both polymerization and depolymerization. *The Journal of biological chemistry* **281**, 26754-26767 (2006).
170. Gurel, P.S., Hatch, A.L. & Higgs, H.N. Connecting the cytoskeleton to the endoplasmic reticulum and Golgi. *Current biology : CB* **24**, R660-r672 (2014).
171. Fernández-Barrera, J. & Alonso, M.A. Coordination of microtubule acetylation and the actin cytoskeleton by formins. *Cellular and molecular life sciences : CMLS* **75**, 3181-3191 (2018).
172. Ramabhadran, V., Hatch, A.L. & Higgs, H.N. Actin monomers activate inverted formin 2 by competing with its autoinhibitory interaction. *The Journal of biological chemistry* **288**, 26847-26855 (2013).

173. Bartolini, F. *et al.* An mDia1-INF2 formin activation cascade facilitated by IQGAP1 regulates stable microtubules in migrating cells. *Molecular biology of the cell* **27**, 1797-1808 (2016).
174. Andrés-Delgado, L. *et al.* INF2 promotes the formation of detyrosinated microtubules necessary for centrosome reorientation in T cells. *The Journal of cell biology* **198**, 1025-1037 (2012).
175. Gaillard, J. *et al.* Differential interactions of the formins INF2, mDia1, and mDia2 with microtubules. *Molecular biology of the cell* **22**, 4575-4587 (2011).
176. Shirao, T. & Obata, K. Two acidic proteins associated with brain development in chick embryo. *Journal of neurochemistry* **44**, 1210-1216 (1985).
177. Shirao, T. & Obata, K. Immunochemical homology of 3 developmentally regulated brain proteins and their developmental change in neuronal distribution. *Brain Res* **394**, 233-244 (1986).
178. Shirao, T., Inoue, H.K., Kano, Y. & Obata, K. Localization of a developmentally regulated neuron-specific protein S54 in dendrites as revealed by immunoelectron microscopy. *Brain Res* **413**, 374-378 (1987).
179. Shirao, T., Kojima, N., Terada, S. & Obata, K. Expression of three drebrin isoforms in the developing nervous system. *Neurosci Res Suppl* **13**, S106-111 (1990).
180. Kojima, N., Shirao, T. & Obata, K. Molecular cloning of a developmentally regulated brain protein, chicken drebrin A and its expression by alternative splicing of the drebrin gene. *Brain Res Mol Brain Res* **19**, 101-114 (1993).
181. Hayashi, K. *et al.* Modulatory role of drebrin on the cytoskeleton within dendritic spines in the rat cerebral cortex. *The Journal of neuroscience : the official journal of the Society for Neuroscience* **16**, 7161-7170 (1996).
182. Sasaki, Y., Hayashi, K., Shirao, T., Ishikawa, R. & Kohama, K. Inhibition by drebrin of the actin-bundling activity of brain fascin, a protein localized in filopodia of growth cones. *Journal of neurochemistry* **66**, 980-988 (1996).
183. Peitsch, W.K. *et al.* Drebrin is a widespread actin-associating protein enriched at junctional plaques, defining a specific microfilament anchorage system in polar epithelial cells. *European journal of cell biology* **78**, 767-778 (1999).
184. Peitsch, W.K. *et al.* Drebrin particles: components in the ensemble of proteins regulating actin dynamics of lamellipodia and filopodia. *European journal of cell biology* **80**, 567-579 (2001).
185. Hayashi, K. *et al.* Domain analysis of the actin-binding and actin-remodeling activities of drebrin. *Experimental cell research* **253**, 673-680 (1999).
186. Hayashi, K. & Shirao, T. Change in the shape of dendritic spines caused by overexpression of drebrin in cultured cortical neurons. *The Journal of neuroscience : the official journal of the Society for Neuroscience* **19**, 3918-3925 (1999).
187. Ishikawa, R. *et al.* Drebrin attenuates the interaction between actin and myosin-V. *Biochemical and biophysical research communications* **359**, 398-401 (2007).
188. Shirao, T. *et al.* Formation of thick, curving bundles of actin by drebrin A expressed in fibroblasts. *Experimental cell research* **215**, 145-153 (1994).
189. Peitsch, W.K. *et al.* Dynamics of the actin-binding protein drebrin in motile cells and definition of a juxtanuclear drebrin-enriched zone. *Experimental cell research* **312**, 2605-2618 (2006).
190. Geraldo, S., Khanzada, U.K., Parsons, M., Chilton, J.K. & Gordon-Weeks, P.R. Targeting of the F-actin-binding protein drebrin by the microtubule plus-tip protein EB3 is required for neuritogenesis. *Nature cell biology* **10**, 1181-1189 (2008).
191. Merriam, E.B. *et al.* Synaptic regulation of microtubule dynamics in dendritic spines by calcium, F-actin, and drebrin. *The Journal of neuroscience : the official journal of the Society for Neuroscience* **33**, 16471-16482 (2013).
192. Gordon-Weeks, P.R. The role of the drebrin/EB3/Cdk5 pathway in dendritic spine plasticity, implications for Alzheimer's disease. *Brain research bulletin* **126**, 293-299 (2016).

193. Poobalasingam, T., Bianco, F., Oozeer, F. & Gordon-Weeks, P.R. The drebrin/EB3 pathway regulates cytoskeletal dynamics to drive neuritogenesis in embryonic cortical neurons. *Journal of neurochemistry* **160**, 185-202 (2022).
194. Dart, A.E. *et al.* The drebrin/EB3 pathway drives invasive activity in prostate cancer. *Oncogene* **36**, 4111-4123 (2017).
195. Alvarez-Suarez, P. *et al.* Drebrin Regulates Acetylcholine Receptor Clustering and Organization of Microtubules at the Postsynaptic Machinery. *International journal of molecular sciences* **22** (2021).
196. Bouchet, B.P. *et al.* Talin-KANK1 interaction controls the recruitment of cortical microtubule stabilizing complexes to focal adhesions. *eLife* **5**, e18124 (2016).
197. Chen, N.P., Sun, Z. & Fässler, R. The Kank family proteins in adhesion dynamics. *Curr Opin Cell Biol* **54**, 130-136 (2018).
198. Sun, Z. *et al.* Kank2 activates talin, reduces force transduction across integrins and induces central adhesion formation. *Nature cell biology* **18**, 941 (2016).
199. Rafiq, N.B.M. *et al.* A mechano-signalling network linking microtubules, myosin IIA filaments and integrin-based adhesions. *Nature materials* **18**, 638-649 (2019).
200. Paradžik, M. *et al.* KANK2 Links αVβ5 Focal Adhesions to Microtubules and Regulates Sensitivity to Microtubule Poisons and Cell Migration. *Frontiers in cell and developmental biology* **8**, 125 (2020).
201. Lansbergen, G. & Akhmanova, A. Microtubule plus end: a hub of cellular activities. *Traffic (Copenhagen, Denmark)* **7**, 499-507 (2006).
202. Lansbergen, G. *et al.* CLASPs attach microtubule plus ends to the cell cortex through a complex with LL5beta. *Developmental cell* **11**, 21-32 (2006).
203. van der Vaart, B. *et al.* CFEOM1-Associated Kinesin KIF21A Is a Cortical Microtubule Growth Inhibitor. *Developmental cell* **27**, 145-160 (2013).
204. Astro, V. & de Curtis, I. Plasma membrane-associated platforms: dynamic scaffolds that organize membrane-associated events. *Science signaling* **8**, re1 (2015).
205. Horton, E.R. *et al.* Definition of a consensus integrin adhesome and its dynamics during adhesion complex assembly and disassembly. *Nature cell biology* **17**, 1577-1587 (2015).
206. Sarkar, S. *et al.* A novel ankyrin repeat-containing gene (Kank) located at 9p24 is a growth suppressor of renal cell carcinoma. *The Journal of biological chemistry* **277**, 36585-36591 (2002).
207. Yu, M. *et al.* Force-Dependent Regulation of Talin-KANK1 Complex at Focal Adhesions. *Nano letters* **19**, 5982-5990 (2019).
208. Hida, Y. & Ohtsuka, T. CAST and ELKS proteins: structural and functional determinants of the presynaptic active zone. *The Journal of Biochemistry* **148**, 131-137 (2010).
209. Spangler, S.A. & Hoogenraad, C.C. Liprin-α proteins: scaffold molecules for synapse maturation. *Biochemical Society transactions* **35**, 1278-1282 (2007).
210. Herzog, R., van den Dries, K., Cervero, P. & Linder, S. Poji: a Fiji-based tool for analysis of podosomes and associated proteins. *Journal of cell science* (2020).
211. Tinevez, J.Y. *et al.* TrackMate: An open and extensible platform for single-particle tracking. *Methods (San Diego, Calif.)* **115**, 80-90 (2017).
212. Naj, X., Hoffmann, A.K., Himmel, M. & Linder, S. The formins FMNL1 and mDia1 regulate coiling phagocytosis of Borrelia burgdorferi by primary human macrophages. *Infection and immunity* **81**, 1683-1695 (2013).
213. Chen, L. & Ko, C.P. Extension of synaptic extracellular matrix during nerve terminal sprouting in living frog neuromuscular junctions. *The Journal of neuroscience : the official journal of the Society for Neuroscience* **14**, 796-808 (1994).
214. Sellner, J. in Milania's Blog, Vol. 2022 (2016). https://milania.de/blog/Intersection_area_of_two_circles_with_implementation_in_C%2B%2B (last visit on webpage 16.10.2022)
215. Bhuwania, R., Castro-Castro, A. & Linder, S. *Microtubule acetylation regulates dynamics of KIF1C-powered vesicles and contact of microtubule plus ends with podosomes*, Vol. 93. (2014).

216. Tarone, G., Cirillo, D., Giancotti, F.G., Comoglio, P.M. & Marchisio, P.C. Rous sarcoma virus-transformed fibroblasts adhere primarily at discrete protrusions of the ventral membrane called podosomes. *Experimental cell research* **159**, 141-157 (1985).
217. Ezratty, E.J., Partridge, M.A. & Gundersen, G.G. Microtubule-induced focal adhesion disassembly is mediated by dynamin and focal adhesion kinase. *Nature cell biology* **7**, 581-590 (2005).
218. Ezratty, E.J., Bertaux, C., Marcantonio, E.E. & Gundersen, G.G. Clathrin mediates integrin endocytosis for focal adhesion disassembly in migrating cells. *The Journal of cell biology* **187**, 733-747 (2009).
219. Kaverina, I., Rottner, K. & Small, J.V. Targeting, capture, and stabilization of microtubules at early focal adhesions. *The Journal of cell biology* **142**, 181-190 (1998).
220. Krylyshkina, O. *et al.* Nanometer targeting of microtubules to focal adhesions. *The Journal of cell biology* **161**, 853-859 (2003).
221. Ren, X.D. *et al.* Focal adhesion kinase suppresses Rho activity to promote focal adhesion turnover. *Journal of cell science* **113 (Pt 20)**, 3673-3678 (2000).
222. Gupton, S.L. & Waterman-Storer, C.M. Spatiotemporal feedback between actomyosin and focal-adhesion systems optimizes rapid cell migration. *Cell* **125**, 1361-1374 (2006).
223. Zaidel-Bar, R., Milo, R., Kam, Z. & Geiger, B. A paxillin tyrosine phosphorylation switch regulates the assembly and form of cell-matrix adhesions. *Journal of cell science* **120**, 137-148 (2007).
224. Kim, D.H. & Wirtz, D. Focal adhesion size uniquely predicts cell migration. *FASEB journal : official publication of the Federation of American Societies for Experimental Biology* **27**, 1351-1361 (2013).
225. Malik-Sheriff, R.S., Imtiaz, S., Grecco, H.E. & Zamir, E. Diverse patterns of molecular changes in the mechano-responsiveness of focal adhesions. *Sci Rep* **8**, 2187 (2018).
226. Akisaka, T., Yoshida, H. & Takigawa, T. Differential distribution of posttranslationally modified microtubules in osteoclasts. *The journal of histochemistry and cytochemistry : official journal of the Histochemistry Society* **59**, 630-638 (2011).
227. Zhu, X., Efimova, N., Arnette, C., Hanks, S.K. & Kaverina, I. Podosome dynamics and location in vascular smooth muscle cells require CLASP-dependent microtubule bending. *Cytoskeleton (Hoboken, N.J.)* **73**, 300-315 (2016).
228. Linder, S. & Cervero, P. The podosome cap: past, present, perspective. *European journal of cell biology* **99**, 151087 (2020).
229. Noordstra, I. & Akhmanova, A. Linking cortical microtubule attachment and exocytosis. *F1000Research* **6**, 469 (2017).
230. Bazellières, E. *et al.* Apico-basal elongation requires a drebrin-E-EB3 complex in columnar human epithelial cells. *Journal of cell science* **125**, 919-931 (2012).
231. Ishikawa, R. *et al.* Drebrin, a development-associated brain protein from rat embryo, causes the dissociation of tropomyosin from actin filaments. *The Journal of biological chemistry* **269**, 29928-29933 (1994).
232. Spanjaard, E. & Johan Mechanotransduction: Vinculin Provides Stability when Tension Rises. *Current Biology* **23**, R159-R161 (2013).
233. Li, B. *et al.* Drebrin restricts rotavirus entry by inhibiting dynamin-mediated endocytosis. *Proceedings of the National Academy of Sciences of the United States of America* **114**, E3642-e3651 (2017).
234. Vacca, B. *et al.* Drebrin E depletion in human intestinal epithelial cells mimics Rab8a loss of function. *Human molecular genetics* **23**, 2834-2846 (2014).
235. Cervero, P., Vrenken, K., Klose, M., Rehm, K. & Linder, S. Nectin stabilization at adherens junctions is counteracted by Rab5a-dependent endocytosis. *European journal of cell biology* **100**, 151184 (2021).
236. Yu, Q. *et al.* Drebrin promotes lung adenocarcinoma cell migration through inducing integrin β1 endocytosis. *Biochemical and biophysical research communications* **630**, 175-182 (2022).

237. Hackett, B.A. & Cherry, S. Flavivirus internalization is regulated by a size-dependent endocytic pathway. *Proceedings of the National Academy of Sciences of the United States of America* **115**, 4246-4251 (2018).
238. Marx, A. *et al.* Xenopus cytoplasmic linker-associated protein 1 (XCLASP1) promotes axon elongation and advance of pioneer microtubules. *Molecular biology of the cell* **24**, 1544-1558 (2013).
239. Engel, U. *et al.* Abelson phosphorylation of CLASP2 modulates its association with microtubules and actin. *Cytoskeleton (Hoboken, N.J.)* **71**, 195-209 (2014).
240. Juanes, M.A. *et al.* Adenomatous polyposis coli nucleates actin assembly to drive cell migration and microtubule-induced focal adhesion turnover. *The Journal of cell biology* **216**, 2859-2875 (2017).

13 Publications

Parts of the content presented here have been published:

Weber, K., Hey, S., Cervero, P., & Linder, S. (2022). The circle of life: Phases of podosome formation, turnover and reemergence. *Eur J Cell Biol, 101*(2), 151218. doi:https://doi.org/10.1016/j.ejcb.2022.151218

Pacheco-Fernandez, N., Pakdel, M., Blank, B., Sanchez-Gonzalez, I., Weber, K., Tran, M. L., . . . Von Blume, J. (2020). Nucleobindin-1 regulates ECM degradation by promoting intra-Golgi trafficking of MMPs. *Journal of Cell Biology, 219*(8). doi:10.1083/jcb.201907058

Parts of the content presented here have been shown at:

Kathrin Weber, Robert Herzog, Stefan Linder (2019). Influence of podosome cap components on MT1-MMP transport to podosomes (Poster#36) 6th ZOO meeting Rotterdam: *Cell Adhesion and Migration in Inflammation and Cancer*, May 15-18, 2019, Rotterdam, Netherlands

Kathrin Weber, Robert Herzog, Stefan Linder (2019). Influence of podosome cap components on MT1-MMP transport to podosomes (Poster and flash talk) Invadosome 2019: *Mechano-chemical signals in invasion*, June 19-22, 2019, London, UK

Manuscripts in preparation:

Weber, K; Herzog, R.; Hey, S. & Linder, S.: A drebrin-EB3 axis regulates contact of microtubule +tips with podosomes

Woitzik, P., Weber, K., Herzog, R, Hey, S., Horst, A., Cervero, P., Linder, S.: Glycolytic PKM2 differentially regulates podosome formation and function

14 Danksagung

Zum Schluss möchte ich mich bei allen bedanken, die mich auf verschiedenste Weise während der Dissertationszeit unterstützt haben. Einige möchte ich nochmal hervorheben:

Bei Prof. Dr. Stefan Linder möchte ich mich für die Aufnahme ins Labor, die Vergabe des spannenden Themas und die Betreuung bedanken. Besonders faszinierend war, dass egal wie verzwickt mir mein Projekt vorkam, ein kleines Gespräch schon ausreichte, um wieder das ganze Potential zu sehen und euphorisch weiterzuwerkeln. An dieser Stelle möchte ich auch Bernd für den Austausch verschiedenster Küchenleckereien danken.

Herrn PD Dr. Pommerening-Röser möchte ich sehr für die Übernahme des Zweitgutachtens danken, Frau Prof. Dr. Julia Kehr danke ich für die Teilnahme und Unterstützung in der Prüfungskommission. Außerdem möchte ich mich auch bei Petra Ziemer aus dem Promotionsbüro bedanken, für Ihre schnelle Unterstützung in organisatorischen Fragen.

Weiter möchte ich mich bei Bernd, Sabine und Virgilio für die Betreuung der Mikroskope bedanken, an denen ich wohl fast die Hälfte meiner Arbeitszeit verbracht habe.

Ich möchte mich auch bei allen Labor-Mitgliedern des LinderLabs bedanken: eine solch angenehme Kollegentruppe findet man wohl nirgends: egal ob Kaffeerunden & Mittagessen, Grillaktionen, Film-Abende, Feuerzangenbowle, Pizza-Essen oder HeidePark; mit euch hat alles Spaß gemacht. Besonders herausheben möchte ich hier Robert, der nicht nur ein guter Diskussionspartner, sondern in den vergangenen Jahren mit allen Höhen und Tiefen zu einem sehr guten Freund geworden ist. Auch möchte ich Johann nicht unerwähnt lassen, der mit seiner tollen Lebenssicht mich um einige Erkenntnisse und witzige Geschichten bereichert hat. Auch Pasquale, dem besten Parmigiano-Dealer, möchte ich für die vielen so hilfreichen Gespräche danken. Nicht zu vergessen ist natürlich Andrea, ohne Dich läuft das Labor nicht!

Auch möchte ich meiner Biochemiker-Truppe danken, allen voran meiner Studienfreundin Anne. Auf dich kann ich immer zählen, deine Hilfsbereitschaft und Freundschaft hat einen unschätzbaren Wert.

Zu guter Letzt möchte ich meiner Familie und insbesondere meinem Freund danken, für die ganze Unterstützung, die Geduld, Rückhalt und Liebe die nicht in Worte gefasst werden kann.

Danke!

15 Eidesstattliche Erklärung

Hiermit erkläre ich an Eides statt, dass ich die vorliegende Dissertationsschrift selbst verfasst und keine anderen als die angegebenen Quellen und Hilfsmittel benutzt habe. Ebenfalls erkläre ich an Eides statt, dass alle dem Prüfungsamt und den Gutachtern vorliegenden Exemplare (digital sowie physisch) mit dieser Dissertationsschrift identisch sind.

Hamburg, den 17.10.2022 (Kathrin Weber)